UNICAMP

UNIVERSIDADE ESTADUAL DE CAMPINAS
Instituto de Física Gleb Wataghin

Mônica Soares Nunes

Impact of Electron Lifetime on Electromagnetic Shower Separation

Impacto do Tempo de Vida dos Elétrons na Separação de Chuveiros Eletromagnéticos

CAMPINAS

2019

Mônica Soares Nunes

Impact of Electron Lifetime on Electromagnetic Shower Separation

Impacto do Tempo de Vida dos Elétrons na Separação de Chuveiros Eletromagnéticos

Tese apresentada ao Instituto de Física Gleb Wataghin da Universidade Estadual de Campinas como parte dos requisitos exigidos para a obtenção do título de Doutora em Ciências.

Thesis presented to the Institute of Physics Gleb Wataghin of the University of Campinas in partial fulfillment of the requirements for the degree of Doctor in Science.

Supervisor/Orientador: Prof. Dr. Ernesto Kemp

Este exemplar corresponde à versão final da tese defendida pela aluna Mônica Soares Nunes, e orientada pelo Prof Dr Ernesto Kemp.

Assinatura do Orientador

—————————————————————

Campinas

2019

N922i   Nunes, Mônica Soares, 1987-
             Impact of electron lifetime on electromagnetic shower separation / Mônica
       Soares Nunes. – Campinas, SP : [s.n.], 2019.

             Orientador: Ernesto Kemp.
             Tese (doutorado) – Universidade Estadual de Campinas, Instituto de Física
       Gleb Wataghin.

             1. Neutrinos. 2. Argônio líquido. 3. Chuveiros eletromagnéticos. I. Kemp,
       Ernesto, 1965-. II. Universidade Estadual de Campinas. Instituto de Física Gleb
       Wataghin. III. Título.

MEMBROS DA COMISSÃO JULGADORA DA TESE DE DOUTORADO DE **MÔNICA SOARES NUNES – RA: 045446** APRESENTADA E APROVADA AO INSTITUTO DE FÍSICA "GLEB WATAGHIN", DA UNIVERSIDADE ESTADUAL DE CAMPINAS, EM 12 / 12 / 2019.

COMISSÃO JULGADORA:

- Prof. Dr. Ernesto Kemp – Orientador – DRCC/IFGW/UNICAMP
- Prof. Dr. Pedro Cunha de Holanda – DRCC/IFGW/UNICAMP
- Prof. Dr. Anderson Campos Fauth – DRCC/IFGW/UNICAMP
- Prof. Dr. João Carlos Costa dos Anjos – Observatório Nacional
- Prof. Dr. Célio Adrega de Moura Júnior – DF/UFABC

OBS.: Ata da defesa com as respectivas assinaturas dos membros encontra-se no SIGA/Sistema de Fluxo de Dissertação/Tese e na Secretaria do Programa da Unidade

CAMPINAS
2019

ACKNOWLEDGEMENTS

all the coffees, thank you for all the happy hours, thank you for all the horoscope readings, thank you for all our time together! I love you, and I wish you all the success in this world!

I want to send special thanks to Ohana, Gabriela and Pedro! Thank you guys for your friendship and all the support! Thank you for all the time that you spend listening to my problems! Thank you for all the great moments of fun and sushis!

I also want to thank all the special people that I have met at Fermilab. People from many different places, with different cultures backgrounds that enriched my life in the United States. Thank you for all the parties, all the great conversations, thank you for making me feel welcomed to this new country.

Professor Dr. Ernesto Kemp! Thank you for being my advisor and one of my best friends for all these years. Thank you for all the support, all the conversations, all the lessons and for your friendship! Thank you for believing in me even if I did not believe in myself. You are truly special!

To all the professors of the Physics Institute at UNICAMP: thank you for passing along your valuable knowledge.

Jen and Jonathan, thank you for welcoming me to this big-hearted experiment. LArIAT is this great collaboration because it counts with you on its leadership. I am very thankful to you for all the support and for everything that I have learned during my stay at Fermilab.

Vito, my love, thank you for your love and your support! Thank you for all this time that we have been together! I love you!

Bissetriz and Entropia, my fur daughters, I love you very much! I am sorry for leaving you sometimes, but it was always to make life better for our family!

Vovó Cida, I miss you every day of my life, and I know I will love you forever!

RESUMO

Neutrinos são partículas que, apesar de abundantes no universo, interagem pouco com a matéria. Experimentos anteriores detectaram um excesso de neutrinos na região de baixa energia que pode estar ligado à existência de um quarto tipo de neutrino, o neutrino estéril. Esse excesso pode ser devido ao novo neutrino ou simplesmente devido à incapacidade dos experimentos anteriores de diferenciar chuveiros eletromagnéticos iniciados por elétrons ou fótons. Por isso, experimentos de neutrinos utilizando argônio líquido estão sendo construídos atualmente e apostam nas câmaras temporais de argônio líquido (LArTPCs) para responder à essas e outras questões em aberto sobre essas partículas misteriosas.

LArTPCs representam hoje o futuro para a pesquisa de neutrinos. Possuem alta resolução espacial e grande capacidade calorimétrica. Diversos experimentos estão em fase de planejamento utilizando essa tecnologia portanto, é necessário ter grande compreensão sobre as interações de partículas em argônio líquido. O experimento LArIAT foi criado para realizar estudos que auxiliem a caracterização da resposta do detector à partículas carregadas esperadas em interações de neutrinos. O detector é exposto a um feixe de partículas carregadas e recebe uma quantidade grande de enventos de elétrons dentro da câmara, tornando-o um experimento perfeito para auxiliar no estudo da separação de chuveiros eletromagnéticos.

Para que as interações sejam corretamente identificadas e o máximo de informação possa ser coletada, o argônio líquido utilizado precisa estar com alta pureza. Nesta tese, é descrito o processo utilizado no experimento LArIAT para o monitoramento da pureza do argônio utilizando múons cósmicos e o impacto desta medida na separação de chuveiros eletomagnéticos.

Palavras-chave: neutrinos, pureza do argônio, chuveiros eletromagnéticos.

ABSTRACT

Neutrinos are superabundant particles in the universe but rarely interact with matter. Previous experiments noticed an excess of neutrinos in the low energy range that could be connected to the existence of a fourth type of neutrino: the sterile neutrino. This excess could be because of the new neutrino or just because of the incapacity of previous experiments on distinguishing electromagnetic showers initiated by electrons and photons. So, new experiments using liquid argon are being developed and bet on the liquid argon time projection chambers (LArTPCs) to find answers for these and other still open questions about these mysterious particles.

LArTPCs represent today the future for neutrinos research. They have high spatial resolution and great calorimetric capacity. Many experiments are being planned using this technique; consequently, it is necessary to understand the particle's interactions in liquid argon completely. The LArIAT experiment was created to help in the characterization of this kind of detector's response to charged particles that are expected to come out of neutrino interactions. The detector is exposed to a charged particle beam and receives a high number of electrons, making this a perfect experiment to help in the study of electromagnetic shower separation.

To correctly identify the interactions and to collect the maximum information about them, the liquid argon that is utilized has to be ultra-pure. In this thesis, the process used on LArIAT to monitor the argon's purity using cosmic muons is described, as well as the impact of this measurement on the separation of electromagnetic showers.

Keywords: neutrinos, argon purity, electromagnetic showers.

LIST OF FIGURES

CONTENTS

CHAPTER 1

INTRODUCTION

The discovery that neutrinos are capable of oscillating constitutes a significant milestone in astro and particle physics over the last few decades. Studies involving solar and atmospheric neutrinos were the first to provide evidence of this new behavior of the ghost particles. With this discovery, a new world "Beyond the Standard Model" of particle physics was created, and with it, lots of fresh possibilities were open. Many experiments commenced being developed with new technologies that were going to be capable of doing an in-depth study of these particles.

The Cherenkov neutrino experiments LSND and MiniBooNE found an excess of low energy electron neutrinos that could indicate the existence of a fourth type of neutrino: the sterile neutrino. The three-neutrinos known model can not describe this excess. However, it is not known yet if this is an indication of the fourth neutrino or if it was just the inability of the previous neutrino experiments of differentiating electromagnetic showers.

Liquid Argon Time Projection Chambers were found as the best solution to solve this and many other open questions, due to its high spatial resolution and calorimetric capacity.

In chapter 2, the neutrino oscillations are covered. From the historical background to their interactions, it is possible to understand the particles that are the heart of the new generation of particle physics experiments.

The main problem that led to this study is presented in chapter 3. The previous neutrino experiments found an excess of electron neutrinos in the low energy range that could indicate a new neutrino type. The next generation of neutrino experiments will be able to answer this and many other still open questions.

Chapter 4 describes the technology used in the new neutrino experiments that will be

able to solve the low energy excess problem.

To characterize the new types of detectors, the experiment described in chapter 5 was created. In this chapter, all the parts of the experiment are explained.

Chapter 6 will describe the technique used to monitor the argon purity in the experiments.

And, finally, chapter 7 presents the impact of the purity measurements in the separation between electromagnetic showers, which will be able to verify the low energy neutrino excess.

CHAPTER 2

NEUTRINOS

Neutrinos are tiny neutral elementary particles that rarely interact with matter. Due to this characteristic, giant detectors are necessary to study them deeply to fully understand their behavior.

When neutrinos were first discovered, in 1956 (10), scientists believed that they had zero mass and would interact only via weak interaction, being the least exciting particles to be studied. Actually, these particles can travel hundreds of light-years through a wall of lead without having a single interaction. To interact this little means that for scientists to detect these neutrinos, they need massive detectors and a powerful neutrino source. After the discovery of their capacity of oscillating, meaning that they are now massive particles, the idea of neutrinos being dull particles changed, brought lots of questions to the community, and opened doors for physics beyond the Standard Model (the particle physic's bible). It is known now that neutrinos could be the key to give physicists many answers about the great mysteries of physics, such as the asymmetry of matter and anti-matter in the universe or even if more types of neutrinos exist. To try to solve these new questions in the neutrino world, multiple neutrino experiments have been built or are being planned to be part of these studies.

This chapter will overview the Standard Model for particles and its implications for neutrinos. Also, the most significant experimental results of neutrino experiments will be shown. Open questions that still exist in the particle physics world concerning neutrinos will be discussed.

2.1 The Standard Model: the theory that describes almost everything

The Standard Model (SM) is a successful theory that started to be developed in the 70s, and it describes the fundamental particles (the basic building blocks of the universe) and fundamental forces, but gravity, in nature. It has been extensively tested through all these years, always presenting high precision on the results, and since the beginning, all the particles it predicted theoretically to exist have been found experimentally culminating with the discovery at CERN of the Higgs boson in 2012.

In the SM, the foundations for the known matter ("matter-particles") are quarks and leptons. They differ by intrinsic properties and how they interact with each other by the exchange of gauge bosons. Quarks and leptons have spin $1/2$ and follow the Fermi-Dirac statistic. Bosons will follow the Bose-Einstein statistics since they have integer spin and will act as the force carriers to mediate the interactions between fermions.

The Standard Model is a gauge theory based on the symmetry group $SU(3)_C \times SU(2)_L \times U(1)_Y$, with the subscript C representing the color charge, the subscript L indicating coupling only to left-handed fermions and the subscript Y representing the conserved hypercharge.

The left-handed fermions are organized in three generations doublets, while the right-handed ones are organized in singlets.

Electrons, muons, taus compose the leptons group together with electron neutrino, muon neutrino, and tau neutrino. Electrons, muons, and taus have an electric charge equal -1 (comparing to the value of the elementary charge), and all the three neutrinos associated with them are neutral. Leptons are arranged into three generations of doublets, in a progressive mass hierarchy of electrons, muons, and taus: one charged lepton with its associated neutral lepton. These particles do not carry color properties and will interact via the electroweak forces.

Quarks, in contrast with leptons, are known for the fact that they can possess one of the three colors allowing them to interact via the strong force. Quarks are organized as triplets of $SU(3)$ and have fractional electric charges (comparing to the value of the elementary charge). Moreover, since they also possess electric charge and flavor, they can participate in electromagnetic interactions. The strong force will be responsible for maintaining these particles together to form structures as barions (the combination of three quarks) or mesons (the combination of a quark with an anti-quark), always keeping a neutral color particle as a result. It is not possible to have free quarks because of the requirement of color neutrality

Table 2.1: Standard Model elementary fermionic fields with isospin (T), hypercharge (Y) and electric charge (Q). Subscripts L and R represent negative chirality (left-handed) and positive chirality (right handed).

Generation	I	II	III	T	Y	Q
Leptons	$\nu_{e,L}$	$\nu_{\mu,L}$	$\nu_{\tau,L}$	1/2	-1	0
	e^-_L	μ_L	τ_L	-1/2	-1	-1
	e^-_R	μ_R	τ_R	0	-2	1
Quarks	u_L	c_L	t_L	1/2	1/3	2/3
	d_L	s_L	b_L	-1/2	1/3	-1/3
	u_R	c_R	t_R	0	4/3	2/3
	d_R	s_R	b_R	0	-2/3	-1/3

and strong force confinement at low energies.

Gauge bosons are responsible for mediating the interactions between fermions acting as force carriers for strong and electroweak forces. Gamma ($gamma$) is the one responsible for the electromagnetic interaction, gluons (g) will mediate the strong interactions and, $W^{\pm}$ and Z^0 are the bosons that participate in the weak interactions. Higgs is another (famous) boson that is part of the SM. His significance and notoriety arise from the fact that he is responsible for explaining the existence of all particle's masses, and it was the last piece of the SM to be discovered experimentally.

The Higgs boson plays a crucial role in explaining the existence of the particle's masses. The Higgs Mechanism was proposed in the 1960s by Robert Brout, François Englert and Peter Higgs (11; 12) to account for the electroweak symmetry break that was responsible for allowing that the weak force carriers to have masses. Peter Higgs noticed that this mechanism would require the existence of an unseen particle, which is called now the Higgs Boson.

The Standard Model is summarized in table 2.1. The model also contemplates all the anti-particles of the fermions, not shown in this table. They all have inverted quantum numbers comparing to their particles.

2.2   Neutrinos: The ghost particles

At the beginning of the particle's physics history around the year of 1930, protons and electrons were believed to be the elementary particles, and the nuclei were believed to be bound states of protons and electrons. From this point of view, the β decay of a nucleus (A, Z) would be a process like $(A, Z) \rightarrow (A, Z+1) + e^-$ and the emitted electron would have a fixed value for its kinetic energy, however what was measured in experiments was that the spectrum of the energy of this emitted beta was compatible with three bodies decays. Niels Bohr was ready to abandon the law of conservation of energy to explain what was seen in the measurements, but fortunately, Pauli proposed the existence of a new particle that was being emitted with the electron in beta decays: a ghost particle that was exiting the process without being noticed and "stealing" the missing energy. This new particle had to be electrically neutral to conserve charge and to explain the absence of a track, it had to interact weakly with the nuclei, and it had to be very light to match the possible values for the electron's energies. In 1933 Enrico Fermi presented a theory for beta decay utilizing Pauli's new particle, and it was a great success. This new particle was then called neutrino (in fact, nowadays, this is the anti-neutrino). So, in modern terminology, the beta decay is known to be like:

$$(Z, N) \rightarrow (Z + 1, N - 1) + e + \bar{\nu} \tag{2.1}$$

where: (Z, N) is the original nucleus, (Z+1, N-1) is the emitted nucleus after the emission of the beta particle e and the anti-neutrino $\bar{\nu}$. Or, it can also be written as:

$$n \rightarrow p + e + \bar{\nu} \tag{2.2}$$

Rearranging the particles in this equations, it is possible to have these reactions:

$$\nu + n \rightarrow p + e \tag{2.3}$$

or

$$\bar{\nu} + p \rightarrow n + e^+ \tag{2.4}$$

Which are called inverse beta decays.

Neutrinos were first detected in 1956 by Clyde Cowan and Frederick Reines at the Savannah River Experiment. This observation happened 26 after this particle was first proposed to explain the apparent lack of energy conservation in beta decays and Cowan and Reines sent Pauli a telegram informing the detection: "We are happy to inform you that

we have definitely detected neutrinos from fission fragments by observing inverse beta decay of protons. Observed cross-section agrees well with expected six times ten to minus forty-four square centimeters" (13).

Since then, many studies were developed to investigate these challenge particles. By the end of the fifties and the beginning of the sixties, when scientists were studying observed and forbidden reactions involving neutrinos, it was proposed two new conservation numbers: muon number and electron number to explain some decays. So, with these new conservation laws, scientists had to assume that there were two different kinds of neutrinos: one associated with electrons, and another associated with muons. In 1962 Leon Lederman, Melvin Schwartz, and Jac Steinberger detected for the first time interactions of the muon neutrino with an experiment at the Brookhaven Laboratory (14).

Finally, in 1975, a new lepton was discovered with the Mark I experiment at SLAC-LBL group (15). The tau particle arrived to insert the third generation of leptons and for scientists to propose a new kind of neutrino: the tau neutrino. In 2000, the DONUT experiment, from Fermilab, announced the discovery of tau neutrinos, the last lepton of the Standard Model (16).

The confirmation of the existence of neutrinos was a pioneering contribution to neutrino science. It opened the doors to the world of "impossible" neutrino experiments.

Nowadays, it is well known that neutrinos are the most abundant fermion in the universe, and there are still many open questions related to these ghost particles. They have behaviors that are not explained with the Standard Model; scientists still do not know if they are their own anti-particle; the community still searches for a possible fourth type of neutrino... There are lots of questions, with lots of research opportunities to face these exciting and challenging times.

2.3 Neutrino Oscilations

2.3.1 Historical background

In 1964, John Bahcall and Raymond Davis Jr. proposed an experiment to study the production of sunlight according to the model in equation 2.5

$$4p \rightarrow^4 He + 2e^+ + 2\nu_e \tag{2.5}$$

With a detailed computer model of the Sun, Bahcall and his colleagues calculated the

number of neutrinos of different energies that were produced by the Sun. They also predicted the number of radioactive argon atoms that these neutrinos would produce in the experiment according to the reaction 2.6 equation.

$$\nu_e +^{37} Cl \to^{37} Ar + e^-$$
(2.6)
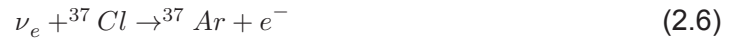
The results of Ray Davi's Homestake Experiment referencia solar neutrino experiment were announced in 1968, showing that only roughly a third of the predicted number of neutrinos was detected. This was known as "The Solar Neutrino Problem" or also as "The Mystery of the Missing Neutrinos" (17)

The first explanation found for this problem was, of course, that the theoretical calculations were wrong. It could be either predicting incorrectly the number of the produced neutrinos in the Sun or the incorrect number of the production rate of argon atoms in the experiment. Another possible explanation was that the experiment itself was projected wrongly. Moreover, another possibility would be that perhaps the physicists did not fully understand neutrinos.

Many different researchers revised the theoretical calculations, the data used was improved, and the predictions became more accurate. Scientists could not find any significant error in the computer model of the Sun or in the calculation of the probability of the detector to capture neutrinos. After all the possible tests and verifications, the discrepancy between the theoretical value and the experiment measurement persisted.

In 1969, B. Pontecorvo and V. Gribov proposed that neutrinos could behave differently than what the physicists of that time were assuming. They proposed the first phenomenological scheme of neutrino mixing. At that moment, very few physicists believed in this new idea, but pieces of evidence favoring this possibility increased with time.

Moving twenty years to the future, there were scientists still trying to solve the solar neutrino problem. The Kamiokande experiment finally showed some conclusive evidence of the anomaly. The Kamiokande experiment used a 2 kiloton Cherenkov detector of pure water with a low enough energy threshold to detect high energy neutrinos through neutrino-electron elastic scattering. A bigger version of the Kamiokande experiment, the SuperKamiokande, succeeded the previous detector. This new one was filled with 50 kiloton of pure water faced by 11,000 photomultiplier tubes. These two experiments confirmed that the number of detected neutrinos was smaller than the value predicted by the theoretical model of the Sun, although instead of detecting only $1/3$ of the predicted value, the Kamiokandes were detecting $1/2$. (18)

The solution to the solar neutrino problem has finally arrived from the Sudbury Neutrino Observatory (SNO) in Canada in 2001. Ray Davi's Homestake Experiment was only sensitive to electron neutrinos, and the Kamiokande Experiment was primarily sensitive to electron neutrinos but had some sensitivity to other neutrino flavors. The SNO experiment uses 1,000 tons of heavy water (D_2), and it was known as the "two-in-one" experiment. This new detector was able to measure the total flux of solar neutrinos, and it was able to distinguish between electron neutrinos and other neutrino flavors (electron neutrinos via charge current interactions and the other two flavors by neutral current interactions). They announced that the total flux detected was comparable with the theoretical prediction, and roughly two-thirds of the electron neutrinos have oscillated to the other flavors.

With the confirmation that neutrinos can oscillate, scientists discovered that neutrinos also have mass. New exciting times for particle physicists arrived. To understand why neutrinos oscillate, what are their masses, and if there are other neutrino flavors out there, physicists had to go beyond the Standard Model of particle physics to find the answers. Many new experiments had to be designed to collect data to solve all these new questions that appeared.

2.3.2   Theoretical Model of Neutrino Mixing

The fact that neutrinos can oscillate implies directly on the fact that they are not massless particles. If neutrinos were massless as the Standard Model predicted, they would be traveling at the speed of light and would not have a measure of time in their frame of reference where it would be possible to define the process of oscillation.

Neutrinos are emitted and absorbed only in weak processes and in their flavor eigenstates (ν_l), but as they travel, they will do so in their mass eigenstates (ν_m). The oscillation arises from neutrino mixing between their flavor and mass eigenstates. Flavor eigenstates could then be constructed as a linear combination of these individual mass eigenstates:

$$\nu_l = \sum_m U_{lm} \nu_m \tag{2.7}$$

and one could also express a mass eigenstate as a combination of flavor states:

$$\nu_m = \sum_{l'} U^*_{l'm} \nu_{l'} \tag{2.8}$$

The concept of mixing flavors is not new in quantum mechanics. In particle physics, this was first observed in the quark sector, where small amounts of cross-generational

couplings were seen. This lead Glashow, Iliopoulos and Maiani (19) to propose that instead of a d quark (mass state), the weak interaction coupled to a combination of d and s quarks, defined by the Cabibbo angle θ_C: $d' = d\cos\theta_C + \sin\theta_C$. With the discovery of a greater number of quark species, this was extended to produce the CKM (Cabibbo-Kobayashi-Masawa) (20; 21) matrix combining the mass states into weak interaction flavor states:

$$
\begin{pmatrix} d' \\ s' \\ b' \end{pmatrix} = \begin{pmatrix} V_{ud} & V_{us} & V_{ub} \\ V_{cd} & V_{cs} & V_{cb} \\ V_{td} & V_{ts} & V_{tb} \end{pmatrix} \begin{pmatrix} d \\ s \\ b \end{pmatrix}
\tag{2.9}
$$

The analogy in the neutrino sector for the quark sector CKM matrix is known as the neutrino mixing matrix, of the Pontecorvo-Maki-Nakagawa-Sakata (PMNS) matrix (22; 23):

$$
\begin{pmatrix} \nu_e \\ \nu_\mu \\ \nu_\tau \end{pmatrix} = \begin{pmatrix} U_{e1} & U_{e2} & U_{e3} \\ U_{\mu1} & U_{\mu2} & U_{\mu3} \\ U_{\tau1} & U_{\tau2} & U_{\tau3} \end{pmatrix} \times \begin{pmatrix} \nu_1 \\ \nu_2 \\ \nu_3 \end{pmatrix}
\tag{2.10}
$$

The matrix U_{PMNS} can be written as

$$
U_{PMNS} = \begin{pmatrix} c_{12} & s_{12} & 0 \\ -s_{12} & c_{12} & 0 \\ 0 & 0 & 1 \end{pmatrix} \begin{pmatrix} c_{13} & 0 & s_{13}e^{-i\delta} \\ 0 & 1 & 0 \\ -s_{13}e^{i\delta} & 0 & c_{13} \end{pmatrix} \begin{pmatrix} 1 & 0 & 0 \\ 0 & c_{23} & s_{23} \\ 0 & -s_{23} & c_{23} \end{pmatrix}
\tag{2.11}
$$

where $c_{ij} = \cos\theta_{ij}$ and $s_{ij} = \sin\theta_{ij}$. The θ_{ij} are the mixing angles and δ is a CP-violating phase. The first part of the U_{PMNS} matrix corresponds to the solar neutrino oscillation. The second one corresponds to reactor neutrino oscillation, and the third matrix corresponds to atmospheric neutrino oscillation.

Oscillation experiments have the power to measure the extent to which the mixing of flavor states occurs. The approximate values of the PMNS matrix are (from(24))

$$
\begin{pmatrix} U_{e1} & U_{e2} & U_{e3} \\ U_{\mu1} & U_{\mu2} & U_{\mu3} \\ U_{\tau1} & U_{\tau2} & U_{\tau3} \end{pmatrix} = \begin{pmatrix} 0.8 & 0.5 & 0.1 \\ 0.5 & 0.6 & 0.7 \\ 0.3 & 0.6 & 0.7 \end{pmatrix}
\tag{2.12}
$$

The mass eigenstates interfere constructively or destructively as the neutrino propagates, resulting in oscillations of the flavor-state that are dependent on the length of the travel (L). Given this, the amplitude for a neutrino to oscillate from a flavor α to a flavor β

with energy E is given by:

$$\psi_{\nu_\alpha \to \nu_\beta} = \sum_i U*_{\alpha_i} e^{-im_i^2 L/(2E)} U_{\beta_i} \tag{2.13}$$

The probability of oscillation of this neutrino to oscillate from flavor α to flavor β is given by the square of this amplitude:

$$|\phi_{\nu_\alpha \to \nu_\beta}|^2 P_{\nu_\alpha \to \nu_\beta} = \tag{2.14}$$

$$= \delta_{\alpha\beta} - 4 \sum_{i>j} R[U*_{\alpha_i} U_{\beta_i} U_{\alpha_j} U*_{\beta_j}] sin^2(\Delta m_{ij}^2 \frac{L}{4E})$$

$$+ 2 \sum_{i>j} I[U*_{\alpha_i} U_{\beta_i} U_{\alpha_j} U*_{\beta_j}] sin(\Delta m_{ij}^2 \frac{L}{2E})$$

where $\delta m_{ij}^2 = m_i^2 - m_j^2$. It is easy to note that the oscillation probability is a function of L/E and that mass splittings δm_{ij} must be different from zero. Neutrino experiments using a well known neutrino beam can study oscillations looking for either the *appearance* of neutrino flavors ($P_{app} = P_{\nu_\alpha \to \nu_\beta}$) or the disappearance of neutrino flavors ($P_{disapp} = 1 - P_{\nu_\alpha \to \nu_\alpha}$) . Neutrino oscillation experiments attempt to determine these mixing angles and phase shift, as well as the mass differences between the different states. The current best fits for the mixing angles are (from (25) normal ordering values):

- $\theta_{13}/° = 8.50^{+0.20}_{-0.21}$; $sin^2\theta_{13} = 0.0218^{+0.0010}_{-0.0010}$ from $\bar{\nu}_e$ disappearance at reactor experiments Double Chooz (26), RENO (27) and Daya Bay (28).

- $\theta_{23}/° = 0.452^{+0.052}_{-0.028}$; $sin^2\theta_{23} = 0.452^{+0.052}_{-0.028}$, from T2K (29) measurements. It is unknown which quadrant it falls into.

- $\theta_{12}/° = 33.48^{+0.78}_{-0.75}$; $sin^2\theta_{12} = 0.304^{+0.013}_{-0.012}$ from KamLAND (30) data.

and mass mixing:

- $\Delta m_{21}^2 = 7.50^{+0.19}_{-0.17} \times 10^{-5} eV^2$

- $\Delta m_{31}^2 = 2.457^{+0.047}_{-0.047} \times 10^{-3} eV^2$

These mass mixing values also come from the global fits on (25)

2.3.3 Neutrinos Interactions

Experiments rely on charged particle detection. These particles are going to be the daughters of neutrino interactions with the detector. It is essential to understand through which

processes neutrinos interact with matter and which particles are created in these processes, so we can successfully get information of the incident neutrino. Neutrino scattering with heavy nuclei can occur in different interaction channels. Figure 2.1, reproduced from (1), shows how process come into play as neutrino energy E_ν increases in the range of 0.1 - 10 GeV (where most neutrino experiments operate). The plot shows charged-current neutrino and anti-neutrino scattering cross-sections, respectively. It represents the predictions of the NUANCE neutrino interaction generator (31) for the three categories whose contributions change as a function of increasing neutrino energy: quasi-elastic (QE), resonant (RES) and deep inelastic scattering (DIS) processes, as well as the total charged-current inclusive cross-section.

QE scattering dominates at lower energies and refers to processes where a neutrino interacts with one of the nucleons in the nucleus, producing a charged lepton as a result:

$$\nu_l + n \rightarrow l^- + p \tag{2.15}$$

$$\bar{\nu}_l + p \rightarrow l^+ + n \tag{2.16}$$

As mentioned above, the detectors can "see" only charged particles, which makes easy the identification and energy reconstruction of neutrino QE interactions. Anti-neutrino interactions will knock out a neutron which may not be visible initially, but it can be identified by sparkles due to small charge deposition from nuclear recoils after undergoing some scattering.

In the RES scattering, a resonant state will be produced due to the excitation of a nucleon during an inelastic collision. These excited states decay to their fundamental states producing a combination of nucleons and mesons. The resonant production in neutrino interactions represents a significant fraction of the total cross-section for the 1-10 GeV range:

$$\nu_l + N \rightarrow l + \Delta/N^* \rightarrow l + \pi + N' \tag{2.17}$$

For higher energies, 0.1 - 100 GeV the DIS can happen. In this scattering, the neutrino can penetrate the nucleon and interact directly with the quarks inside it producing many hadrons in the final state.
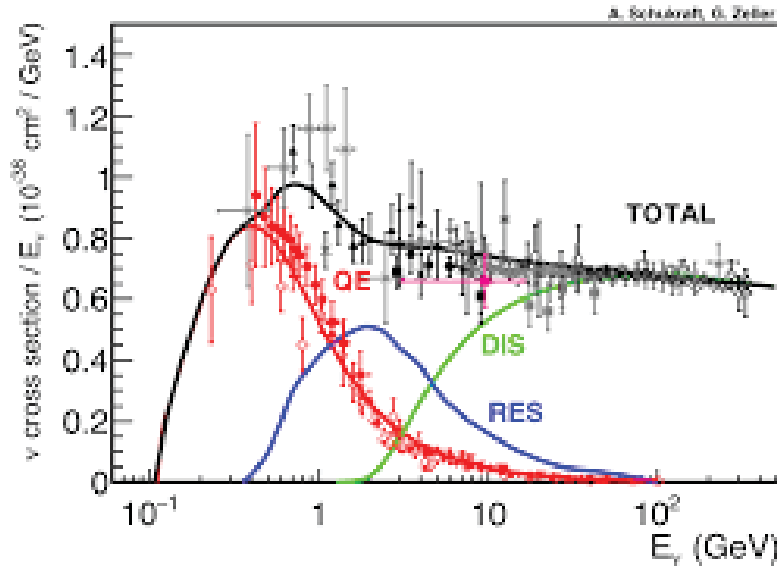
Figure 2.1: Total neutrino CC cross sections per nucleon divided by neutrino energy as a function of energy as reported in (1). Predictions for the total (black), the QE (red), resonant (blue) and DIS (green) are provided by the NUANCE generator. The quasi-elastic scattering data and predictions have been averaged over neutron and proton targets (isoscalar target).

2.3.4   Open questions in neutrino physics

With the discovery of neutrino oscillations, a whole new horizon emerged for particle physicists. New questions, new models, new ideas started to appear to accommodate the fact that neutrinos have a non-zero mass and still be consistent with the already known Standard Model. We are facing times now going Beyond the Standard Model.

With all this new research being done around neutrinos, we are pleased with the advancements made in the field, but it also brought us many questions that now need experimental answers, like:

- Are there new types of neutrinos?

- Do leptons violate CP?

- What is the right mass state order?

- Majorana or Dirac particles?

The next generation of neutrino experiments will hopefully answer all these still open questions in the particle physics world. Large neutrino detectors are being built using a

new technology for detection of these tiny particles: LArTPCs are an appealing kind of detectors that provides exceptional possibilities for studying neutrino interactions thanks to the bubble-chamber quality images they can give. They will contribute immensely to us to find the answer to all our questions.

CHAPTER 3

LOW ENERGY EXCESS

In the 90s, measurements from a variety of sources gave evidence of the occurrence of a fourth species of neutrino. With results from LEP (Large Electron-Positron Collider at CERN) that constrain the number of neutrinos that can interact weakly, the new possible fourth neutrino should be "sterile" meaning that it would not feel the weak force. In all measurements, this neutrino has not been directly observed, but it was deduced from the appearance of electron neutrinos that oscillated from a beam of essentially muon neutrinos. Assuming standard oscillations, the probability of muon neutrinos oscillate, as described in chapter 2, is $P = sin^2(2\theta)sin^2(1.27\Delta m^2 L/E)$, where θ is the mixing angle, Δm^2 is the difference in neutrino mass eigenstates squared, L is the distance traversed by the neutrino, and E is the neutrino energy .

The LSND experiment, a liquid scintillator detector located at Los Alamos National Laboratory, measured the appearance of electron antineutrinos using a beam of muon antineutrinos with different distances between the source and the detector. It measured the $\bar{\nu}_e$ candidate events by employing the coincidence of the immediate Cherenkov radiation signal from the positron and the delayed neutron capture by a hydrogen.

LSND observed a 3.8σ excess of electron antineutrinos over a baseline of several meters (32) that is compatible with the presence of sterile neutrinos ($\bar{\nu}_\mu \rightarrow \nu_{sterile} \rightarrow \bar{\nu}_e$). Using the muon antineutrino energy fo a few MeV, this points to a Δm^2 on the order of $1eV^2$, which contrasts with other observed mass parameters that are typically on the order of $10^{-6}eV^2$. The LSND experiment has limited statistics, and it also had a significant acceptance of cosmic background. The next experiments to test the results obtained should have higher statistics and comparable beam energy, baseline, and detector able to trace

$\bar{\nu}_e$ event candidates.

Another appearance experiment, the MiniBooNE at Fermilab, is a Cherenkov detector proposed to confirm or refute the observed excess seen in LSND. It consists of a spherical tank filled with 800 tons of mineral oil (CH_2), and the ν_e candidate signals are measured as a single isolated electron-like Cherenkov ring. In this way, MiniBooNE's systematics are completely different from the LSND's ones, but MiniBooNE can test the $1eV$ sterile neutrino hypothesis since it has a similar L/E with LSND. Both electron and muon (anti)neutrinos are observed via the charged current quasi-elastic (CCQE) process:

$$\nu_\mu + n \to \mu^- + p^+ \tag{3.1}$$

$$\nu_e + n \to e^- + p^+ \tag{3.2}$$

MiniBooNE is primarily a Cherenkov detector, and can easily discriminate between muons and electrons as it is possible to see in Figure 3.1. Those interactions described above are observed in MiniBooNE using PMTs along the inner wall of the tank (33).

Unlike in the LSND experiment, the expected signal to noise ratio is much lower in MiniBooNE. There are two dominant backgrounds of ν_e ($\bar{\nu}_e$) candidate events. The first one is the intrinsic ν_e ($\bar{\nu}_e$) contaminated in the beam. The majority of them are made by muon decay; hence, MiniBooNE constrains them by simultaneously measuring ν_μ charged current quasi-elastic events (CCQE) (34; 35), where measured ν_μ is related to intrinsic ν_e through the pion decay chain ($\pi^+ \to \nu_\mu, \mu^+ \to \bar{\nu}_\mu + e^+ + \bar{\nu}_e$) in their simulation. The second largest background is the misidentification of neutral current events, mainly NC π^0 production. π^0 decays in two gammas that are possible to be identified in a Cherenkov experiment. A single gamma signal inside a Cherenkov detector is a fuzzy ring, just like an electron signal. In the case of a π^0 decay, two fuzzy rings are identified, as it is shown in Figure 3.1. However, sometimes, the decays kinematics make two gamma rays look like one single gamma (asymmetric decay or gamma rays are too close). In this situation, the Cherenkov ring from one gamma ray is indistinguishable from an electron (positron). To take this systematic into account, MiniBooNE internally measured NCπ^0 production, and the measured information was used to correct π^0 production rates in the simulation (36).

MiniBooNE collected data during 10 years in neutrino and antineutrino modes, and it observed an excess in the 200 to $475MeV$ range in both runs configurations (2). These results are shown in Figure 3.2, where it is possible to notice the excess of data over the expected backgrounds. It should be noted that the dominating background at low energies
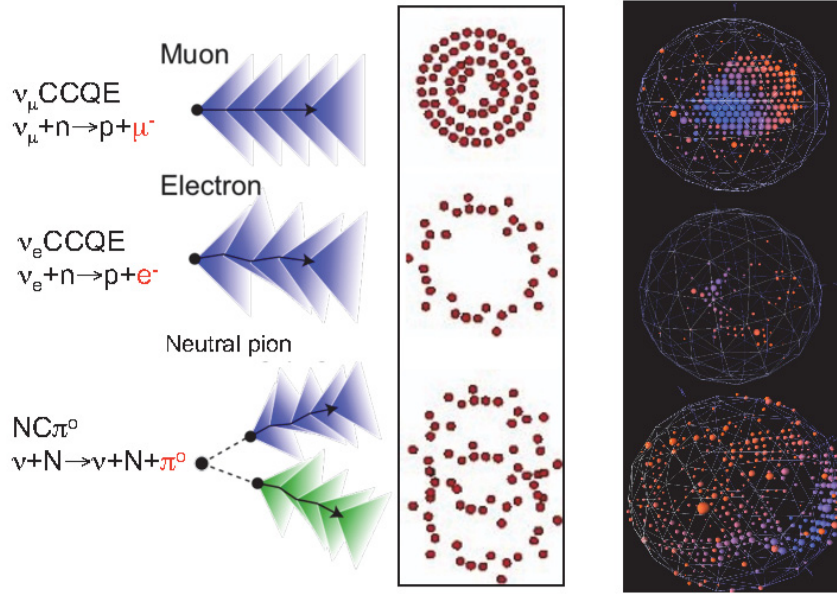
Figure 3.1: Examples of images obtained with the MiniBooNE cherenkov detector. Muons will appear as a defined circle, and electrons and gamma as fuzzy rings.

is the production of π^0s that decay strongly into two photons. As MiniBooNE is not suitable to distinguish electrons and photons precisely, a potential origin of this excess is the misidentification and mis-modeled π^0 created by muon neutrinos.

3.1 Future Plans

To understand the electron or photon nature of the MiniBooNE excess, as well as fully comprehend the origin of the LSND excess, Fermilab is in the process of construction and commissioning the Short Baseline Neutrino Program (SBN) with a different technology for neutrino experiments: Liquid Argon Time Projection Chambers (LArTPCs). The next chapter will describe this technology employed in the next generation of neutrino detectors that will be capable of, among other advantages, distinguishing between electrons and photons signals. Separating their signals will low this uncertainty, and it will assist with the still unsolved questions in the particle physics world. The SBN Program at Fermilab will consist of three LArTPCs exposed to the booster neutrino beam (BNB). With three detectors, it will be possible to make a comparison of near and far neutrino interaction rates allowing more accurate measurement of oscillation parameters. The three detectors that will be part of the SBN Program will be (37):

SBND : The closest to the beam source detector, and it is prepared to be installed. This 112 tons of liquid argon detector will be responsible for measuring the un-oscillated neutrino flux.

MicroBooNE : This 87 tons LArTPC is already operating and taking data since October 2015; this data is producing neutrino cross-section measurements, which will help explore the low energy excess.

Icarus : This will be the SBN far detector. Icarus is the first detector using the time projection chamber technology for neutrino experiments, and its collaboration studied neutrinos at Fran Sasso National Laboratory in Italy. This 500 tons LArtPC arrived at Fermilab and is being prepared for installation.

With these three experiments working together, SBN will be a fruitful territory for exceptional discoveries in the near future.
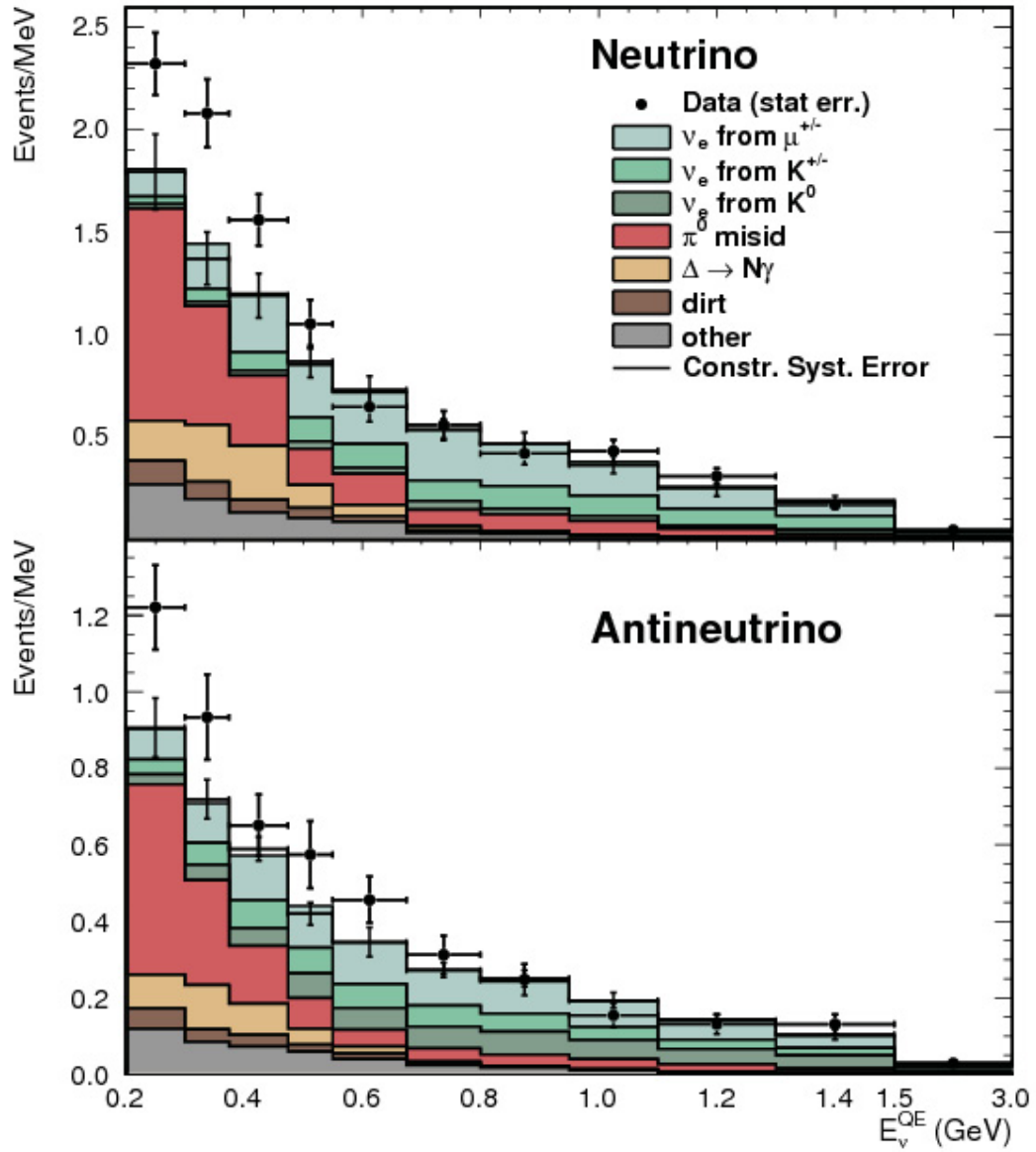
Figure 3.2: Final MiniBooNE oscillation results. (2). Reconstructed neutrino energy distribution of oscillation candidate events. The top plot is for the antineutrino mode, and the bottom for neutrino mode. Both modes show excesses in the low energy region (200 to $474 MeV$).

CHAPTER 4

LARTPC: LIQUID ARGON TIME PROJECTION CHAMBER

Many different types of experiments with different technologies were developed to study neutrinos. Since it is impossible to detect neutrinos themselves, all detectors are going to look to the particles that come out of a neutrino interaction with the target material. The technologies used will depend on the neutrino's energy range, will also depend on the neutrino's sources that will be studied and, in the experiment's goals. When charged particles interact with the medium, two things can occur ionization and/or light production (scintillation, Cherenkov). Experiments will be designed to detect as much information as possible from the interactions. We need detectors that can collect all possible information about the interactions with good calorimetric response, ability to do a 3D reconstructions of the track, proper resolution, capacity of making particle identification, and possibility of light collection. For all these reasons, the Liquid Argon Time Projection Chambers were chosen to be the next generation of neutrino detectors.

4.1 Why LArTPCs?

The first Time Projection Chamber (TPC) was proposed and designed by David Nygren in the late 1970s (38). Its original design was a cylinder filled with methane gas, and the first use of this new technology was in the PEP-4 experiment: an experiment at the SLAC Laboratory to study electron-positron collisions. In 1977, Carlo Rubbia adopted the idea of the TPCs to neutrino detection using liquid argon as the active medium in the ICARUS

experiment ([39](#)).

The choice of using argon for neutrino detection was because noble elements in the liquid form are advantageous for several reasons. They allow high electron mobility as noble elements do not attach electrons and permit them to have long drift times (depending on its purity). Since neutrinos do not interact easily with matter, we need dense mediums to increase the chance of interactions. Liquid argon is 40% denser than water and approximately 1000 times denser than gas. According to the Bethe-Block equation [4.1](#), the energy loss of a charged particle is proportional to the target material density, which shows that the increased density will reflect directly in the higher energy loss, intensifying the calorimetry capacity of this type of detectors. Additionally, the ionization energy of liquids is smaller than gasses in the order of tens of eV, which means that we have more ionization electrons for the same deposited energy. A minimum ionizing particle (MIP) will produce 55,000 electrons for every centimeter traversed inside the liquid argon. Still thinking about going around the fact that neutrinos have a small cross-section, we need big detectors filled with the target material. Liquid Argon is "cheap" to be produced since argon corresponds to approximately 1% of our atmosphere, making it a more viable choice for the construction of multi-tons scale neutrino detectors. Another great feature of liquid argon is the fact that it produces copious scintillation light, and it is transparent for this light produced. So, besides the collection of the ionization electrons, it is possible to collect the scintillation light, which is going to be an essential mechanism for triggering non-beam events.

Another possible noble element that could be employed in neutrino detection is the liquid xenon. As shown in table [4.1](#), xenon also has excellent features that could be important for neutrino experiments. This material is already utilized in dark matter detection; however, it costs considerably more than argon, making it not a suitable choice for large detectors.

4.2   How does a LArTPC work?

LArTPCs are quite similar to the old bubble-chambers, especially in tracking and energy resolution. However, now, these new chambers are connected to electronics that are capable of reading their imaging information. The "electronics" bubble-chambers, as they are sometimes called, are better in doing tridimensional tracking, calorimetry and they have a self-triggering mechanism that comes from the scintillation light collected in liquid argon. The operation of a Time Projection Chamber relies on the collection of free electrons produced by charged particles traveling across the liquid argon. These particles will ionize the

Table 4.1: Comparison between Liquid Argon and Liquid Xenon properties. The complete table can be found in (40).

Property	Argon	Xenon
Atomic No. (Z)	18	54
Atomic weight (A)	39.95	131.3
Maximum recoil energy (% of incident n energy)	9.5	3.0
Boiling point (K)	87.3	165
Density (g/cc)	1.4	3.0
Electron mobility (cm2/v*s)	400	220
Ion drift velocity at 1kV/cm (mm/μs)	2.2	2.4
Energy resolution (FWHM @662keV) scint.only (%)	8	8
Energy resolution, ionization+scintillation (%)	4 (expected)	4 (1.2 possible?)
Scintillation wave length (nm)	128	175
Scintillation yield (no. scintillation photons/MeV)	40000	42000
Fast decay time (ns)	7	4.3
Slow decay time (ns)	1500	22
(n, γ) propensity	medium	high
Neutron activation	medium	medium
Cost ($/gram$)	≈ 0.002	≈ 1.5
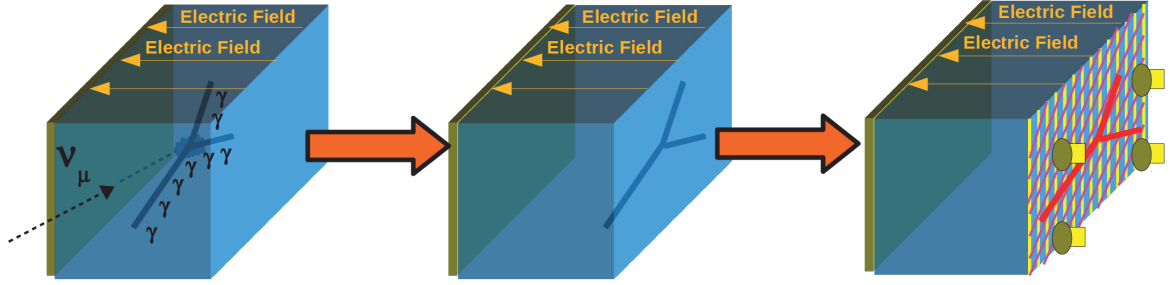
Figure 4.1: As the products of neutrino interactions travel through Ar, they will produce scintillation and ionization light. Photons are fast and will be detected by the photon detection system to provide the $t0$ of the event. Electrons will be drifted towards the readout planes.

argon atoms, and a uniform electric field will accelerate the free electrons towards a readout system, that could be either wire planes or pixel planes. In this thesis, the focus will be on the wire plane TPCs. To reconstruct events with 2D information, we need at least two wire planes (induction and collection) with different views or orientations. The time between when the interaction in argon occurred and the time where the electronics read the charge gives the third dimension, and it can be measured with a clock connected to the beam times or with a Light Collection System responsible for triggering the event. The light collection system will be placed behind the wire planes. The figure showed in 4.1 represents the concept of operation of a LArTPC.

4.2.1   Energy deposition in LAr: Ionization

As charged particles cross liquid argon, they will lose energy primarily by ionizing the atoms of this medium. The Bethe-Bloche equation 4.1 will describe the way that the energy is deposited in the material (8).

$$-\frac{dE}{dx} = Kz^2\frac{Z}{A}\rho\frac{1}{\beta^2}[\frac{1}{2}ln\frac{2m_ec^2\beta^2\gamma^2T_{max}}{I^2} - \beta^2 - \frac{\delta\beta\gamma}{2}] \tag{4.1}$$

This equation takes into account the number of unit charge of the ionizing particle (z), atomic number (Z) and the mass number (A) of the material, the density of the medium (ρ), the electron mass (m_e), the Lorentz factor (γ), the maximum kinetic energy that can be conferred onto a free electron (T_{max}), the mean excitation energy in eV (I), the density correction γ and a conversion factor ($K = 0.307075\frac{MeVcm^2}{g}$).

The dE/dx of a particle is one of the most primary measurements that a LArTPC can
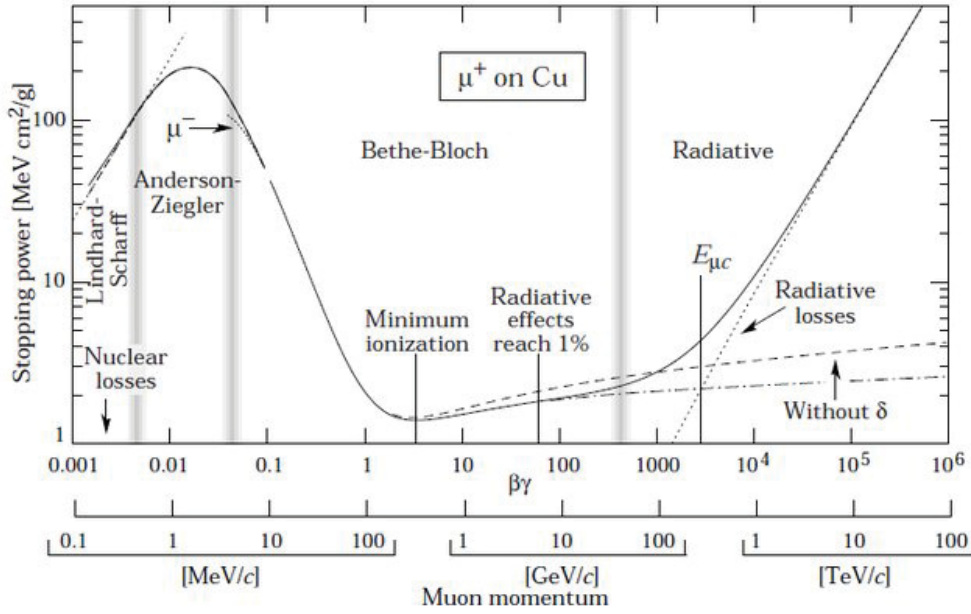
Figure 4.2: Density normalized energy loss, $dE/\rho dx$, vs momentum for muons in copper. The curve for argon would be similar, with a small re-scaling for Z/A.

make, and with it, it is possible to move forward with several analyses in the experiments.

Collisions that can ionize will occur randomly, so it is possible to parametrize their number k in a section of length s along the track with a Poissonian function.

$$P(k) = \frac{s^k}{k!\lambda^k}e^{-s/\lambda}, \tag{4.2}$$

where $\lambda = 1/N_e\sigma_i$, with N_e being the electron density and σ_i the ionization cross-section per electron. In most of the ionization processes in argon (about 66%), the collision will produce only a single electron (or ion pair) (**?**). However, in the other cases where the transferred kinetic energy is high enough, the primary electron will liberate one or more secondary electrons that will stay close to the original pair. In some other cases where the electrons receive enough energy to be ejected with high energy, there will be the formation of the so-called δ ray. The δ ray will leave a small track away from the original particle trajectory, as can be seen in this event display 4.3.

Effects that will affect the ionization charge

Purity and Electron Lifetime
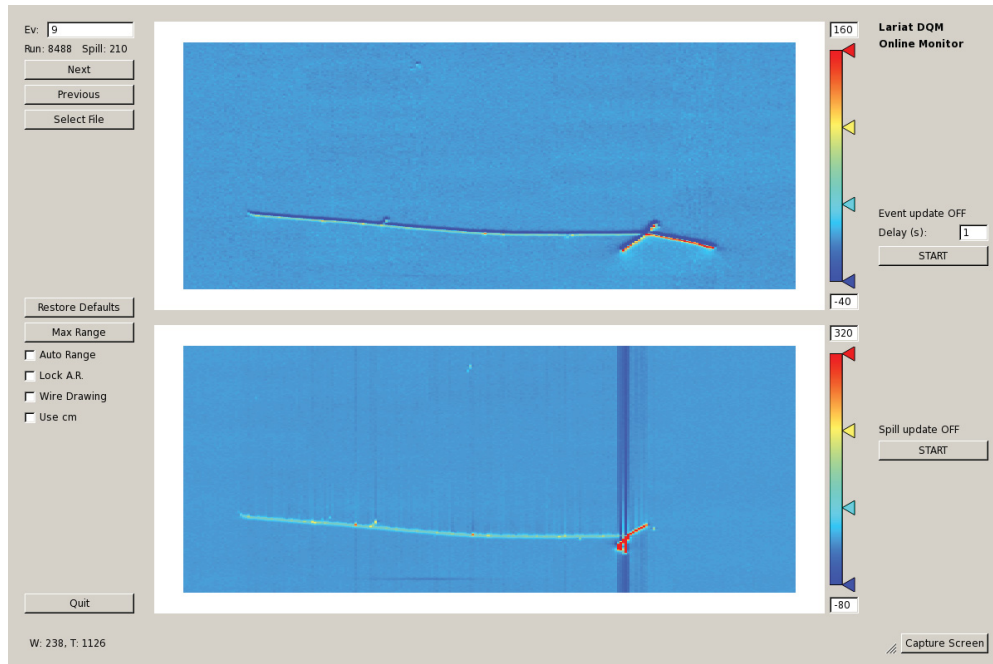
Figure 4.3: LArIAT's event display with a delta being emitted.

Electronegative contaminants present in liquid argon can quench the charge during its drift towards the readout system. The presence of oxygen, nitrogen, and water will affect the amount of charge that the detector will be able to collect, and it will affect every analysis that uses the TPC data. This topic will be discussed deeply in a separated chapter 6 due to its importance for this thesis.

Recombination Effect

Electrons liberated by the ionization process, when drifting through the liquid argon, can be quenched by electronegative contaminants (as explained in chapter 6) and can also be captured by the argon. This recombination can either occur between the free electron and its parent ionized argon, which is now positive or between the free electrons and other argon ions nearby from different ionization processes. Consequently, this charge that was liberated from the argon atom can be immediately re-collected by a nearby argon ion not reaching the readout planes reducing, though, the collected charge.

Two models are used to estimate this recombination effect: the Birks model (**?**) and the Box model (41). The first one implies a gaussian spatial distribution around the particle trajectory during the entire recombination phase and equal mobility for ions and electrons. The second model will assume that the electron diffusion and ion mobility are negligible.

For these two models, what will be affecting the expected fraction of electrons that will survive the recombination process are: the electron-ion pairs per unit length, the electric field they are submitted to, the average electron-ion separation and the angle of the particle relative to the direction of the electric field. Furthermore, in the Birks model, the electron diffusion will also be taken into account. For different energy ranges, these two models will present different results, as expected, due to their assumptions. Hence, usually, the Birks model is used to describe recombination for low dE/dx and the Box model for high dE/dx ranges. Since LArIAT uses a refurbished version of the ArgoNeut detector (as described in 5) with the same electric field, LArIAT uses the same parameters measured by the ArgoNeut collaboration (42) to correct for recombination.

Space Charge Effects

The electrons generated in the ionization process will drift faster to the wire planes than the ions towards the cathode due to the difference of mass. As there are more events in the TPC, especially from cosmic muons, there will be a build-up of positive charge - space charge - left in the detector that can distort the electric field in the chamber. This space charge distortion can affect the reconstruction of the event: if the electric field is modified, the drift velocity of the electrons will be different, and the drift time will be affected. Since the time is used as part of the 3D imaging, the position of the event will be incorrect reconstructed. For big LArTPCs detectors, especially the ones on the surface level, this effect can cause variations up to 5% in the localized electric field (43). For a small experiment, such as LArIAT, this is a sub-dominant effect.

4.2.2   Energy deposition in LAr: Scintillation

The energy deposited by a particle in LAr can also be used to excite Ar atoms. Scintillation light produced in liquid argon will peak at 128 nm, as shown in table 4.1. This ultraviolet light can be used as a trigger to the event, and the aim is to extend its use for calorimetric energy reconstruction. Figure 4.5 shows the emission spectra for argon as well as other noble elements (3).

The excitation processes will happen through two mechanisms, as shown in figure 4.4. These two mechanisms are both through the de-excitation of dimers (44):

$$Ar* + Ar \longrightarrow Ar*_2 \longrightarrow 2Ar + \gamma \qquad (4.3)$$
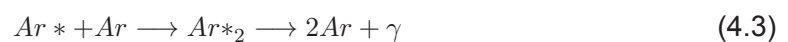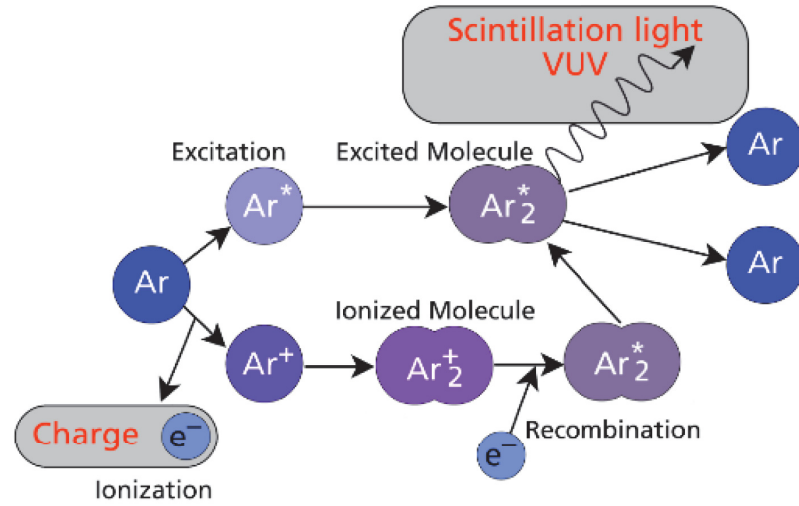
Figure 4.4: Liquid Argon scintillation process.

or

$$Ar^+ + Ar \longrightarrow Ar_2^+, Ar_2^+ + e^- \longrightarrow Ar*_2 \longrightarrow 2Ar + \gamma \tag{4.4}$$
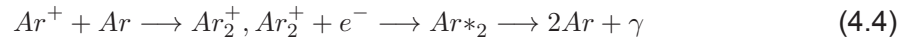
In the first case, "self-trapped exciton luminescence" befalls when a charged particle is absorbed on the atom, leaving the argon atom in an excited state. The excited argon will trap another argon atom in the bulk argon, creating a dimer state which de-excites and scintillates. In the second situation, "recombination luminescence" happens when a charged particle ionizes an argon atom by removing an electron. The charged argon ion will combine with another argon atom and recombines with the thermalized electron cloud, creating a dimer state which scintillates.

The decay of the molecule of $Ar*_2$ results in an emission of photons in the vacuum ultraviolet region (VUV) narrowly peaked at 128 nm. The argon molecule can be excited to two different states creating a dimer in either a singlet $^1\sum_u^+$ or a triple $^3\sum_u^+$ state. The scintillation photons from these two states have two different mean lifetimes: a singlet-fast with $\tau_F \approx 6ns$, and a triplet-slow with $\tau_S \approx 1.5\mu s$. The probability of being in a given state is different depending on the method that the excitation occurred. "Self-trapped exciton luminescence" will create a singlet state around 65% of the times, and a triplet around 35% of the times. "Recombination luminescence" will create a singlet and triplet with approximately equal probability. Since the first Ar electronic excited state is at a higher energy than the singlet and triplet excited states, Lar is transparent to its own scintillation light.

LAr scintillation signal $S(t)$ is thus the convolution of a gaussian distribution $f(t, \sigma)$ (with
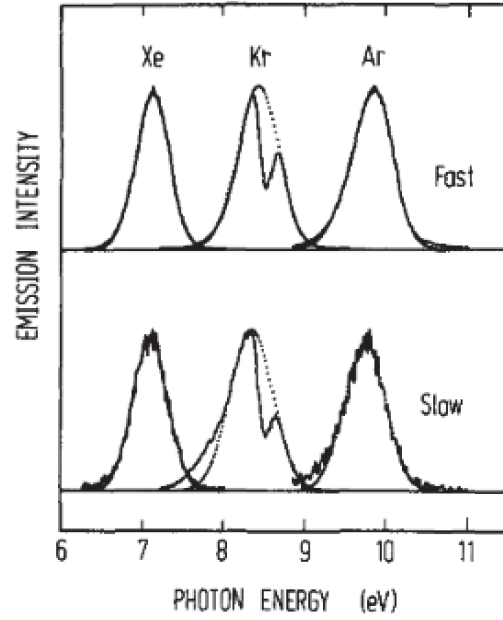
Figure 4.5: Emission spectra of the fast and slow components of xenon, krypton and argon (3). Dotted lines represent gaussian fits to the data.

$\sigma_G \simeq 4ns$), which represents the population of the excited states, with the double exponential distribution of the excited states decay via emission of scintillation photons, $N_\gamma(t)$. Equation 4.5 shows this.

$$S(t) = f(t, \sigma) \otimes N_\gamma(t)$$
$$f(t, \sigma) = \frac{1}{\sigma\sqrt{2\pi}} e^{-t^2/2\sigma^2}$$
$$N_\gamma(t) = \frac{A}{\tau_F} e^{-t/\tau_F} + \frac{B}{\tau_S} e^{-t/\tau_S} \tag{4.5}$$

where A and B parameters depend on the kind of the incident particle in LAr. For example, for MIP: $A = 0.3$ and $B = 0.7$. Detecting the scintillation photons from LAr in large neutrino detectors is technically challenging because of the difficulty in detecting the VUV photons efficiently. However, LAr has a high scintillation light yield, and it is transparent to its own scintillation light so that the photons can be detected at a significant distance from their source.

The LAr scintillation signal i_{out} that would be collected by a dedicated light collect system is the convolution between the photon time distribution $S(t)$ and the optical device response

$R(t)$

$$i_{out}(t) = S'(t) \otimes R(t) \tag{4.6}$$

Light Yield

The 128 nm photons do not have sufficient energy to excite the argon atoms, so this way, argon is transparent to the light that was just produced. Although there are a few factors that can impact the light yield inside a LArTPC. One possible factor that can reduce the light collected is the Rayleigh scattering. Photons in the VUV region will experience a scattering length of 66 m, which is short enough not to be a problem. The utilization of scattered light can be a problem if the experiment relies on light to trigger the event. The scattered light will make it difficult to combine the charge and light coming from the same particle and will be a problem to find the source of the light since its position will be affected by the scattering.

Another factor that will influence the light collected inside the detector is the presence of impurities such as nitrogen. These impurities can absorb or quench the 128 nm photons. Absorption will happen as the photons interact with the impurities. The quenching process will befall as the interaction of the impurities with the argon excimer, where the excimer transfers its excitation to the impurity and dissociates without emitting a photon. Since the triplets states live longer than the singlet states, quenching will happen mostly with triplets affecting especially the slow component of the light, reducing the scintillation yield and shortening of the scintillation time constants. The quenching process induced by nitrogen in liquid argon has been measured to be proportional to the nitrogen concentration, with a rate constant of $\approx 0.11\ \mu s^{-1}\ ppm^{-1}$. For the current generation of LArTPCs, a concentration of 2 ppm will give an attenuation length due to nitrogen of ≈ 30 meters [45].

Wavelength shifting

Scintillation light in liquid argon is collected usually with photodetectors such as Photomultipliers Tubes (PMTs) or/and Silicon Photomultipliers (SiPMs). These devices are sensitive to photons in the visible range of the spectra, being blind to the 128 nm ones. To be able to see these photons, wavelength shifters are going to be deployed in the detector to shift the light from 128 to ≈ 428 nm with the ratio of $\approx 1.2{:}1$ [46].

The most common wavelength shifter is the Tetraphenyl butadiene, known as TPB, and it is used in many experiments to shift VUV photons into optical. The main effect of TPB
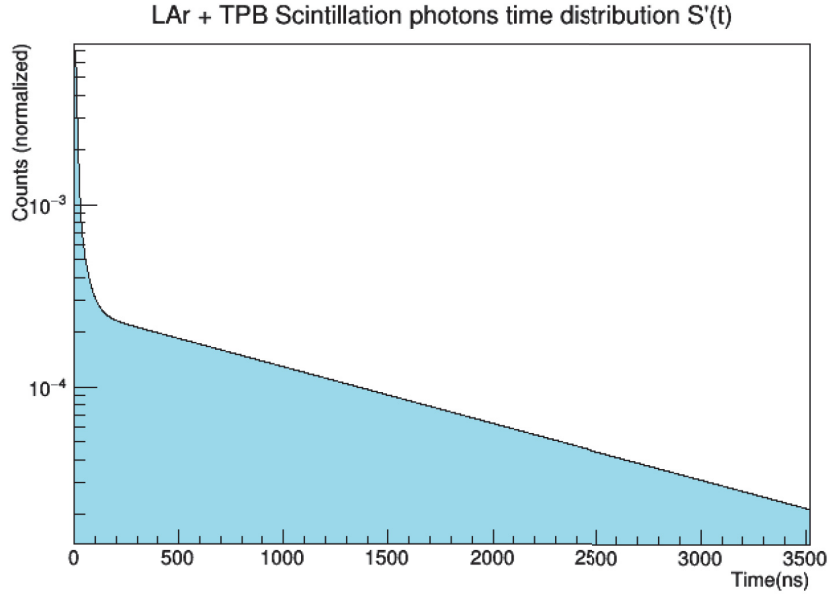
Figure 4.6: Expected LAr+TPB scintillation light photons time distribution.

wavelength shifter on the scintillation photon distribution is to add an intermediate decay exponential to the distribution ($\tau \approx 34$ ns). The new convoluted scintillation response $S'(t)$ is given by equation 4.7

$$S'(t) = f(t, \sigma) \otimes N'_\gamma(t) N'_\gamma(t) = \frac{A}{\tau_F} e^{-t/\tau_F} + \frac{B}{\tau_S} e^{-t/\tau_S} + \frac{C}{\tau_I} e^{-t/\tau_I} \tag{4.7}$$

where $A = 0.188$, $B = 0.738$ and $C = 0.074$ for a MIP in liquid argon. Figure 4.6 shows the expected LAr +TPB scintillation light distribution $S'(t)$.

The use of TPB in LAr experiments can vary. TPB can be evaporated and deposited directly onto the PMT surface to shift the wavelength os the photons as they arrive at the PMT, which allows the fast detection of the light coming directly from the event. TPB can also be evaporated into reflective foils that will be mounted on the inside walls of the sensitive volume of the TPC. This second technique leads to a higher and more uniform light yield. Hybrid systems with a mixture of both techniques are being considered for the next generation of LArTPCs detectors.

4.3 LArSoft: A framework dedicated to LAr experiments

LArSoft is a collection of detector-independent software tools for the simulation, reconstruction, and analysis of data from liquid argon experiments. This framework rests on the Fermilab-supported Analysis Reconstruction Tools (ART) framework, which is made to allow access to an event record. Non-liquid argon experiments also use ART for their frameworks. LArSoft allows users to write their physics code without worrying about the infrastructure. The common characteristics of LArTPCs allow the sharing of algorithm code across detectors of assorted sizes and configurations. The difference among experiments will be in their geometry descriptions made with gdml (Geometry Description Markup Language) files added to their specific versions of LArSoft. The software set offers an extensive selection of algorithms and utilities, including those for associated photodetectors and the treatment of auxiliary detectors outside the TPCs. (**?**)

The data is organized into a hierarchy of runs, sub-runs, and events. Run is defined by the scientist responsible for the data taking (shifter). For different beam specifications and different detector configurations, different runs are opened. Sub-run corresponds to a smaller cycle of data taking. Event is all that happened in a particular period of interest.

In LArSoft the shared repositories are based on C++ codes, and each experiment has its specific repository. Steps within a workflow are performed by experiment-written "modules," that are configured by a FHiCL (47) configuration file. In addition to modules, users may define "services" that can be used to provide global access to a particular resource within modules, such as detector geometry. Services can also be configured by the FHiCL configuration file.

The available algorithms will treat the full range of simulation and reconstruction, from raw waveforms to high-level reconstructed objects, event topologies, and classification. Figure 4.7 illustrates a simplified reconstruction workflow for the data processing used in LArSoft, and this chain will be described with more details bellow.
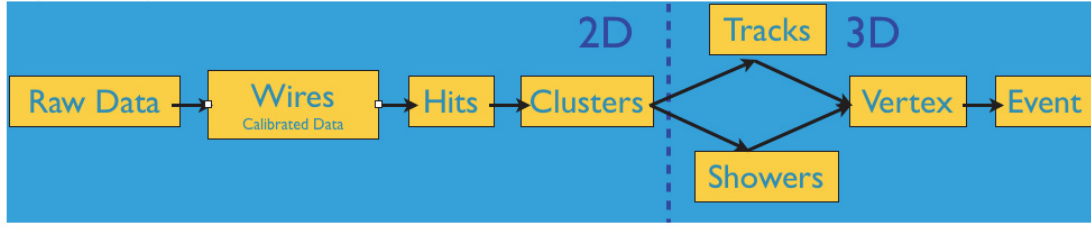
Figure 4.7: Reconstruction chain in LArSoft.

4.4 Event Reconstruction

The output data from the TPC consists of waveforms in the drift time of charge induced or deposited on the readout wires. The readout planes are mounted with different orientations and use bias voltages chosen for optimal field shaping. Each plane will give complimentary views of the same interaction as a function of the drift time, giving the required information for reconstructing a 3D image of the event. The signal response obtained with these planes will possess different shapes depending on the purpose of the wire plane. Induction planes will provide bipolar signals due to the electrons approaching and departing the planes. The collection plane will respond with a unipolar signal due to the collection of the charge. These signals will go through a series of steps until they are ready to be used for analysis.

Deconvolution

Since the signals obtained from the detector have different shapes, as mentioned above, and are subjected to electronics response, there is the necessity of correcting these effects from the detector. The deconvolution process will try to correct the signal that was read out by the data acquisition system by removing the field response from the raw information in order to create a similar and unipolar signal for induction and collection views from the LArTPC. The basic deconvolution process is already implemented in LArSoft, and it is explained using the equations shown in 4.8 and 4.9.

$$W(t) = Q(t) * F(t) * E(t) \tag{4.8}$$

The time-dependent ionization charge can be recovered by deconvolution:

$$Q(t) = \mathscr{F}^{-1}\left[\frac{\Phi(f) * \mathscr{F}(W(t))}{\mathscr{F}(F) * \mathscr{F}(E)}\right] \tag{4.9}$$

where $\mathscr{F}$ is the Fourier transform and $\Phi(f)$ is a filter function. For LArIAT, cross talk was
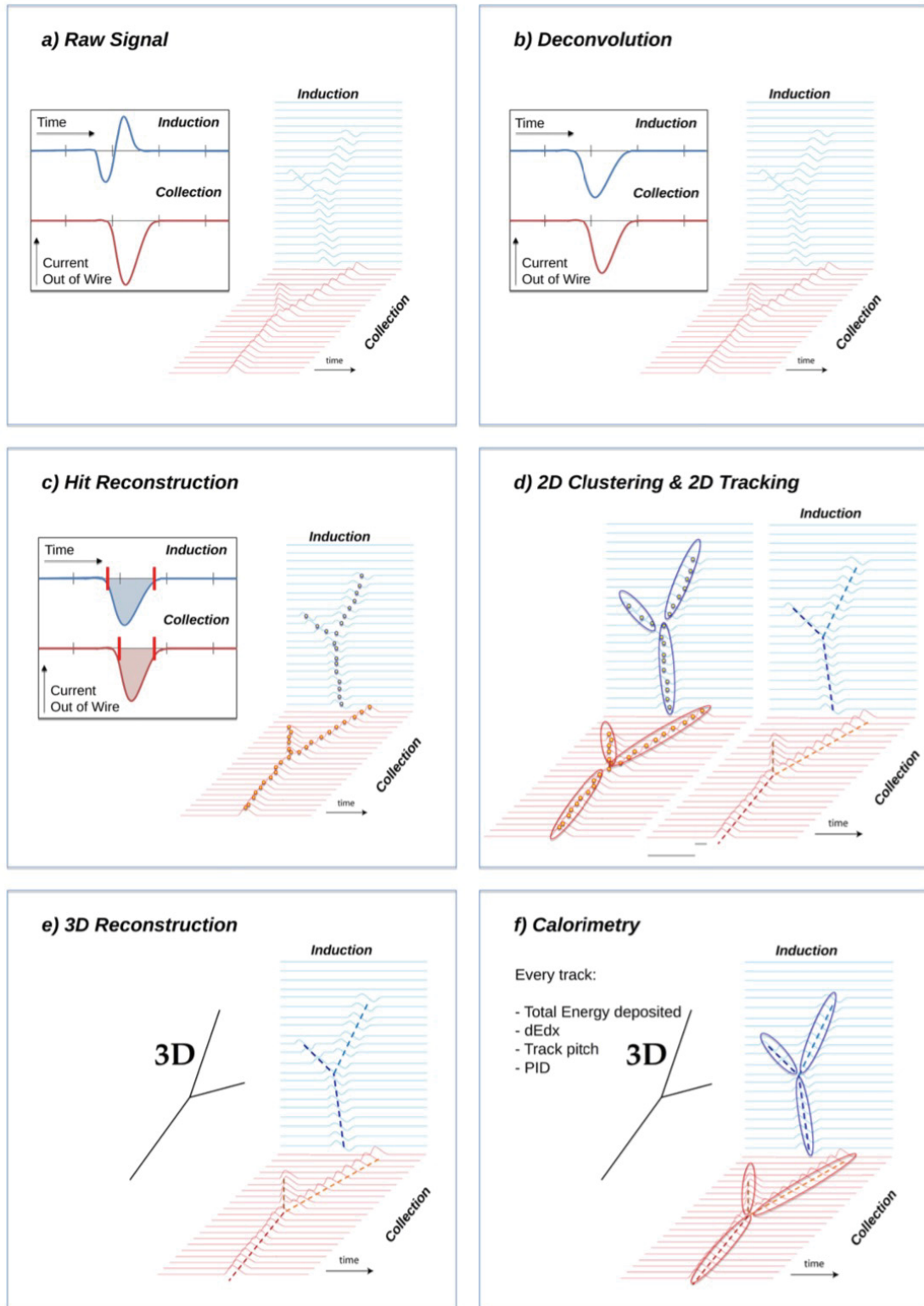
Figure 4.8: Typical signal processing workflow in LArSoft (4)

minimal, so no noise filtering was necessary.

Hit Reconstruction

Once the TPC waveforms are deconvolved, a peak finder looks for bumps in wire data (energy deposition) and fits these peaks with Gaussian curves. The goodness of the fit is stored in a parameter to be associated with the data product. Having the parameters of the fit allows the user to, later on, discard reconstructed peaks with bad fits, such as those due to noisy wires. Other parameters, such as the peak time and area under the Gaussian fit (charge), are then stored. The result of this process on one bump is a single reconstructed "hit."

It is worth mentioning that the height and width of the hit will depend on the topology of the event. For example, a particle that its trajectory is parallel to the wire planes will leave a series of narrow individual hits on consecutive wires. Moreover, a particle traveling with an angle between its trajectory and the readout planes will leave long and wide hits on very few wires. The height of the hits and their integral will be proportional to the charge collected by the wire so that it will depend on the particle type.

Clustering

With hits reconstructed, more complex objects can be formed by grouping hits based on particle topology. Particle topology can be line-like groups that will be called track-like (e.g. muons, protons, charged pions, etc.) or shower-like (e.g. electrons and photons). The track-like clustering will be done by an algorithm that will step along collections of hits in a $2D$ wire-time space for each plane and will produce trajectory points by combining sequentially nearby hits, updating the direction of the trajectory along the way.

Whether or not a new hit gets added to the trajectory will depend primarily on the charge of the hit compared to the average of recently-added hits; how well the hit aligns with the current trajectory (goodness of fit of the candidate hit); and the angle between the two lines formed from a small collection of hits before and after the hit that is being considered. All the hits added to a trajectory are then aggregated into a single cluster.

Track Reconstruction

The collection of $2D$ clusters from both wire planes are then provided as inputs to a $3D$ track-finding algorithm (48). To do this, a $3D$ trajectory is defined such that it minimizes a

measure of the distance separating its $2D$-projections onto wire planes and the actual $2D$ hits observed for all wire planes simultaneously. Tridimensional tracking can use multiple clusters in one plane, but it can never separate them into smaller groups of hits. The outcome is a collection of $3D$ track objects, each characterized by some number of xyz-points or "space points."

Calorimetry

The final level of event reconstruction in LArTPCs is to obtain calorimetric information for the objects from the previous steps (track or shower). A many-steps procedure is needed to get the energy deposited in the TPC from the charge seen by the wires from each plan at a time. For every hit from each object, the calorimetric algorithms calculate the charge seen by every wire by integrating the gaussian fit. This charge will be then corrected by the electron lifetime, the electronic noise of the considered wire, and the recombination effect. Finally, an overall calibration of the energy will be performed, and the calorimetric information for the given object is assigned.

CHAPTER 5

LARIAT: LIQUID ARGON (TPC) IN A TESTBEAM

A full characterization of the LArTPC technology performance is considered of fundamental interest for the development of the Intensity Frontier Program in the U.S., especially for the Short and Long baselines programs for precise neutrino oscillation physics and proton decay searches.

The LArIAT program consists of a full calibration of the Argon TPC in a dedicate beamline. The experiment is focused on the study of all the charged particles expected to come out of neutrino interactions in Liquid Argon; therefore, the detector is placed on a beam of charged particles of known type and momentum, in the range of 0.2 to 1.4 GeV/c. The aim is to characterize signals from different particles in a LArTPC and to find criteria to distinguish among them. The charged particle test beam will help to develop and validate the off-line software tools of particle identification, calorimetry, and event reconstruction without relying solely on simulations.

The LArIAT detector lives in the Fermilab Test Beam Facility (FTBF), where the experiment characterizes a beam of charged particles in the Meson Center beamline.

5.1 The Beam

The beam that arrives in LArIAT's detector starts at the Fermilab accelerator complex, and this journey begins with a beam of protons. Firstly, hydrogen is ionized to form H^- ions that will be boosted to 750 keV by a Cockroft-Walton accelerator and inject into the Linac (linear accelerator) that increases their energy up to 400 MeV; then, H^- ions pass through a carbon foil and lose the two electrons. The resulting protons will then be injected in a
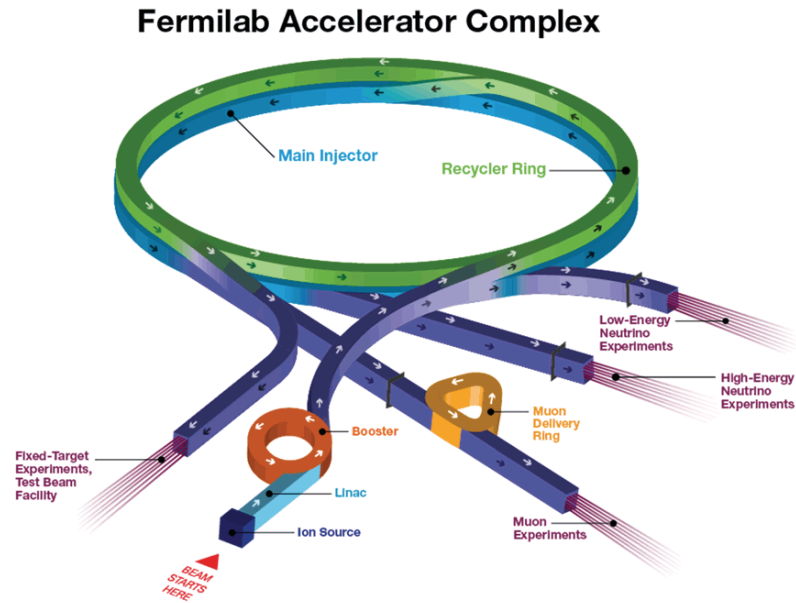
Figure 5.1: Fermilab's accelerator complex

cycling synchrotron called Booster; at this stage, protons have 8 GeV of energy and will be compacted into bunches. The next step of acceleration is the Main Injector, a synchrotron that accelerates the bunches up to 120 GeV, and here several bunches are merged into one and are ready for delivery. Figure 5.1 shows the Fermilab Accelerator Complex.

The Fermilab accelerator complex works in supercycles of 60 seconds in duration. A 120 GeV primary proton beam with variable intensity is extracted in four-second "spills" and sent to the Meson Center beamline. When the beam arrives at FTBF, the primary beam is focused onto a tungsten target to create LArIAT's secondary beam, which is composed mainly of positive pions. The secondary beam impinges then on a copper target within a steel collimator inside the LArIAT experimental hall (MC7) to create the LArIAT tertiary beam.

5.2 The Tertiary beamline detectors

To determine which particles and their momentum before they enter the TPC, LArIAT relies on a set of detectors that will select and identify them. Figure 5.2 shows the detectors and
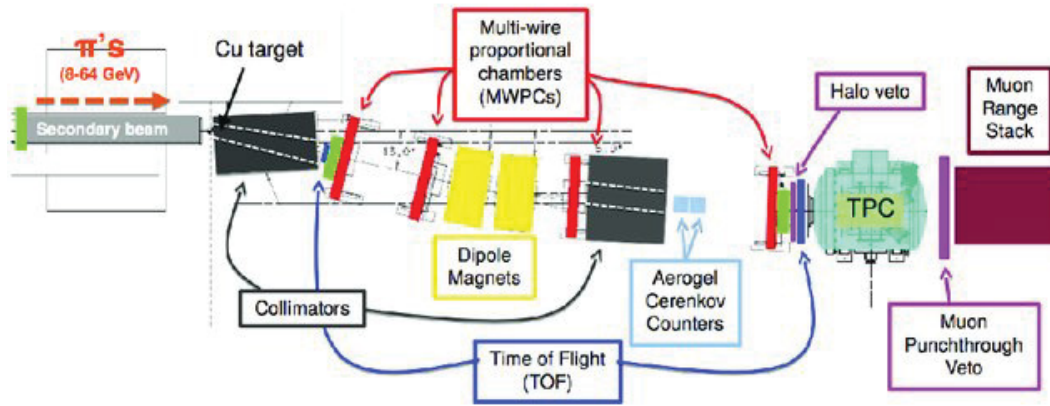
Figure 5.2: LArIAT's tertiary beam line detectors.

their positions in the tertiary beamline.

The tertiary beamline starts with the secondary beam (mostly pions) hitting a copper target. A new beam is just formed, and it will first pass through a steel collimator that selects particles with a $13°$ production angle. The particles will then find a series of detectors to characterize the beam.

5.2.1 Time of Flight (TOF)

The first instrument from the beamline that the particles will hit is the upstream detector of the time of flight system. As the name states, this set of two devices will measure the time of the flight of the particles before they enter the TPC. Heavy particles will, logically, take longer to travel, and lighter particles will do it faster.

The system is composed of two scintillator paddles, one upstream (before the middle of the beamline - USTOF) and one downstream (after the middle of the beamline - DSTOF). The first detector is a 10 x 6 x 1 cm scintillator section, read out by two PMTs positioned on the beam left side, which collects the light from light guides attached to all four edges of the material. The second paddle is a 14 x 14 x 1 cm scintillator section read out by two PMTs on the opposite end of the scintillator. During Run III the scintillators were readout by four PMTs. The scintillator pieces were made as thin as possible to reduce the energy loss due to ionization by the particles inside the detector. The USTOF is rotated 13°, and the DSTOF is rotated 3°, both in the XZ plane.

A CAEN 1751 digitizer module is used for digitizing the signal coming from the PMTs at a sampling rate of 1 GHz. The 12 bit samples are stored in a circular memory buffer. When

a trigger is issued, data from the TOF PMTs are recorded to output in a 28.7 μs windows starting approximately 8.4 μs before the trigger time.

5.2.2   Multi-Wire Proportional Chambers and Bending Magnets

After hitting the USTOF detector, a particle will pass through the Multi-Proportional Chambers (or Wire Chambers - WC) and the Bending Magnets. The combination of the WCs and the magnets will make possible the measurement of the momentum of the particles before they enter the cryostat.

There are four wire chambers in the beamline: two before the bending magnets (WC1 and WC2) and two after the magnets (WC3 and WC4). Each wire chamber is composed of two wire planes, one vertical and one horizontal, with 128 wires spaced 1 mm apart. Inside the wire chamber, there is a mixture of 85/15 argon/isobutane, which allows ionization of electrons when a charged particle passes through the active volume. The two first wire chambers are rotated 13°, and the two last are rotated 3° in the XZ plane. The wire chamber's raw signals are amplified, shaped, and discriminated by ASDQ chips. The chips are read by a Time-to Digital Converter (TDC) with 64 wires per TDC, making 4 TDCs per wire chamber. Each wire readout lasts for 1024 samples, with each sample representing approximately 1.18 ns. This TDC provides a fast OR output that can be used in a first-level trigger.

Two dipole magnets are utilized to bend the charged particle beam as it travels through the beamline. The first magnet is rotated by 10.5° and the second by 5.5°, both in the XZ plane. Choosing the current and the polarity in the magnets is possible to select the particle's charge and momentum before they enter the TPC. The magnets could hold a maximum of 100 A that was used only when the beam was sent to the detector hall to avoid overheating. Chilled water lines passed through the magnets, and fans were kept on to help with protecting the magnets from overheating. Right after the third WC, is another collimator that shields WC4 and the DSTOF from particles that could have been created by a particle that impinged upon the steel of the magnets.

To measure the momentum with the combination of the four WCs and the bending magnets, the hits in the wire chambers and the current in the magnets will be recorded. In the most simplistic scenario, only one hit on all wire chambers is recorded during a single readout of the detectors systems. This way, the hit positions on the first two wire planes are used to form a trajectory before the bend, and the hits on the last two wire planes are used to form a trajectory after the bend. With the angles formed in the XZ plane between

Figure 5.3: Part of the beamline's detectors showing one wire chamber and the bending magnets (yellow)

the two trajectories, it is possible to calculate the Z component of the particle's momentum as follows:

$$P_Z = \frac{B_{eff}L_{eff}}{3.3(sin(\theta_{DS}) - sin(\theta_{US}))} \qquad (5.1)$$

where B_{eff} is the effective maximum field in a square field approximation, L_{eff} is the effective length of both magnets combined, θ_{US} is the angle of the z axis of the upstream trajectory, θ_{DS} is the angle of the z axis of the downstream trajectory. 3.3 c^{-1} is the conversion factor from [T.m] to [MeV/c]. If there are multiple hits in a single wire plane or if there is an absence of hits in one or more wire chambers, things get more complicated, and other techniques will be applied.

5.2.3   Cosmic Ray Paddles

To select cosmic ray events, LArIAT has a cosmic ray trigger composed of two sets of cosmic ray paddles (or cosmic towers). One tower sits upstream of the cryostat and the other downstream, one beam-right and the other beam-left around the cryostat, as shown in figure 5.4. The cosmic towers are composed of two sets of paddles: an upper and a
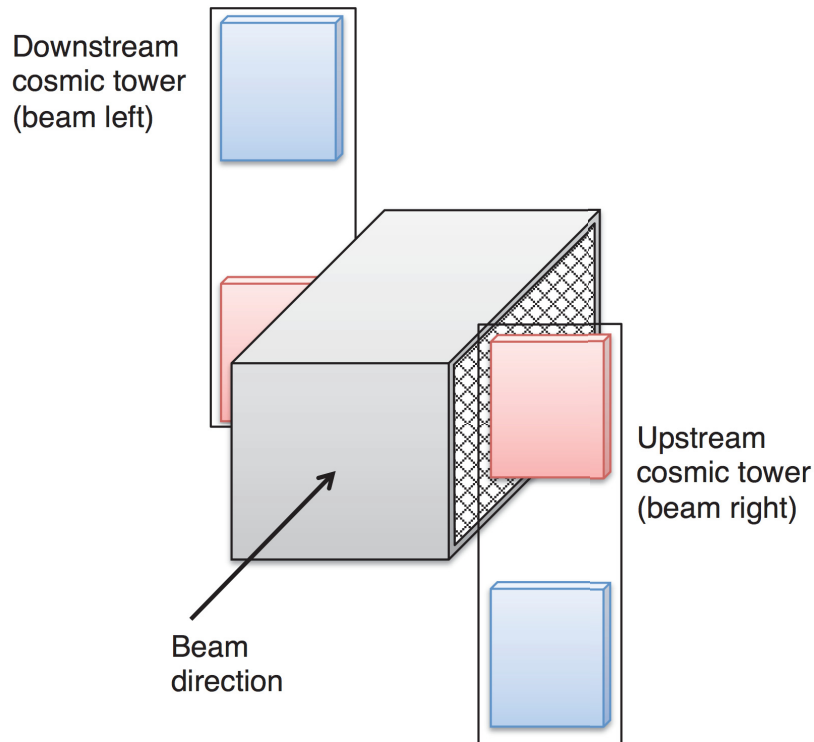
Figure 5.4: Scheme of the cosmic ray paddles outside LArIAT's cryostat.

lower. Each set of paddles is constituted of four paddles: a pair sitting horizontally and a pair sitting vertically. The sets sitting horizontally will provide a veto for downward-going cosmic ray air showers. The sets that sit vertically will select muons that cross the whole TPC along one of its diagonals and cross the anode and the cathode inside the chamber. A logical "AND" of discriminated signals of the vertical paddles from either end will make this selection.

The cosmic rays selected by the cosmic trigger can be used for the calculation of the electron lifetime, which is related to the concentration of electronegative contaminants in the liquid argon and is described in chapter 6. The crossing muons can also be used to provide an in situ calibration sample for the calorimetry and electric field studies such as the channel calibration due to different wire responses and calibration of the calorimetric response of the TPC.

Each paddle is made of a scintillator material with a trapezoidal shape, and they are all enclosed in an aluminum case to ensure that light from outside goes in. The scintillation light will be readout by wavelength shifting optical fibers, which go along the long side of the paddle and are optically coupled to a low voltage, Zener diode Hamamatsu H5783 PMT.

Signals from the PMTs will be amplified and discriminated by a custom PMT amplifier and discriminator (PAD) circuit, attached at one edge of the paddle. The discriminated signal is transmitted via a CAT5 cable to a Control and Concentrator Unit (CCU), which produces an ECL output for the trigger. The CCU also renders high voltage to the PMT and the threshold level for the PAD circuit.

The paddles used in LArIAT came from the CDF detector. The selection was made after measuring the efficiency and accidental rate using a muon telescope. The paddles with the highest efficiency and lowest single count rates were selected to be used in LArIAT.

5.3   LArIAT's Cryostat

The main part of the experiment lives inside the cryostat. This place is were the TPC, and the liquid argon will be placed, and the tests for the next generation of neutrino experiments will happen.

5.3.1   The Cryogenic system

LArIAT uses ArgoNeuT's cryostat (49) to keep argon at 87 K, however, with some modifications to allow the operation in a charged particle test beam. The current version of the cryostat is shown in figure 5.5, and it will be described in this section among the purification system, details of the TPC, and the light collection system.

5.3.2   The Cryostat

LArIAT's cryostat consists of an internal volume, which involves the purified liquid argon and an external volume working as a vacuum jacket with layers of aluminized mylar superinsulation. The main axis of the cryostat is horizontal and oriented parallel to the beam. Both vessels, the internal and external, are cylindrical with convex end caps. The inner vessel has 76.2 cm in diameter and 130 cm in length, carrying about 550 L of LAr, which corresponds to 0.76 ton. To access the inner volume, the cryostat has a "chimney" distending from its top at mid-length, visible in figure 5.5, which works as an access path for signal cables from the LArTPC and the internal instrumentation, as well as for the high voltage feedthrough.

Several modifications were made to adapt the ArgoNeuT cryostat to its use in the FTBF. The previous version of the cryostat had end caps made of stainless steel and were 4.8 mm
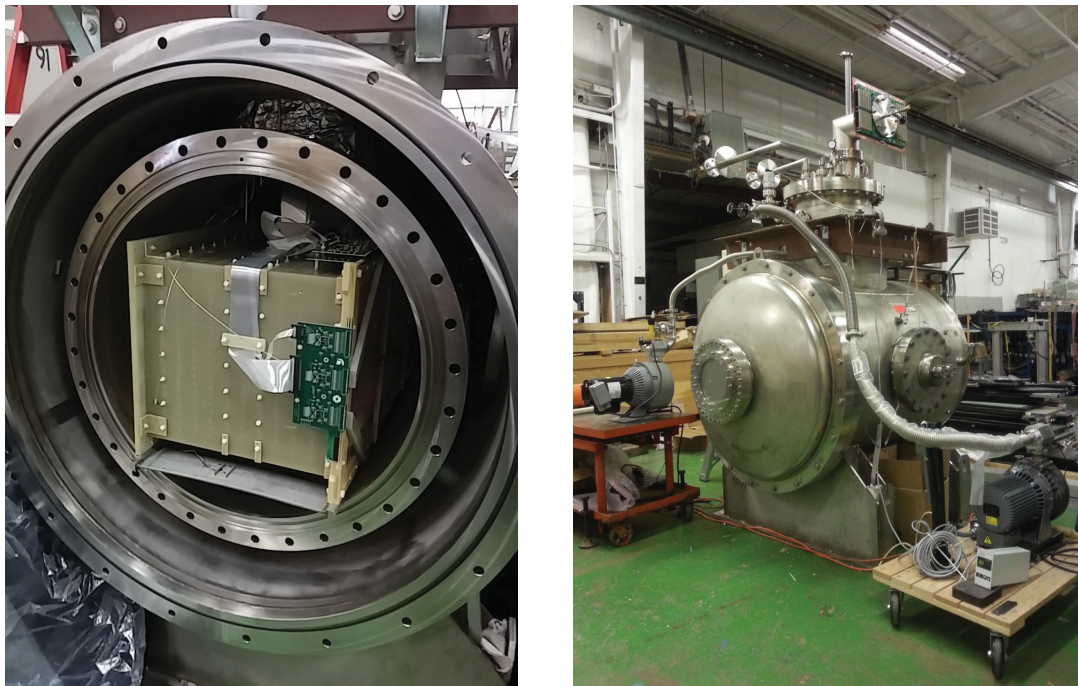
Figure 5.5: LArIAT's cryostat. Left: TPC sitting inside the open cryostat. Right: Cryostat closed and is possible to see the "chimney" used to access the inner volume

thick. To minimize the quantity of material before the TPC's active material, a flange was installed on the front of the outer vessel, and a 22.9 cm diameter beam window was placed at its center. The "excluder", a hollow concave volume, was installed on the inner vessel's front end cap to minimize the amount of liquid argon without instrumentation upstream to the TPC. With all these modifications, the total thickness of the unistrumented region upstream of the TPC's active volume was reduced from 1.8 radiation lengths to less than 0.3.

The ArgoNeuT detector did not have a light collection system, and hence for LArIAT, it was necessary to add CF-flanged apertures to the side ports of both the inner and outer cryostat vessels to accommodate signal and high voltage bias connections. Section 5.4.3 will detail LArIAT's light collection system.

5.3.3   Liquid Argon Purification System

LArIAT does not have a recirculation system for the liquid argon, which forces the experiment to get argon delivered every week. The commercial dewer outside the detector hall is filled using research-grade liquid argon with impurities < 1 ppm by the vendor. The acceptable contamination is only 100 ppt, making additional filtering necessary for the successful run of the detector.

From the external dewar to the cryostat, the argon passes through a purification system, which is based on the Liquid Argon Purity Demonstrator (LAPD) (50). The purification system consists of a single 77 L filter filled halfway with a 4 Åmolecular sieve. The sieve can remove water and small amounts of nitrogen and oxygen. The remaining volume of the filer contains BASF-CU-0226 S, a highly-dispersed copper oxide impregnated in a high surface-area alumina, which is able to remove oxygen and some water. The filter is insulated with a vacuum jacket and aluminum radiation shields.

The liquid argon purity inside the TPC is monitored, as described in 6, and according to the value obtained with this method is possible to know if the filter needs to be regenerated or not. When required, the regeneration process is done with the filter in place using a flow of argon gas that is heated to 200°. Once at 200°, a small flow of hydrogen is mixed into the primary argon flow and exothermically combines with oxygen captured by the filter to create water (50).

After filtering, the argon is pumped through the bottom of the cryostat into the inner vessel. During operation, the liquid argon in the cryostat boils and is vented to the atmosphere. Once the liquid level decreases below a threshold, more argon is pumped from the commercial dewer through the filtration system and into cryostat to refill it. This guarantees the cold electronics and high voltage feedthrough connections are fully submerged. During regular operations, refilling the cryostat happens many times a day. Argon levels, temperature, pressures, and filling stages are all monitored in real-time. The monitoring page can be seen in figure 5.6.

5.4   LArIAT's Time Projection Chamber

The TPC used in LArIAT is a rectangular box with an active volume of dimensions 47 cm (drift distance) x 40 cm (height) x 90 cm (length) containing 170 liters or 0.25 ton of liquid argon.

5.4.1   Cathode and Field Cage

A high voltage feedthrough on the top of the LArIAT cryostat passes the high voltage to the cathode; the purpose of the high voltage system is to drift the free electrons create by ionization of charged particles in the liquid argon towards the wire planes. The power supply utilized in this system is a Glassman LX125N16 (51) able to generate up to -125 kV
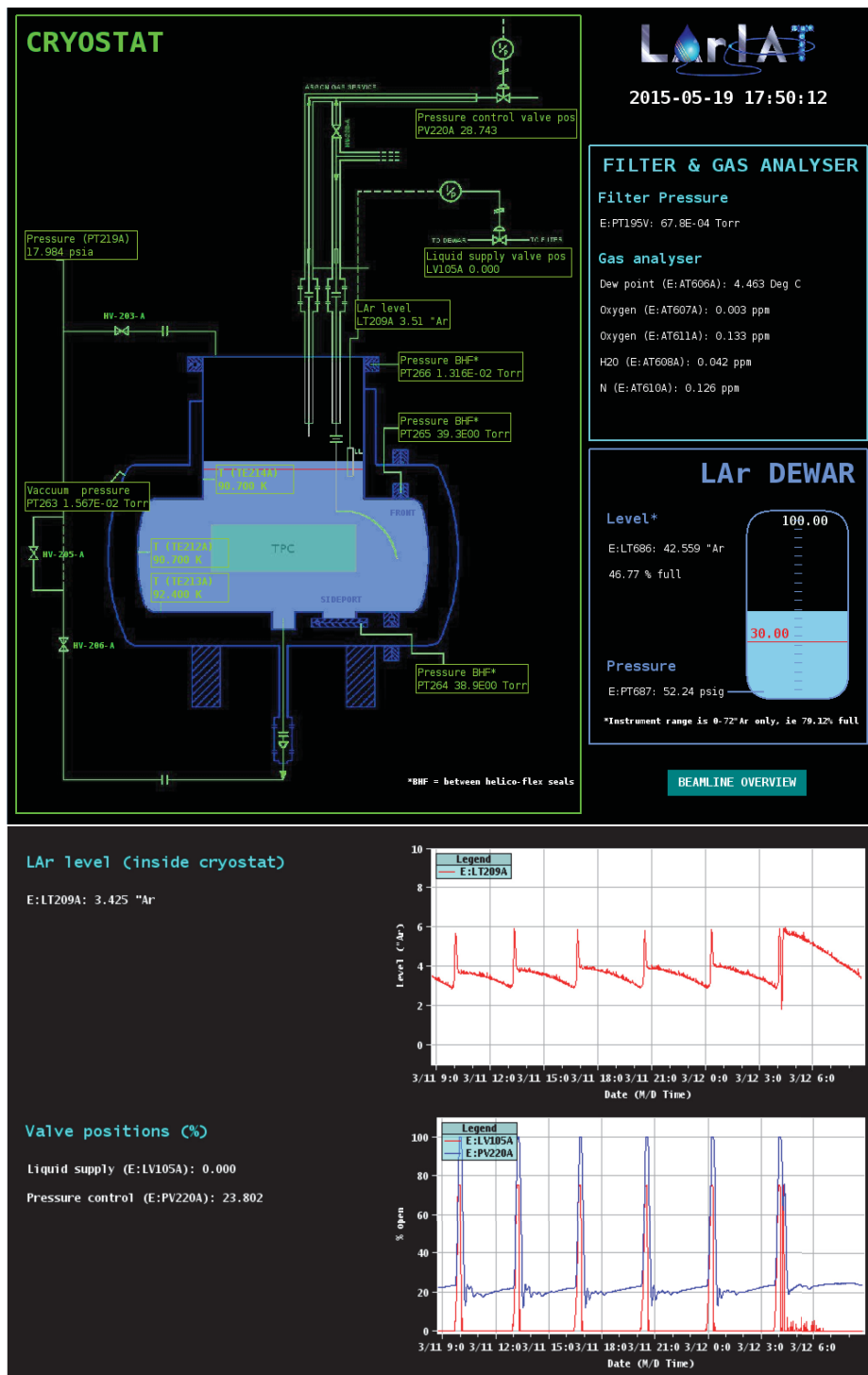
Figure 5.6: Screenshot of LArIAT's monitoring cryogenic system. The periodic nature of LAr level indicates refilling of the cryostat due to boiled off liquid argon

and 16mA of current although operated with -23.1 kV during LArIAT's runs. High voltage cables connect the power supply to a series of filter pots before reaching the cathode.

The field cage is composed of twenty-three parallel copper rings enclosing the inner walls of the G10 TPC structure. A system of voltage-dividing resistors connected to the field cage rings steps down the high voltage from the cathode to form a uniform electric field. The electric field over the entire TPC drift volume is 486 V/cm.

Enclosing the TPC, there are the cathode and the field cage structures. The rectangular field cage of the TPC is composed of copper-clad G10 pieces, with 1.0 cm wide, horizontal copper strips, with gaps of 1.0 cm; the G10 pieces form the outer walls of the TPC. The four inner walls of the field cage are connected electrically, such that each strip forms a complete loop around the drift volume. Four 1 GΩ resistors are arranged in parallel between the pieces of the field cage, for an effective strip-to-strip resistance of 250 MΩ. The voltage changes uniformly from the cathode to the anode, providing a uniform electric field throughout the TPC active volume. The cathode for the first two running periods of LArIAT was composed of a single piece of copper-clad G10 with a copper area that exactly matched the aperture of the field cage structure. In subsequent LArIAT runs, as a test of a design proposed for the SBND experiment, the first cathode was replaced with a cathode made of stainless steel mash.

The TPC has three drift regions with different electric fields, as shown in figure 5.7. The main drift region, the one where the interactions will happen, is the volume enclosed by the cathode and the shield plane. The second region is the one between the shield and induction planes, and the induction and collection planes enclose the third region. The bias voltages for the wire planes are chosen in a way that the electric field in these regions satisfies the "charge transparency" condition: 100% of the drifting electrons are transmitted through the shield plane and the induction plane reaching the collection plane to be collected. The default voltages for the wire planes used for each run are shown in table 5.1.

5.4.2   Wire Planes

The ionization electrons will reach the wire planes after being drift by the electric field in the TPC. LArIAT has three wire planes: shield, induction, and collection.

The wires are first winded in a winding machine with the right pitch and tension. From the winding machine frame, they are transferred to the G10 wire-carrier boards that are temporarily attached to an aluminum frame to avoid deformations. The winding frames are
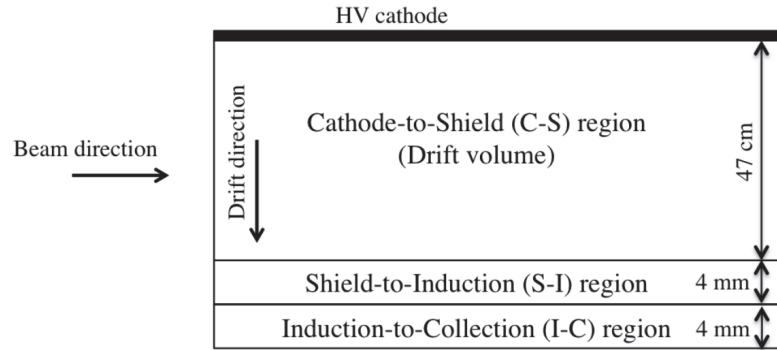
Figure 5.7: Diagram not to scale of the three drift volumes in LArIAT's TPC: the main drift region between the HV cathode and the wire planes, the region between the shield plane and the induction plane, and the region between the induction and collection planes.

Table 5.1: Bias voltages and number of wires for the wire planes used during LArIAT's runs.

Run	Pitch	Cathode	Shield	Induction	Collection	Wires/plane
Run I	4	-23164 V	-298 V	-18.5 V	338 V	240
Run II	4	-23164 V	-298 V	-18.5 V	338 V	240
Run IIIA	5	-23164 V	-325 V	0	423 V	192
Run IIIB	3	-23164 V	-298 V	-18.5 V	338 V	240
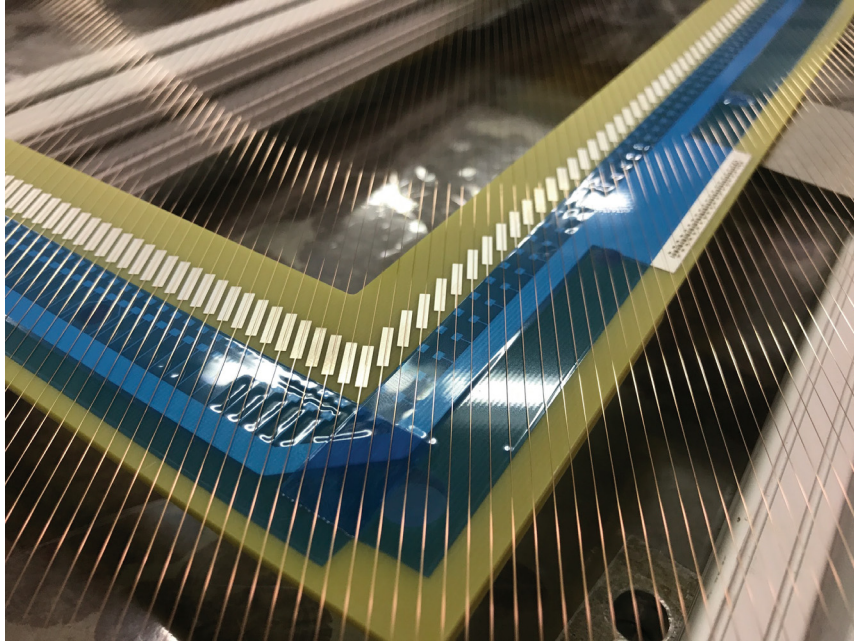
Figure 5.8: Wire plane during the mounting process.

placed on top of the wire-carrier and aligned. Once they are perfectly aligned, a temporarily epoxy will hold the alignment while a permanent epoxy is applied at the inside edge of the G10. The epoxy will cure during a day, and only after this period, the wires are cut from the winding frame. The next step is to solder the wires, resistors, and capacitors to their pads in the G10 boards. After the soldering process, the excess wires are cut, and the board is cleaned with ethanol. Figure 5.8 illustrates parts of this process. Before being installed in the TPC, all the connections and continuity of the wires are tested. Applying a 20 Hz square wave to each wire, the values of the resistors and capacitors are tested, comparing the RC time constant measured to the nominal value of 48 ns (capacitance = 2200 pF and resistance = 22 MΩ).

The first plane that the drifting electrons will reach is the shield plane. This first plane is composed of parallel vertical wires. All the wires spacing for the three LArIAT runs are shown in table 5.1. The shield plane is not connected to the readout electronics, and its function is to shield the outer planes from extremely long induction signals due to the ionization in the whole drift volume. The shield plane acts almost like a Faraday cage making the resulting shape of the signals in the induction plane easier to reconstruct. After the shield plane, there are the induction and collection planes. These planes have their wires oriented at 60° from the vertical with opposite signs. Due to this orientation, their lengths are different. As the electrons pass by the induction plane, a bipolar signal will be induced
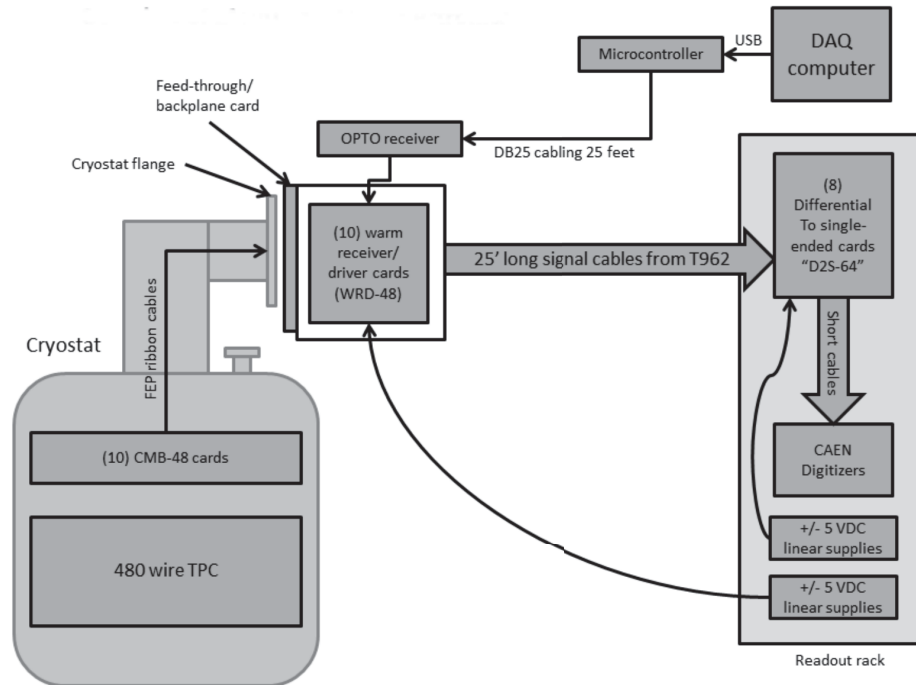
Figure 5.9: Block diagram representing LArIAT's electronics.

on its wires. The electrons will then be collected by the last wire plane (the collection plane), forming a unipolar signal on its wires.

The 480 (or 384 for Run IIIA) instrumented wires are readout individually. Each signal is first amplified by a series of cold amplifier motherboards that host ASICs designed to operate submerged in liquid argon. Utilizing cold electronics enhances the signal-to-noise ratio if compared to the warm ASICs that were being used in the ArgoNeuT experiment. The signal goes from the cold motherboards to warm receiver cards (WRDs) mounted outside and above the cryostat through ribbon cables that exit from the cryostat's chimney. The signal is then transferred away from the cryostat to the electronic racks where a set of D2S-64 cards processes them. These cards reconvert into a single-ended signal to cancel common-mode noise and provide enough current for the digitizers. The digitizers used for LArIAT were a series CAEN V1740 boards, with 128 ns sampling time, and a total of 3072 samples per event, for a total readout time per wire of 393 μs. A 90 mV signal from the ASICs corresponds to a peak amplitude inside the digitizers of 180 ADCs. The digitized signal from the V1740s is what is saved and used for reconstruction. A diagram drawn showed in figure 5.9 represents the whole front end electronics of LArIAT.

The TPC had different wire configurations during its runs to study the response and

b)
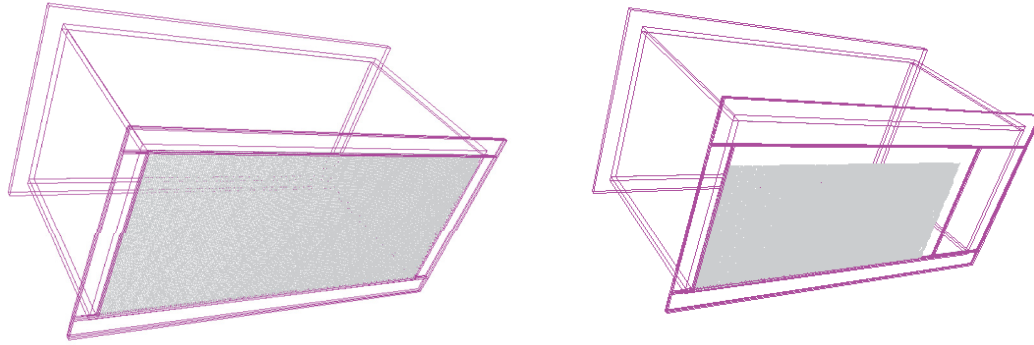
a) TPC shape for Run I, Run II and Run
IIIA.

TPC shape Run IIIB.

Figure 5.10: The TPC views for the different runs on LArIAT. Beam comes from the left side. The gray areas represent the wire planes. The active volume in figure (b) is smaller due to limited number of readout channels.

efficiency of different geometries used in various neutrino experiments. As shown in 5.1, Run I and Run II had 240 wires per plane with 4 mm wire pitch. Run IIIA had a 5 mm wire pitch and 192 wires per plane. For Run IIIB, the TPC had planes with 3 mm wire pitch and 240 wires per plane. In the last case, due to the limit number of readout channels, the active volume was reduced. Figure 5.10 shows the different TPC shapes during the whole run period.

5.4.3   Light Collection System

To ensure that the maximum information is being read, besides collecting the ionization charge, the scintillation light is also collected in LArIAT. Liquid argon scintillates in the vacuum-ultraviolet (VUV) range, which is invisible by most photosensors. For this reason, the 128 nm scintillation light needs to be shifted by a wavelength-shifter. In LArIAT, this process is done by a thin layer of tetraphenyl butadiene (TPB), which coats highly reflective dielectric substrate foils lining the TPC's four field cage walls.

LArIAT had various photon detection systems during its runs. They were all mounted behind the wire planes and held in place by a PEEK support structure that is attached to a side access flange, as shown in figure 5.11. All the windows of the devices are held parallel to the collection plane being approximately 5 cm distant. For most of LArIAT's runtime,
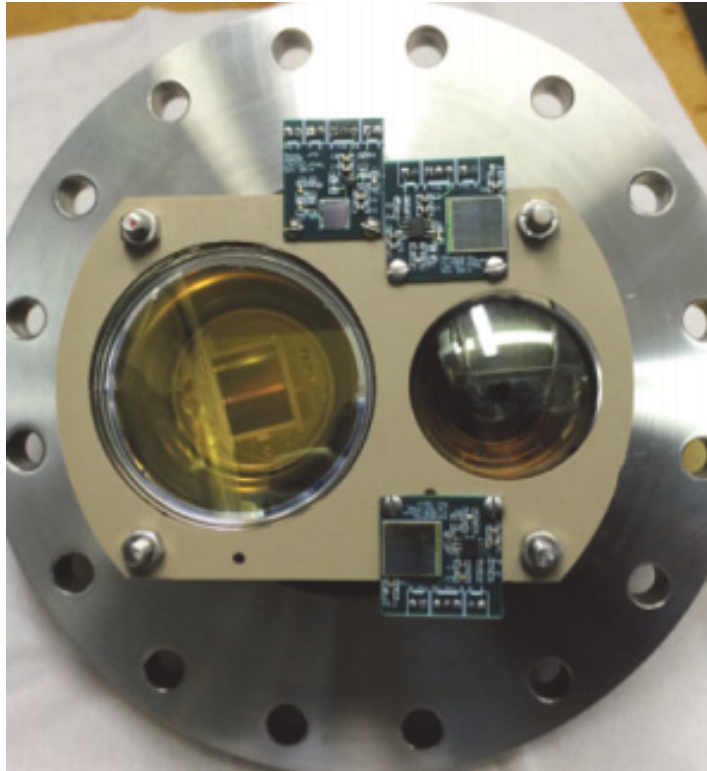
Figure 5.11: LArIAT's ligth collection system.

the light detection system was composed of two PMTs: 3-inch Hamamatsu R11065 and a 2-inch ETL D757KFL. During all the runs, several silicon photomultipliers (SiPMs) arrays were also used. Table 5.2 shows all the devices deployed for each run.

As shown in table 5.2, a new device called ARAPUCA (**?**), was deployed for Runs IIIA and IIIB. ARAPUCA is a Brazilian word for trap, and it consists of a box with high reflective inner surfaces (reflectivity > 98%), and a dichroic filter window to trap light inside until a SiPM reads it. The dichroic-filter is highly transparent to wavelengths below a particular cutoff and highly reflective above. The scintillation light coming from an interaction will first find a wavelength-shifter that will convert the VUV photons to a wavelength just below the filter's cutoff, allowing light to enter the box. The light will then encounter the dichroic-filter, passing through it. Right after, there is another wavelength-shifter coating the inner side of the dichroic-filter that will convert photons to a wavelength greater than the cutoff. Now the light cannot escape the box, and it will reflect until it finds the SiPM in one corner of the ARAPUCA.

The ARAPUCA tested in LArIAT is shown in figure 5.12, and it is 4.5 x 5.5 cm^2 with an exposed filter area of 3.5 x 4.5 cm^2. The outer wavelength-shifter used is a P-terphenyl, which emits 350 nm photons, and the inner is TPB, which emits 430 nm photons. The

Table 5.2: Devices deployed for the light detection system at LArIAT.

Run I:	PMT: Hmm R-11065 (3")	PMT: ETL D757KFL (2")	SiPM: SensL MicroFB-60035 w/ preamp	SiPM: Hmm. S11828-3344M 4x4 array
RunII:	PMT: Hmm R-11065 (3")	PMT: ETL D757KFL (2")	SiPM: SensL MicroFB-60035 w/ preamp	SiPM: Hmm. VUV-sensitive
RunIIIA:	PMT: Hmm R-11065 (3")	PMT: ETL D757KFL (2")	ARAPUCA	–
RunIIIB:	PMT: Hmm R-11065 (3")	PMT: ETL D757KFL (2")	ARAPUCA	–

dichroic-filter has a cutoff of 400 nm. Inside the box, there is a single SensL MicroFC 60035 SiPM biased at +24V. Its signals are amplified and then sent out to the DAQ.

Signals from all photodetectors are routed from the side flange of the cryostat to NIM fanouts, which give the 50Ω termination required to reduce reflections along the cables. Discriminated copies of the PMT signals are used in the construction of several light-based triggers, and the raw waveforms are recorded at 1 GHz by a CAEN V1751 digitizer.
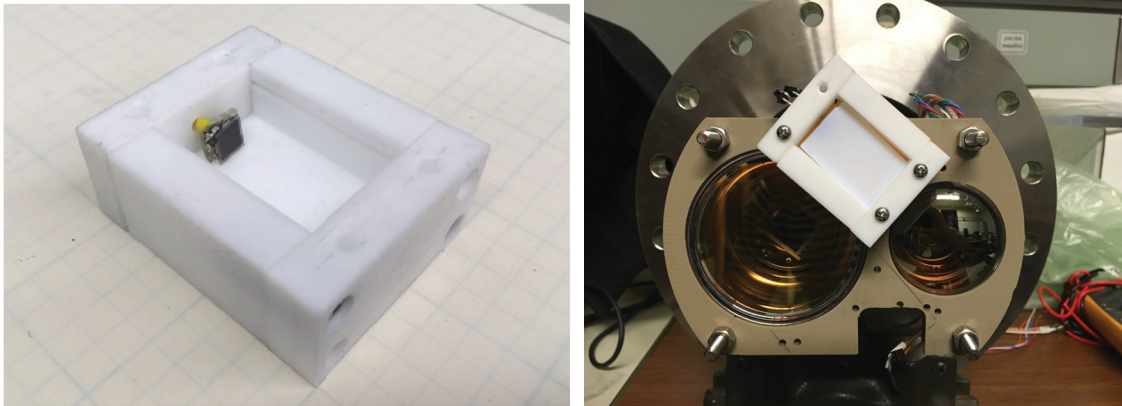
Figure 5.12: Photon detection system for Run IIIA and Run IIIB. Left: ARAPUCA prototype used in LArIAT's light collection system. Right: ARAPUCA mouted next to the PMTs.

5.4.4 Triggers and Data Aquisition (DAQ)

The main piece of LArIAT's trigger and DAQ systems are the CAEN V1495 (52) and its user-programmable FPGA. Following a trigger menu, this module checks for matches between sixteen or third two (Run III) logical inputs to flag an event with a pre-defined trigger. If a trigger pattern continues for two sequential clock ticks, the V1495 produces a readout request.

LArIAT operates in a 60.5 s cycle. The experiment receives three logic signals related to the beam timing from Fermilab's accelerator complex. These inputs will be used as input triggers: a 1-second pulse right before the beam, a 4.2 seconds pulse indicating beam-on, and a 25 seconds pulse meaning beam-off, which is used for cosmic data collection.

The beamline instruments, the cosmic paddles, and the light collection system will also provide NIM-standard logic pulse inputs to the trigger decision. Figure 5.13 shows the main trigger conditions for LArIAT.
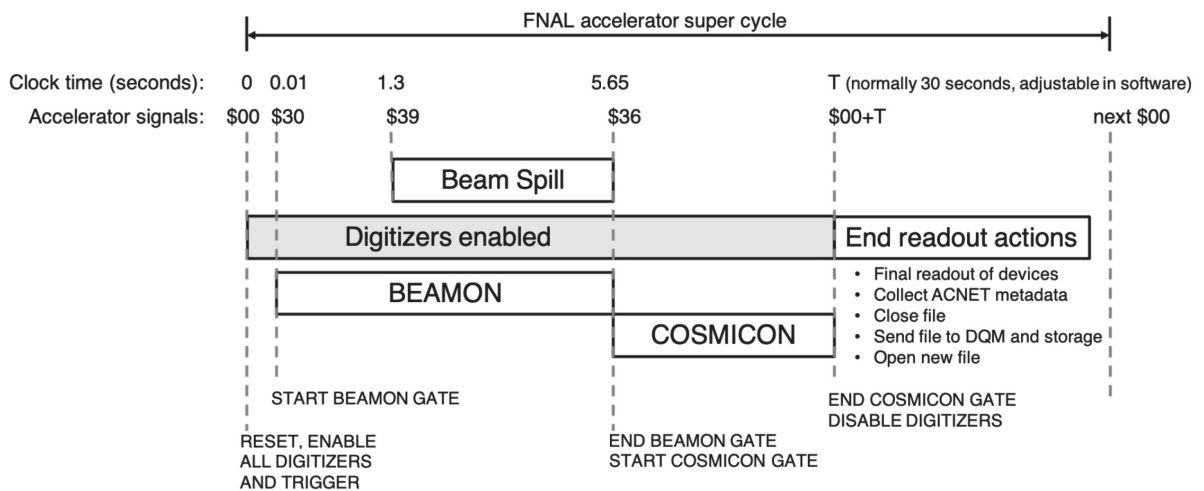
Figure 5.13: LArIAT's supercycle. Main triggers: BEAMON to receive the 4.2 s of beam and COSMICON to receive 26 s of cosmic data.

CHAPTER 6

ARGON PURITY IN LARIAT

As described in previous chapters, the energy deposition in liquid argon by a charged parti-cle can happen through ionization or excitation, producing free electrons or photons. Elec-tronegative contaminants in liquid argon, such as O_2, H_2O, and N_2, are especially damaging as they quench the free electrons and the photons generated by the interacting particles be-fore their collection in the LArTPC. Those impurities are commonly found in trace amounts in commercially-available LAr (**?**).

6.1   Argon Production

Argon, with its 0.9% content in the air, is the only noble gas, which has today a broad industrial utilization since it can be easily produced in enormous amounts and with a notably low cost. Its primary production is part of the liquefaction of dry air, and argon (which boils at 87.3K) can be easily separated by fractional distillation, for instance, from Nitrogen (which boils at 77.3K) and Oxygen (which boils at 90.2K) (53).

6.2   Impurities harmful for Light

The main focus of this thesis is the study of harmful impurities to charge and its impact on the separation of electromagnetic showers. Still, impurities critical for light will be described briefly in this section.

Non-radiative destruction of photon-producing Ar excimers, Ar_2^*, can occur through two-body collisions with all kinds of residual impurities. The impurity contributing most promi-

nently to this process is N_2 ($Ar_2^* + N_2 \rightarrow 2Ar + N_2$). Quenching competes with radiative decay, reducing the effective scintillation lifetime as shown in equation 6.1.

$$\tau_i' = (\frac{1}{\tau_q} + \frac{1}{\tau_i})^{-1} \tag{6.1}$$

where τ_q is the quenching timescale, and i denotes either the triplet or singlet excimer state.

This quenching naturally reduces the yield of photon-producing excimers by a factor τ_i'/τ_i for both the singlet and triplet populations (54**?**). In typical experimental conditions where LAr has undergone proper filtering, $\tau_q \gg \tau_s$ and very minimal change is seen in the prompt singlet component ($\tau_s' \approx \tau_s = 6ns$). However, the triplet component tends to be more vulnerable to this quenching due to its much longer decay time of $\tau_s = 1.3\mu s$.

Correcting for light quenching in data thus relies on the knowledge of τ_q, which can be estimated based on exponential fits to average optical waveforms, as shown in figure 6.1. It is possible to see that different levels of N_2 contamination in LAr (5), will affect late-light lifetime dramatically decreasing it as contamination levels increase from 0 ppm to 40 ppm.
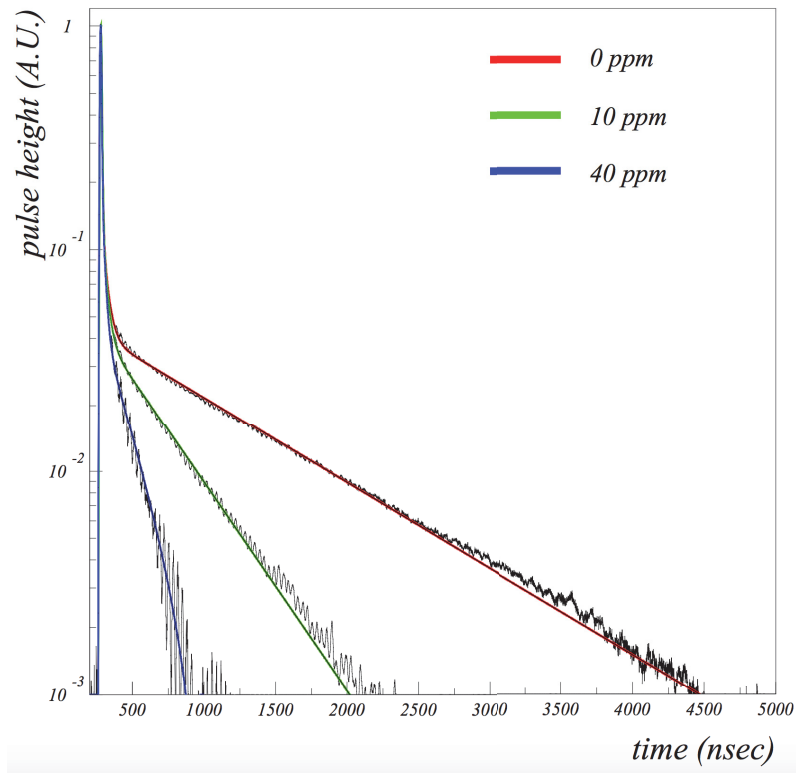
Figure 6.1: Signal shape at 0 ppm, 12 ppm and 40 ppm of N2 contamination, superimposed fits with three components (5).

6.3   Impurities harmful for Charge

Free electrons generated by the passage of a charged particle through the detector will be drifted towards the readout planes. If there are electronegative contaminates in the liquid argon, not all the electrons will reach the wire planes. The total charge produced Q_0 will then be quenched in its way from the point of production to the wire planes by impurities S. A certain portion of the molecules of contaminants will be converted to negative ions of much small mobility and, therefore, lost for the electronic pulse. The following reaction can describe the electron attachment to an impurity S (55).

$$e^- + S \rightarrow_{k_S} S^- \tag{6.2}$$

where k_S is a rate constant given by

$$k_S = \int v\sigma(v)f(v)dv \tag{6.3}$$

where v is the electron constant velocity ($v = d/t_{drift}$), $f(v)$ is the velocity distribution of the electrons and $\sigma(v)$ is the cross-section as a function of velocity for interaction of the electrons with impurities S. The rate constant k_S can also be expressed as a function of energy

$$k_S = \int \sigma(E)f(E)dE \tag{6.4}$$

where $f(E)$ is the well-known Maxwell distribution function.

Assuming that the passage of an ionizing particle produces a number N of electrons smaller than the impurity concentration N_S, the number of electrons lost per time interval is given by

$$\frac{dN}{dt} = -k_S N_S N \tag{6.5}$$

For hermetically sealed containers which have been well cleaned before filling with liquid N_S persists constant and integration of equation 6.5 gives

$$N = N_0 e^{-t/\tau} \tag{6.6}$$

or in terms of electric charge per unit length

$$\frac{dQ}{dx} = \frac{dQ_0}{dx} e^{-t/\tau} \tag{6.7}$$

where τ is the electron lifetime and is related to the rate constant and the impurity concentration by:

$$\tau = \frac{1}{k_S N_S} \tag{6.8}$$

Assuming that all the impurity is Oxygen, for an electric field up to $\approx$ 1 kV/cm, the equation above can be written as

$$\tau_e[\mu s] \approx \frac{300}{\rho_{0_2}[ppb]} \tag{6.9}$$

where, ρ_{0_2} is the amount of impurities of Oxygen with respect to the amount of argon (55).

6.3.1   Measuring Liquid Argon Purity

To allow the good functionality of LArIAT is required that the presence of electronegative contaminants is less than 1 ppb. There are two possible ways to monitor the argon purity in an experiment:

- With gas analyzers to measure the concentration of impurities

- Using cosmic muons that cross the TPC

Gas analyzers could monitor the presence of O_2, H_2O and N_2 contents throughout the cryo-system with sensitivity down to few ppb (for O_2, H_2O) and fractions of ppm (for N_2). Therefore, to precisely measure the electronegative contaminant concentration in LAr is necessary to rely on the TPC itself.

The amount of charge per unit of length dQ/dx collected at the wire plane will be dependent on the traveled distance, measured in terms of drift time. As a consequence, for a given charge deposition in argon, the amount of charge collected at the readout plane as function of the drift time manifests an exponential decay trend, with a characteristic time constant called electron lifetime τ.

Determination of τ using cosmic muons is a possible method to monitor liquid argon detectors daily. The electron lifetime is a value that can be used by the whole collaboration to correct the detector calorimetric response.

The Multi-track Method

This study will be performed with selected muons crossing the whole, or most, of the time projection chamber drift distance to measure the electron lifetime. Cosmic muons are min-

imum ionizing particles (mip); consequently, the amount of charge deposited per unit of path length follows a well-defined distribution, independent of the particle's momentum. If the portion of free electrons generated by the passage of a muon is close to the wire planes, this charge will be collected with little or no quenching due to impurities. Also, the charge generated by the portion of the track closest to the cathode will be maximally quenched. Measuring the dQ/dx along the track in different drift times will manifest an exponential decrease, whose characteristic time constant is just the electron lifetime τ that can be extracted by a simple fitting procedure.

It is significant to mention that the charge read by the wire planes will follow a convolution of a Landau and Gaussian distributions. The deposition of charge will be described by a Landau due to fluctuations in energy loss (8). The most probable energy loss will be characterized by equation 6.10.

$$\Delta_p = \epsilon[ln\frac{2mc^2\beta^2\gamma^2}{I} + ln\frac{\epsilon}{I} + j - \beta^2 - \delta(\beta\gamma)] \tag{6.10}$$

where $\epsilon = (K/2) < Z/A > (x/\beta^2)$ MeV, $K = 0.307075\frac{MeV cm^2}{g}$, Z is the atomic number of the absorber, A the atomic mass of the absorber, for a detector with a thickness x in g/cm^2, and $j = 0.200$ (56).

The Gaussian part of the convolution will describe the charge reaching the wire planes. The sigma of this distribution will depend on both the electronics - providing a constant contribution - and the diffusion process - with a contribution proportional to the square root of the drift time ($\sigma = p_0 + p_1\sqrt{t}$).

For a given drift time window, a convolution of a Landau with a Gaussian $L \otimes G$ function will represent the distribution of dQ/dx collected at the wire planes, where the sigma of the Gaussian has a square root dependence on the drift time.

For the electron lifetime calculation, it is necessary to select only cosmic muons that cross the whole TPC with the tracks going almost in a diagonal direction, as shown in figure 6.2.

The selection is performed by the cosmic ray paddles outside the TPC. As described in section 5.2.3 in chapter 5, LArIAT has two sets of cosmic ray paddles (or cosmic towers) sitting upstream and downstream of the cryostat, one beam-right, and the other beam-left. Each tower has two sets of detectors, an upper and a lower. To be triggered as a cosmic muon, is required that the particle crosses any two opposite sets of paddles: either the upper beam-left (downstream) with lower beam-right (upstream) or upper beam-right (upstream)
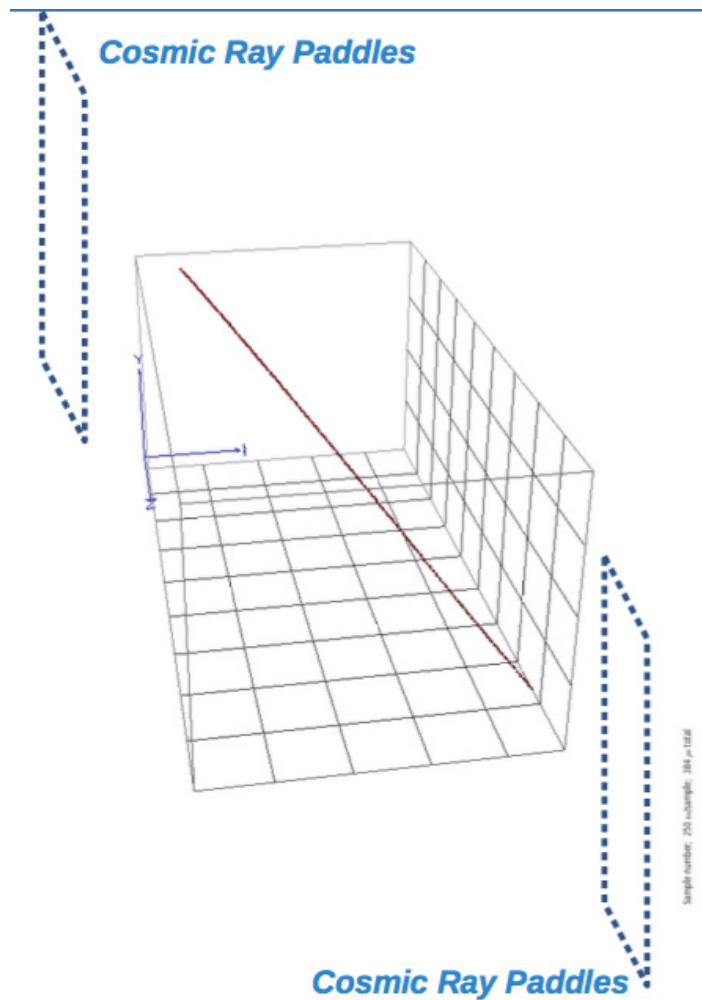
Figure 6.2: Tracks that are selected for the lifetime determination have to cross the whole TPC in a diagonal direction. The events are selected by the cosmic ray paddles outside the TPC.

with lower beam-left (downstream). The coincidence between the signals will select muons that crossed the body diagonal of the active volume, spanning the full range of drift lengths that are possible in the detector. After being selected as a crossing muon by the cosmic ray paddles, the event will be verified by a series of cuts applied to the tracks and hits:

Single track The event must include only one reconstructed track with more than five hits. This assures that the charge collected belongs to a single mip in the detector.

Boundary conditions Even after the cosmic ray paddles trigger this event, to verify that the muon crosses the whole TPC, the code requires that the reconstructed track must start and end within 2cm of any two sides of the TPC.

Vertical track angle The angle θ of the reconstructed track in the YZ plane must be $20° <$
$\theta < 80°$ or $100° < \theta < 160°$. This eliminates tracks that are verticle or horizontal
aligned.

Horizontal track angle The angle ϕ of the reconstructed track in the ZX plane must be
$20° < \theta < 80°$ or $100° < \theta < 160°$. This eliminates tracks that are aligned or perpen-
dicular to the beam(if the track is parallel to the wire planes, it will be impossible to
describe the charge dependence with the drift time).

Track length The track must be at least 10cm long.

Track straightness To test if a track is straight, two requirements need to match. First,
the scalar product of the direction vectors at the beginning and end of the track must
be > 0.99. Besides, the linear fit of hit wire number versus hit drift time plot for both
collection and induction views must have a normalized $\chi^2 < 10$ (that is, the track must
be straight on both collection and induction views). Track straightness is essential as
the inclination of the track, used to weight the charge of each hit, is computed only
once for the track as a whole.

Hit plane Only the hits of the collection plane will be analyzed.

Delta ray cut Hits identified as pertaining to delta rays are rejected. First, all the hits with
$dQ/dx > 1400ADC.ns$ (the dQ/dx MPV of a hit from a mip is $\sim 900ADC.ns$ as seen
from data) are flagged as potential deltas. If three consecutive hits are flagged as
possible deltas, they are excluded.

Boundary hits The first and last hits of the track are discarded as they may hold incom-
plete charge.

Single hit in the wire The hit in the track must be the only one detected by the wire.

These cuts described above are to guarantee that the muons cross the TPC in a way
that allows part of the track to be near the wire planes and another part close to the cathode.
Consequently, it is possible to establish the charge lost in function of the drift time. The cuts
will also assure that only cosmic muons will be considered for the calculation of the electron
lifetime, eliminating possible deltas and particles from the beam.

For the calculation of the electron lifetime using the selected muons, the technique will
combine all the crossing muon tracks of a given data sample; in LArIAT, the data sample
was chosen to be all the data from one day.
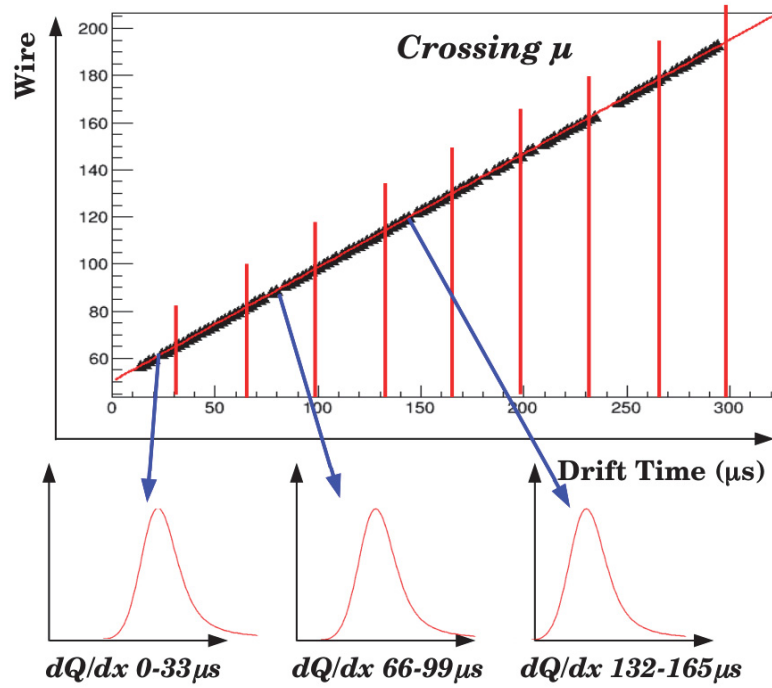
Figure 6.3: A track from a crossing muon divided by the drift time into bins of $33\mu s$ each. The charge of all hits of each section of the track will then fill dQ/dx histograms corresponding to the drift time value of the hit.

In this approach, the TPC drift time is divided into 12 bins of $33\mu s$ each, and for each track, calculate the charge per unit length (dQ/dx) that falls into each bin. The dQ/dx deposited per bin will then fill a histogram, and after all the tracks of the data sample being analyzed, there will be 12 histograms per day. Figure 6.3 shows this method.

The extension of each bin has been determined to be small enough to have negligible differences in the charge loss due to quenching inside the bin, but still long enough to allow for histograms with plausible statistics. For an electron lifetime $\tau = 800\mu s$, the variation in dQ/dx of two hits at the limits os their drift time bin is $\sim 4\%$, which decreases to $\sim 2\%$ if $\tau = 1500\mu s$.

Every histogram created has to have at least 500 entries so that it will be fitted by a $L \otimes G \oplus G$ function. The first part of this function was described in the previous section, and the second part includes an extra Gaussian added to take into account a background contribution given by delta rays not removed by the cuts. Figure 6.4 shows a typical fitted dQ/dx distribution for an arbitrary drift time bin.

From the fits of the dQ/dx distributions, it is possible to obtain the fitting parameters, including the Most Probable Value (MPV) for each histogram. These values are plot as
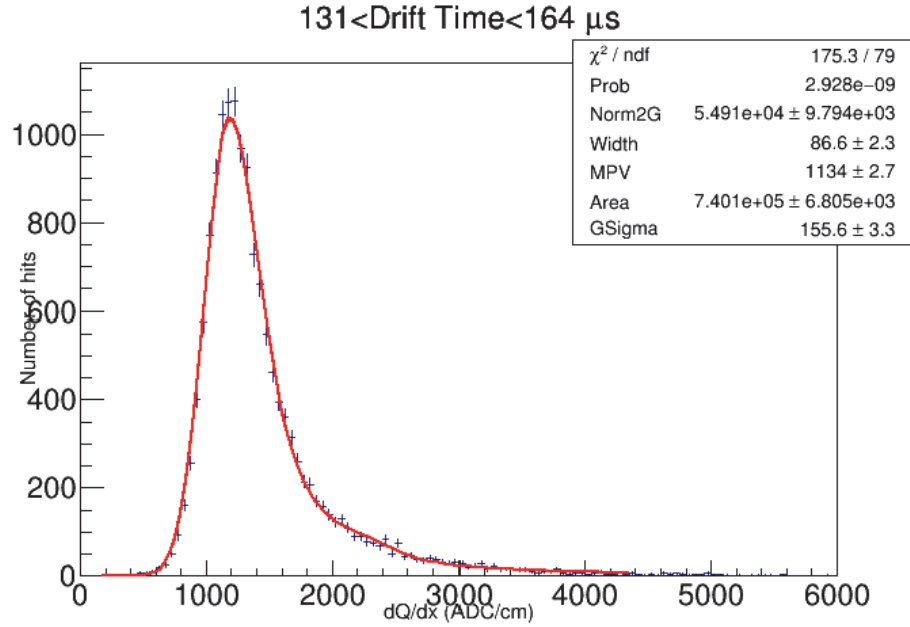
Figure 6.4: dQ/dx distribution for runs 8938 to 8973 in the 197 - 229 μs bin (check this). The blue line represents the extra Gaussian part of the fit.

a function of the drift time value associated with the respective histogram. The drift time associated with each histogram corresponds to the center bin value, with the bin half-width taken as the error. This plot is fitted with an exponential from which is possible to extract the electron lifetime τ. Figure 6.5 shows one of these fits.

The results of the electron lifetime measurements over the three data-taking periods of LArIAT are shown in figure 6.6. The oscillations in electron lifetime can be traced to several factors. Since LArIAT does not have a recirculating system, the cryostat has to be filled ever 6 hours, which means that new argon will enter the TPC multiple times a day. The purity of the argon that was delivered varied from week to week, and saturation of the in-line filter resulted in dramatic decreases in electron lifetime over a very short time. After filter regeneration, the lifetime slowly increased as the less pure argon inside the cryostat was diluted by top-offs of cleaner argon from the filter.

According to equation 6.9, LArIAT experienced concentrations of O_2 up to ≈ 0.16 ppb during Runs 1 and 2, and up to ≈ 0.65 ppb for Runs 3a and 3b.
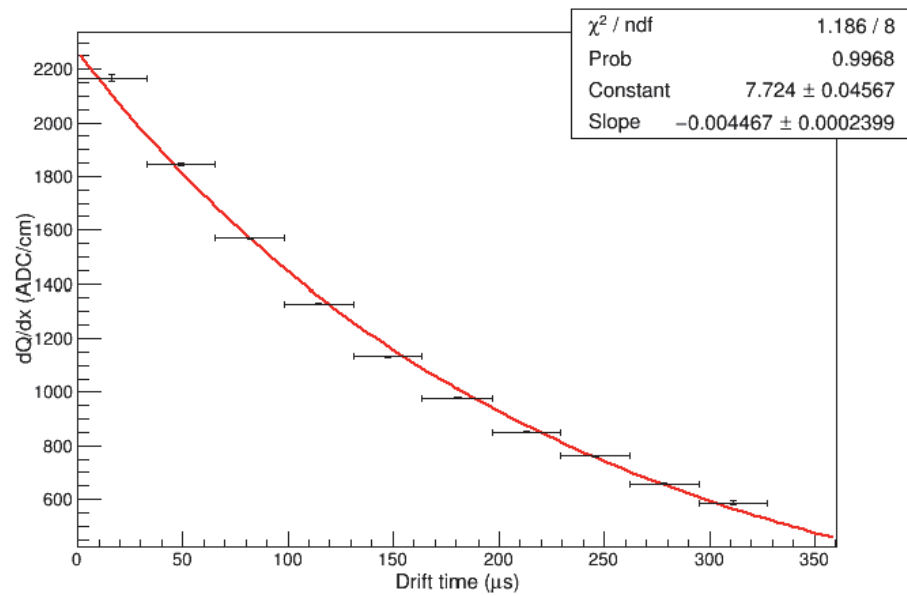
Figure 6.5: Plot of dQ/dx Most Probable Value versus drift time. The red line shows the exponential fit from which τ is determined.
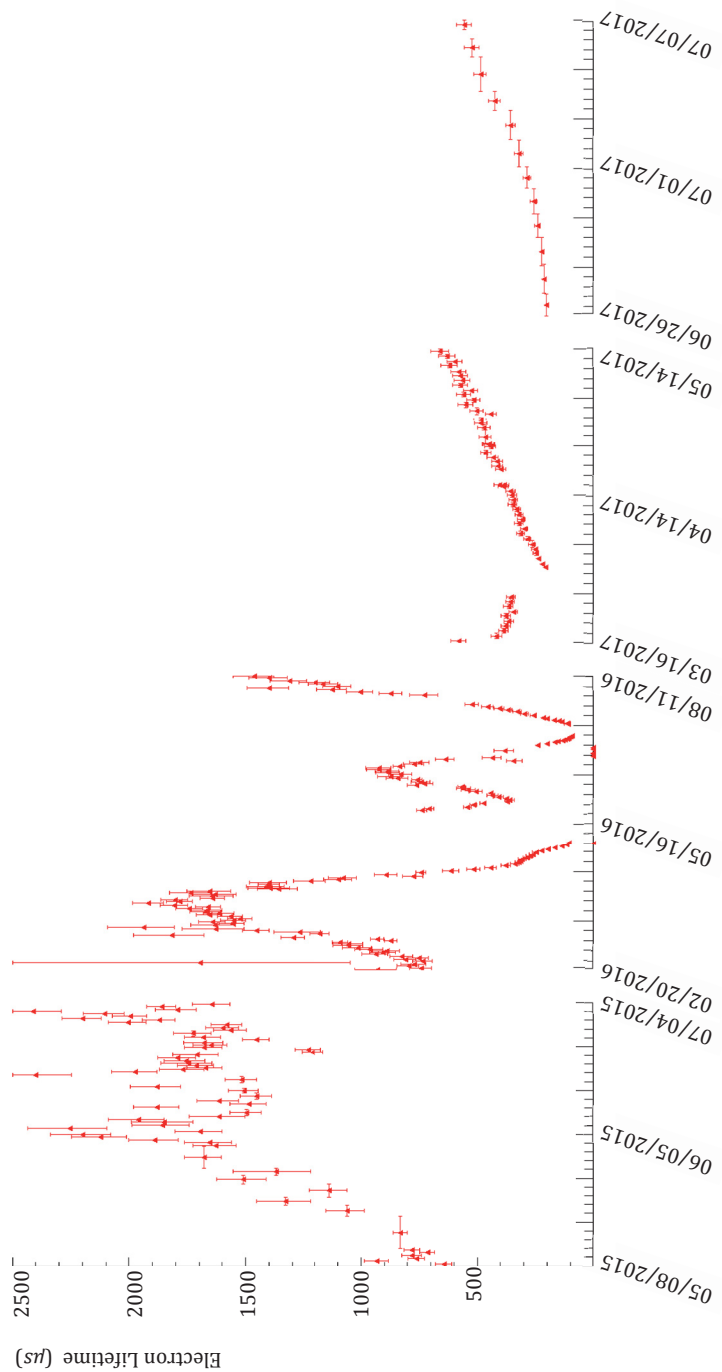
Figure 6.6: Electron Lifetime for all the three data-taking periods, from 2015 to 2017. Fluctuations are due to many factors related to the fact that LArIAT does not have a recirculation system.

CHAPTER 7

ELECTROMAGNETIC SHOWERS IN A TPC

As discussed in chapter 3, the distinction between electron or photon initiated showers is the key to explain the low energy excess seeing by LSND and MiniBooNE. Separating electromagnetic showers will also be crucial for CP violations measurements.

As electrons and photons interact with the active material of the detectors, they will initiate a cascade of more electrons and photons with lower energies called an electromagnetic shower. LArTPCs have the power to discriminate between electron and photon initiated showers due to its excellent calorimetric capacity and resolution to get a detailed visualization of the event topology.

Since LArIAT is an experiment exposed to a charged particle beam, it collects a large sample of electron showers produced by the Fermilab TestBeam Facility beam. LArIAT is also able to see photon showers coming from π_0s originated in pion charge-exchange reactions. This all makes this experiment ideal for studying electromagnetic showers.

7.1 Differences between electromagnetic showers

Visually, electrons and photons behave in the same way as they interact with a detector. They will both initiate a cascade of particles, and based on the event's topology is difficult to distinguish between each other. Luckily, there are a few characteristics that help in this separation, and LArTPCs have the capability of accessing them.
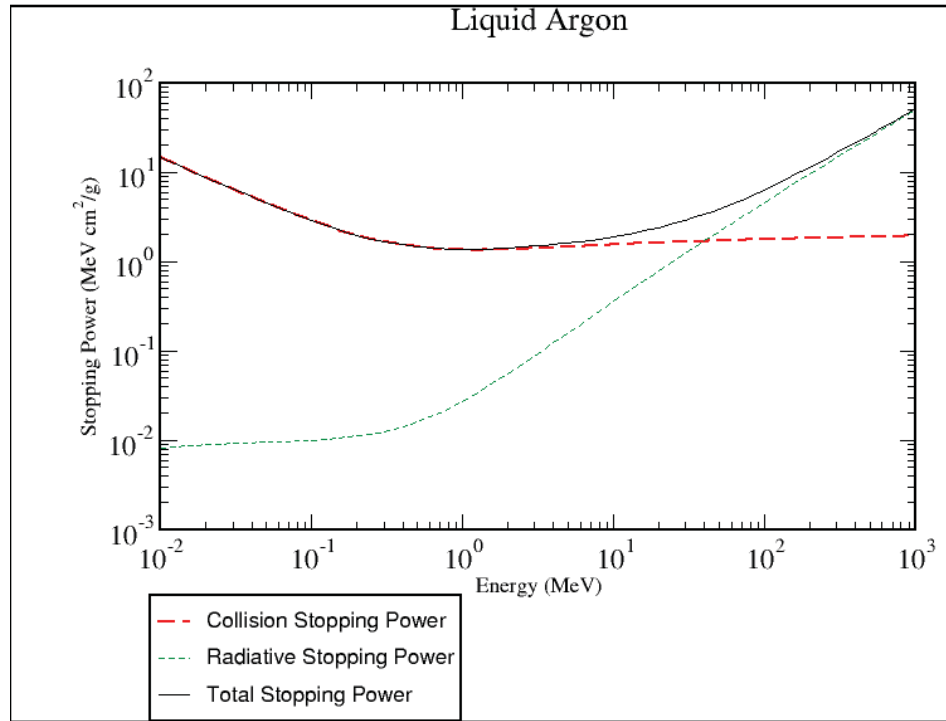
Figure 7.1: Energy loss per unit distance travelled (MeV/cm) for electrons in liquid argon. It is possible to see colision and radiative stopping powers. Plot from (6)

.

7.1.1   Energy loss by Electrons

Figure 7.1 shows the contribution of collision and radiative stopping powers for liquid argon. For the energy range of electrons from LArIAT's beam, bremsstrahlung is the dominate process for electron's energy loss.

From figure 7.1 is possible to notice that electrons will deposit energy since they have kinetic energy inside the TPC. For photons, it happens differently: they will move undisturbed until they either Compton scatter or produce a e^+/e^- pair. The notable distances traveled by photons before depositing energy in the TPC makes their signature qualitatively distinct from that of electrons. The characteristic amount of matter crossed for these interactions is named the radiation length X_0, usually measured in g/cm^2. It has two meanings: the mean distance that a high energy electron has to cross to lose all but $1/e$ of its energy by bremsstrahlung, and 7/9 of the mean free path for pair production by a high energy photon (57). It is also a good scale measure for defining high energy electromagnetic cascades. It

is possible to calculate the radiation length using:

$$\frac{1}{X_0} = 4\alpha r_e^2 \frac{N_A}{A} \{Z^2[L_{rad} - f(Z)] + ZL'_{rad}\} \tag{7.1}$$

where A = 1 g/mol, $4\alpha r_e^2 N_A/A = (716.408 g/cm^2)^{-1}$. $L_{rad} = ln(184.15Z^{-1/3})$ and $L'_{rad} = ln(1194Z^{-2/3})$. The function $f(Z)$ for elements up to uranium is given by:

$$f(Z) = a^2[(1 + a^2)^{-1} + 0.20206 - 0.0369a^2 + 0.0083a^4 - 0.002a^6] \tag{7.2}$$

where a = αZ with α being the Fine Structure Constant. For LAr, X_0 = 14 cm.

Electrons will lose energy by bremsstrahlung at a rate approximately proportional to its energy, while the ionization loss rate modifies only logarithmically with the electron energy. The critical energy E_c is sometimes defined as the energy where the two loss rates are equal. The definition used at the PDG (8) is the one described by (58), who represents the critical energy as the energy where the ionization loss per radiation length is equal to the electron energy. For solid and liquid absorbers the critical energy can be approximated by (59)

$$E_c = \frac{610 MeV}{Z + 1.24} \tag{7.3}$$

After E_c electrons will lose its energy mainly by bremsstrahlung with cross-section given by (60):

$$d\sigma/dk = (1/k)4\alpha r_e^2 \{(\frac{4}{3} - \frac{4}{3}y + y^2)[Z^2(L_{rad} - f(Z)) + ZL'_r ad] \tag{7.4}$$
$$+ \frac{1}{9}(1 - y)(Z^2 + Z)\}$$

Where $y = k/E$ is the fraction of the electron's energy transferred to the radiated photon. At small y, the term on the second line ranges from 1.7% (low Z) to 2.5% (high Z) of the total. If this is ignored and the first line simplified with the definition of X_0 given in equation 7.1 the cross-section equation can be simplified to

$$\frac{d\sigma}{dk} = \frac{A}{X_0 N_A k}(\frac{4}{3} - \frac{4}{3}y + y^2) \tag{7.5}$$

7.1.2 Energy loss by photons

Figure 7.2 shows the most important interactions that photons can experience in liquid argon. Interactions for low energy photons are dominated by the photoelectric effect.

As their energies increases to values comparable with the ones seeing in LArIAT, pair production starts to dominate as shown in figure 7.2. There is a minimum energy required for e^+e^- production given by:

$$E_\gamma \geq 2m_ec^2 + \frac{2m_e^2c^2}{m_{nucleus}} \tag{7.6}$$

Since, $m_{nucleus} >> m_e$, the equation above can be written simply as $E_\gamma \geq 2m_ec^2$

The cross-section of the interaction can be expressed as:

$$\frac{d\sigma}{dx} = \frac{A}{X_0N_A}[1 - \frac{4}{3}x(1-x)] \tag{7.7}$$

Where x here is the fraction of energy transferred to the pair produced electron (or positron) and is given by $x = E/k$, and k is the incident photon energy. And if integrated, the pair production cross-section becomes:

$$\sigma = \frac{7}{9}(\frac{A}{X_0N_A}) \tag{7.8}$$

Figure 7.3 shows that for energies in the order of the ones seeing in LArIAT (a few hundreds of MeV) is expected that over 90% of the photons go under pair production interactions.

7.1.3 Electromagnetic Showers

As electrons travel by a medium, they can lose energy either by excitation or ionization of the atoms that form the material (collision stopping power) or through bremsstrahlung interaction (radiative stopping power). For energies well beyond the critical energy ($\approx$ 45 MeV for liquid argon), as shown in 7.1, radiative loss considerably exceeds ionization loss, producing electromagnetic showers.

Electromagnetic showers can be described as a cascade of photons and electrons that produce a dense cloud of charge deposition pointing in the direction of the original electron's momentum (**?**). This cascade can only happen if the energy of the radiative photon is sufficiently high to produce electron-positron pairs. These newly created particles can also experience other bremsstrahlung interactions, producing more photons, and so on until
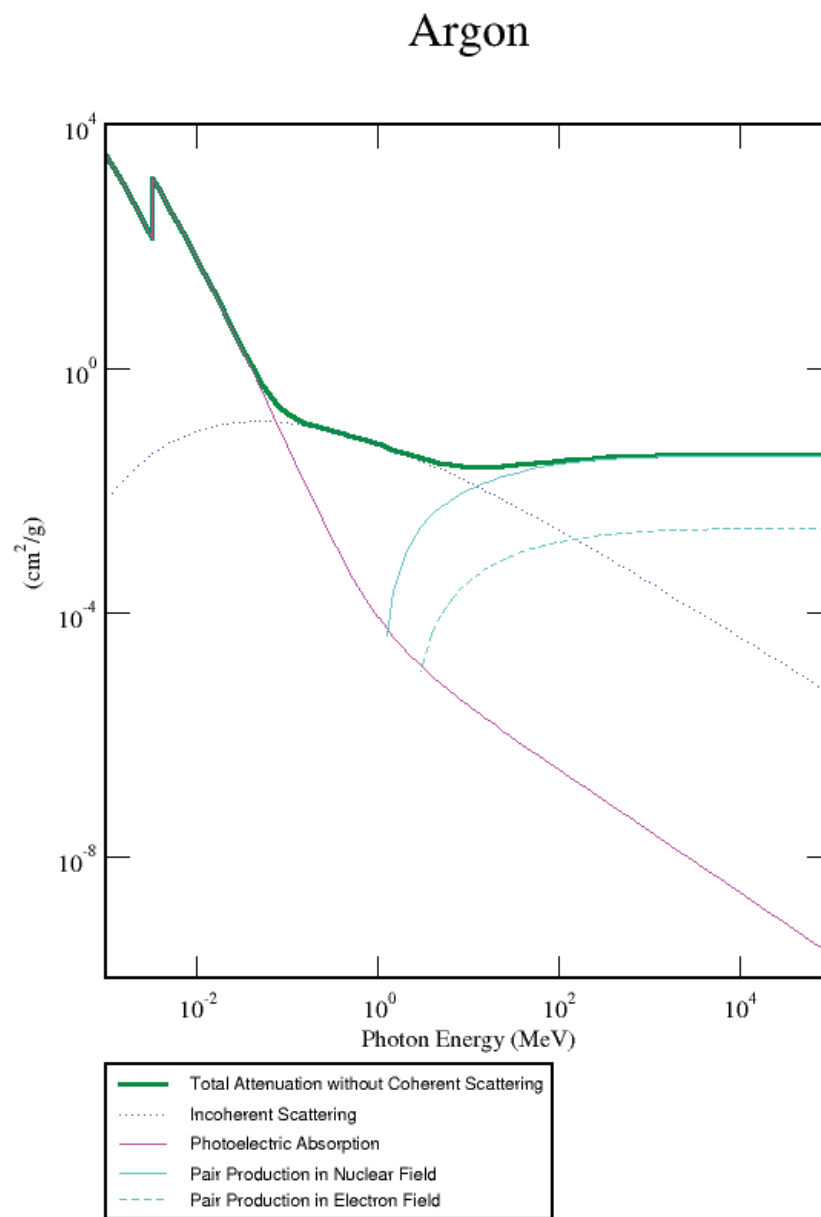
Figure 7.2: Cross-section values for photons interactions with Argon. Graphic generated with (7)
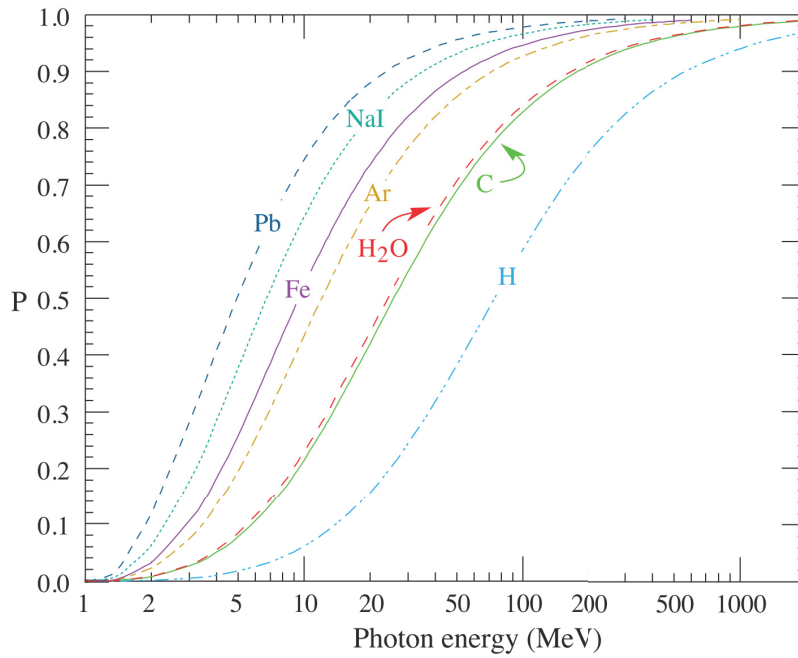
Figure 7.3: Probability of a photon interaction result in electron-positron pair for various elements and energies (8).

photons fall below the pair production threshold, and energy losses of electrons other than bremsstrahlung begin to dominate. The development of cascades caused by electrons, positrons, or photons is governed by bremsstrahlung of electrons and pair production of photons.

A simple model is able to describe the main features of particle multiplication in electromagnetic cascades: assuming that a photon of initial energy E_0 starts the cascade by producing an electron/positron pair after one radiation length. Assuming also that the energy is shared symmetrically between the particles at each multiplication point, the number of particles at a depth t is given by:

$$N(t) = 2^t \tag{7.9}$$

with energy:

$$E(t) = E_0 . 2^{-t} \tag{7.10}$$

The cascade will continue until the electron has less than the critical energy E_c:

$$E_c = E_0 . 2^{-t_{max}} \tag{7.11}$$

After this point, the particles created in the shower will be only absorbed. The position of the shower comes from:

$$t_{max} = \frac{ln E_0/E_c}{ln 2} \propto ln E_0 \qquad (7.12)$$

The transverse development of electromagnetic showers in different materials follows well with the "Molière radius" R_M, given by (61; 62):

$$R_M = X_0 E_s/E_c \qquad (7.13)$$

where $E_s \approx$ 21 MeV (8). About 10% of the energy of an electromagnetic shower, on average, falls outside of the cylinder with radius R_M. And, about 99% of it is contained inside of $3.5 R_M$.

7.1.4 Differences between Electron and Photon initiated showers

To be able to solve the questions involving the low energy excess of electron neutrinos, experiments have to be able to distinguish between the showers. As said previously, LArT-PCs use technology with high spatial resolution and high calorimetric capacity and is the perfect kind of detectors to find the answers for the open questions in the neutrino world.

Electromagnetic showers seem to be the same visually, as shown in figure 7.4, although there are a few small details that can help with the separation between them.

The first method to separate electron from photon showers considers the radiation length. In liquid argon X_0 = 14 cm, which is large compared to the excellent spatial resolution of TPCs. One of the definitions of radiation length is that it represents 7/9 of the mean free path for pair production by a photon. This means that a photon may leave a visible gap between the interaction vertex and the start of the shower. For an electron interacting with liquid argon, such gap does not exist. This topological difference can be used in neutrino experiments to identify photon and electron initiated showers. However, there are cases where high energy gammas interact in a sufficiently short distance from the vertex in such a way that the gap is not visible. Luckily there is a second method for discrimination.

The other method to separate electromagnetic showers consists of using calorimetry at the beginning of the shower. Electron showers are initiated by one ionizing particle, while photon showers are started by an $e^- e^+$ pair, meaning two ionizing particles. Looking at the dE/dx at the beginning of the shower is possible to discriminate the two particles.
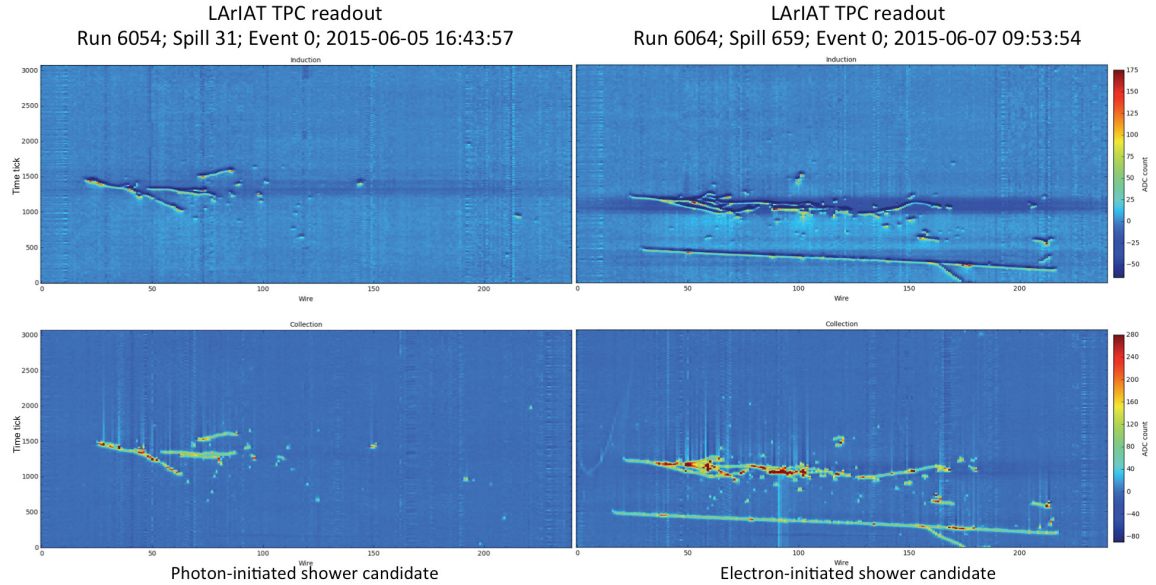
Figure 7.4: LArIAT's event display showing electron and photon initiated shower candidates.

For LArIAT, the second method is more appropriated since the experiment does not use neutrinos. Using charged particles from the beam, there is no vertex for the interaction, making the topologic method inefficient. On the other hand, LArIAT can look to the beginning of the showers and distinguish them by the calorimetric way, also testing the efficiency of separation for all the different geometries used in the experiment.

7.2   The analysis

For this thesis, sets of 20k electrons and 20k photons with momentum distributed between 250 MeV/c and 750 MeV/c were created, and each set was simulated with different electron lifetime values. The values for τ were chosen to match the ones seeing in LArIAT during its runs (figure 6.6) and are shown on table 7.1. The particles were fired from the position z = -100, which corresponds to the front of the TPC. All the simulations were done for all the three different geometries (3, 4, and 5 mm wire pitches).

Equation 6.7 represents the charge collected after being quenched by impurities. Therefore, it is possible to invert the equation and infer about the charge that was deposited,

Table 7.1: Electron lifetime values used for electrons and photons simulations for each geometry. The values were chosen to reflect the values found on data for each run.

4 mm	5 mm	3 mm
150 μs	150 μs	100 μs
300 μs	300 μs	300 μs
400 μs	400 μs	500 μs
500 μs	550 μs	700 μs
700 μs	700 μs	–
1000 μs	–	–
1200 μs	–	–
1400 μs	–	–
1500 μs	–	–
1600 μs	–	–
2500 μs	–	–

correcting the charge that was read:

$$\frac{dQ_0}{dx} = \frac{hit - charge}{track - pitch} e^{t/\tau} \tag{7.14}$$

Where, $hit - charge$ is the charge read by each wire, and $track - pitch$ is the wire pitch (3, 4, or 5 mm) projected on the direction of the track. The value dQ/dx is summed until the beginning of the shower reaches 1.0, 1.5, 2.0, and 2.5 cm. The charge deposition is evaluated for all the different beginnings of the shower for the different geometries.

From figure 7.5 shows the dQ/dx for electrons and photons with τ = 500 μs. It is possible to see that the electron deposition has only one peak centered $\approx$ in 20k ADC/cm compatible with charge coming from one ionizing particle.

The photon distribution is a little more complicated: it has two peaks - one matching two ionizing particles centered $\approx$ 42k ADC/cm, and one smaller peak matching one ionizing particle and coinciding with the electron's peak. The most prominent peak is the one corresponding to two ionizing particles, meaning that most of the interactions were from pair production form. However, a small fraction of the photons suffered Compton scattering, and the emitted electron showered inside the TPC. In a neutrino experiment, the one ionizing signal can be misinterpreted, and the original photon can be not well identified.
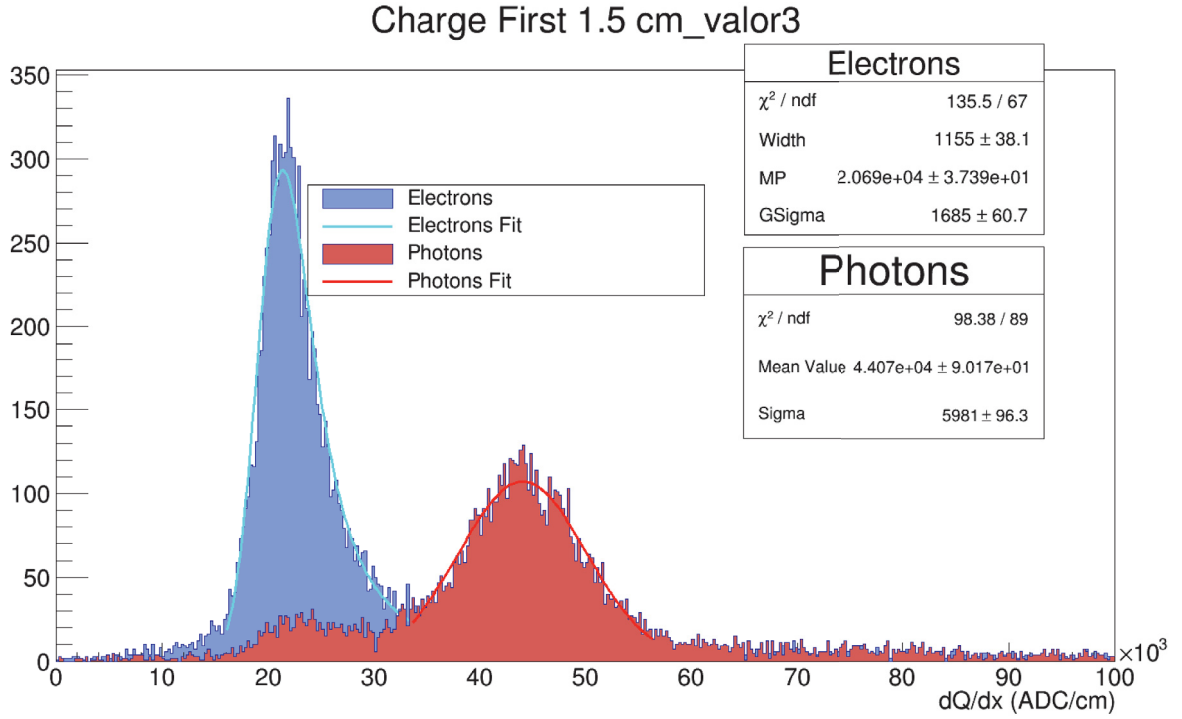
Figure 7.5: dQ/dx for simulated electrons and photons in LArIAT's detector using 4 mm wire pitch and τ = 500 μs considering 1.5 cm of the beginning of the shower.

The fittings applied to the histograms were chosen among several fits using different ranges. The left part of the fit for the electron's peak varied from 0 to the first x corresponding to 10% of the MPV high with 100 ADC/cm steps. The right side ranged from the last x corresponding to 10% of the MPV high to 70k ADC/cm (a region free from one ionizing particle peak) with 100 ADC/cm steps. The fit with the lowest χ^2/NDF provided the fit range to the histogram. For the photons histograms, the same technique was used for the second peak only.

To try to understand what is an electron and what is a photon without topology information, a few new parameters will be defined and applied to the dQ/dx distributions.

Figure of Merit

To measure the separation between two peaks, a Figure of Merit (FoM) (63) will be defined using the difference in ADC/cm between the two peaks and their width:

$$FoM = \frac{\Delta M}{\frac{1}{2}(\sigma_1 + \sigma_2)} \tag{7.15}$$

where ΔM is the difference in ADC/cm between the two Most Probable Values, and σ_i
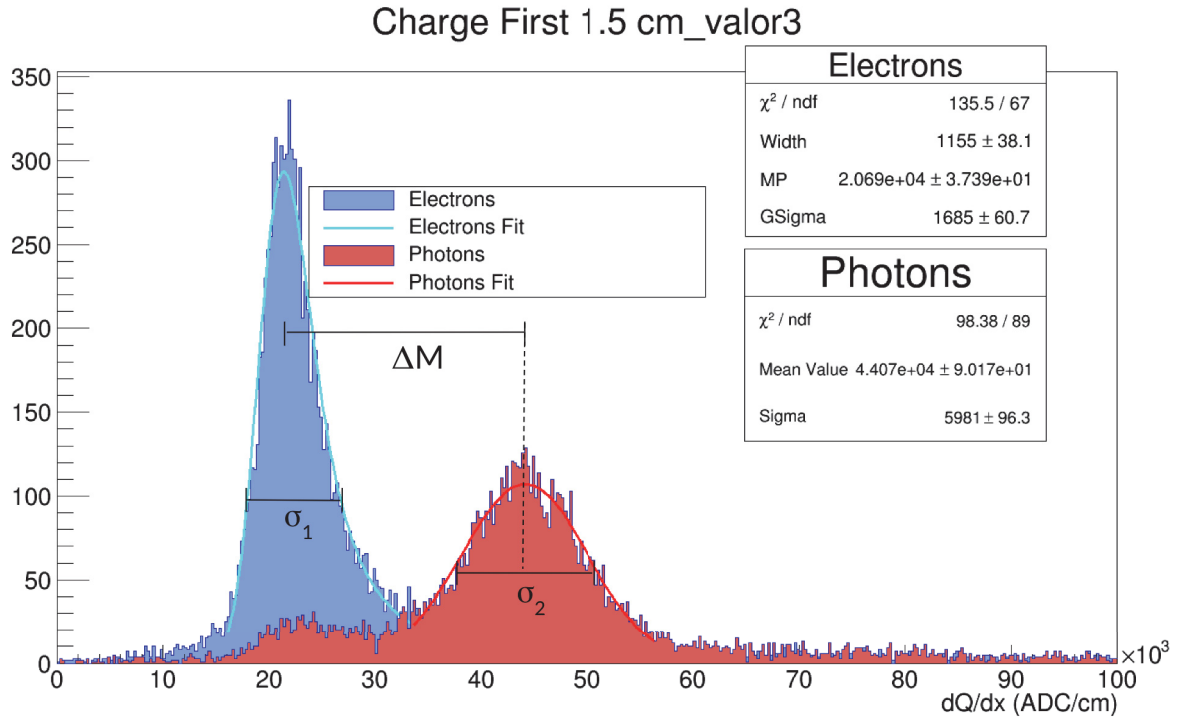
Figure 7.6: dQ/dx for simulated electrons and photons with the parameters used for the Figure of Merit calculation.

are the widths of the two distributions, as shown in figure 7.6

Figures of Merit are quantities used to characterize the performance of a device, system, or method. The calculation of FoM can be adjusted to each specific case.

Particle Purity

To learn how much from the one ionizing peak comes from electrons, it is useful to define an electron purity percentage (ep). This number will be calculated using the histogram's integrals:

$$ep = \frac{\int_0^{min} electron's histogram}{\int_0^{min} electron's histogram + \int_0^{min} photon's histogram} \tag{7.16}$$

where min is defined as the point where the two fits coincide ($f(electron's histogram) - f(photon's histogram) < 0.01$).

For completeness, it is possible to calculate also the photon's purity (pp) in the same
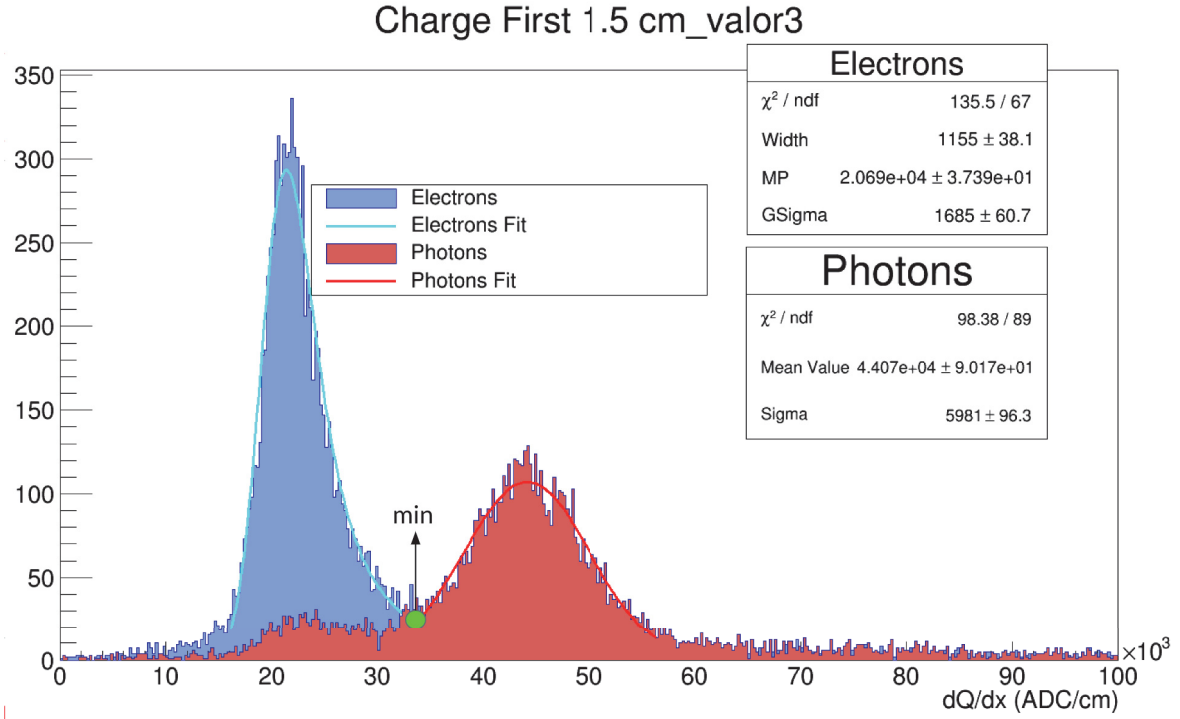
Figure 7.7: dQ/dx distributions and their fits showing the min point used for the integration.

way:

$$pp = \frac{\int_{min}^{maxbin} photon's\, histogram}{\int_{min}^{maxbin} electron's\, histogram + \int_{min}^{maxbin} photon's\, histogram} \tag{7.17}$$

where $maxbin$ is the maximum bin of the distributions.

For the best electron-photon shower separation, it is desired that the distributions have a high Figure of Merit number and the maximum electron purity percentage. So, it is possible to look at the plot in figure 7.8 to select the best samples.

Figure 7.8 shows all the values calculated for the different wire pitches and considering different values for the beginning of the shower. Each data point corresponds to a different electron lifetime used for the simulation, and it was also used for correcting the charge read. It is noticeable that the best configurations for electromagnetic shower separations are in the top right corner, indicating high Figure of Merit values and high electron's purity. From this figure, the best situations are:
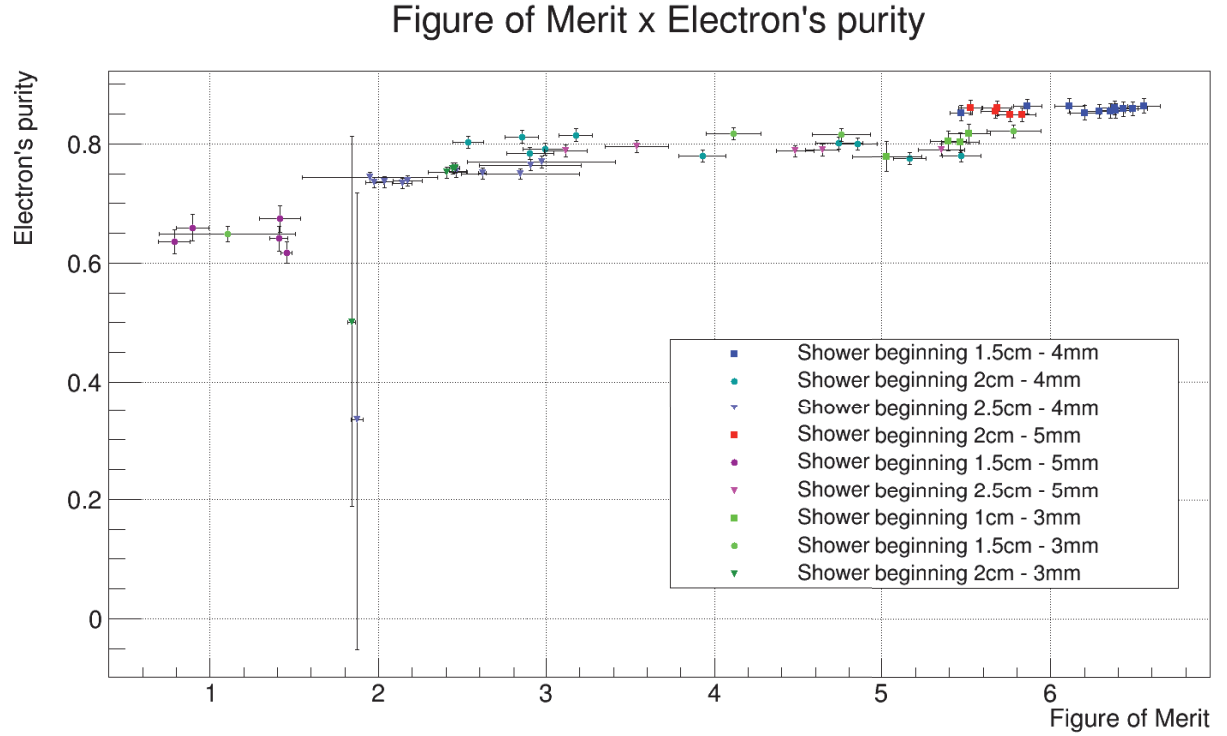
Figure 7.8: Plot of the Figure of Merit vs Electon's purity.

4 mm wire pitch: beginning of shower of 1.5 cm

5 mm wire pitch: beginning of shower of 2.0 cm

3 mm wire pitch: beginning of shower of 1.0 cm

These three areas assure at least 80% of electrons purity in the one ionizing particle region. Now that a set of data points were selected for each different wire pitch, it is possible to study the dependence with the electron lifetime. Figure 7.9 will show this dependence.

From figure 7.9, it is possible to identify a standard behavior for all the three different geometries used. For low electron lifetimes, the capability of the method on distinguishing between showers is lower than for high electron lifetimes, even after the correction of the charge collected.

The fit of the plots in figure 7.9 was done with the following equation:

$$y = p_0(1 - e^{-p_1 x}) \tag{7.18}$$

After a certain value of electron lifetime, all the configurations reached a plateau for the Figure of Merit value, meaning that we have a minimum electron lifetime for good electron-

Electron Lifetime (μs) x Figure of Merit
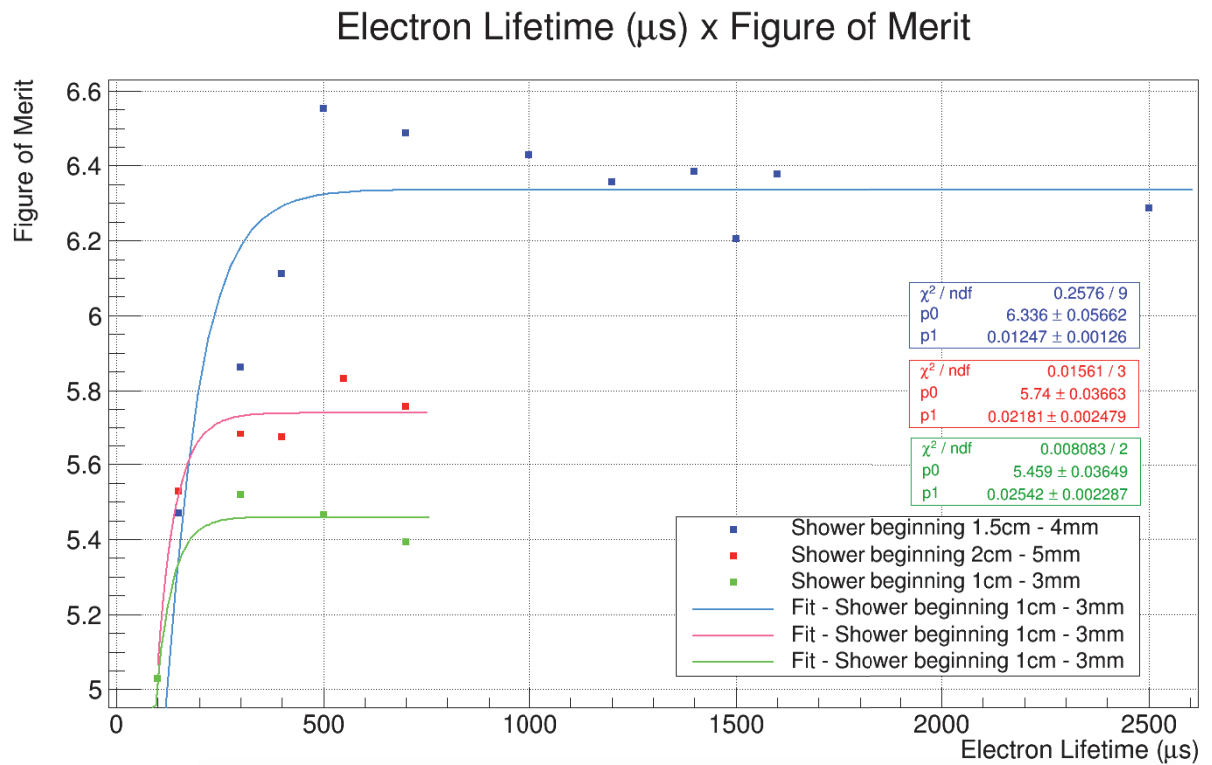
Figure 7.9: Electron Lifetime vs Figure of Merit. Best data set for shower discrimination of each of the three different configurations.

Table 7.2: Values of minimum electron lifetime for a good electron-photon shower separation on LArIAT's detector.

4 mm wire pitch	5 mm wire pitch	3 mm wire pitch
$\approx 400\ \mu s$	$\approx 250\ \mu s$	$\approx 300\ \mu s$

photon shower separation. For LArIAT's geometries, the values found for τ for a good electromagnetic shower separation with more than 80% of electron's purity where:

These values were calculated for the electron lifetime's value needed to get to 99% of the plateau, and specif for LArIAT's geometry. The idea now is to extrapolate this study for other neutrino experiments.

7.3 Impact on other neutrino experiments

Since many current and future neutrino experiments share the same technology, it is possible to apply the results of this thesis to different LArTPCs.

These other time projection chambers do have the same technology; however, they all have different characteristics. The results of this study will be extrapolated to three experiments: MicroBooNE, SBND, and DUNE.

MicroBooNE is, as mentioned in chapter 3, is a 87 tons LArTPC already taking data since 2015 at Fermilab. Its TPC has three readout planes (two inductions and one collection) with 3 mm wire spacing and operates at a 273V/cm electric field. The chamber has a maximum drift distance of 2.5 m, and it is currently the largest LArTPC running in the world. More information about MicroBooNE is available in (64).

SBND was also mentioned in the previous chapter 3, and its 112 tons of liquid argon will work as the near detector for the Short Baseline Neutrino program. The LArTPC is still finishing the installation, and it is expected to start taking data in 2021. The detector will hold three wire planes (again, two induction and one collection) with 3 mm wire spacing. The ionization electrons will have a maximum of 2 m of drift and will experience 500 V/cm of an electric field.

DUNE, the Deep Underground Neutrino Experiment, will consist of two neutrino detectors placed in the most intense neutrino beam in the world, and it is planning to start taking data around 2026. In the meantime, to test the technology and possible geometries, two prototypes will be tested at CERN. ProtoDUNE-SP is a half-height with full-width dimen-
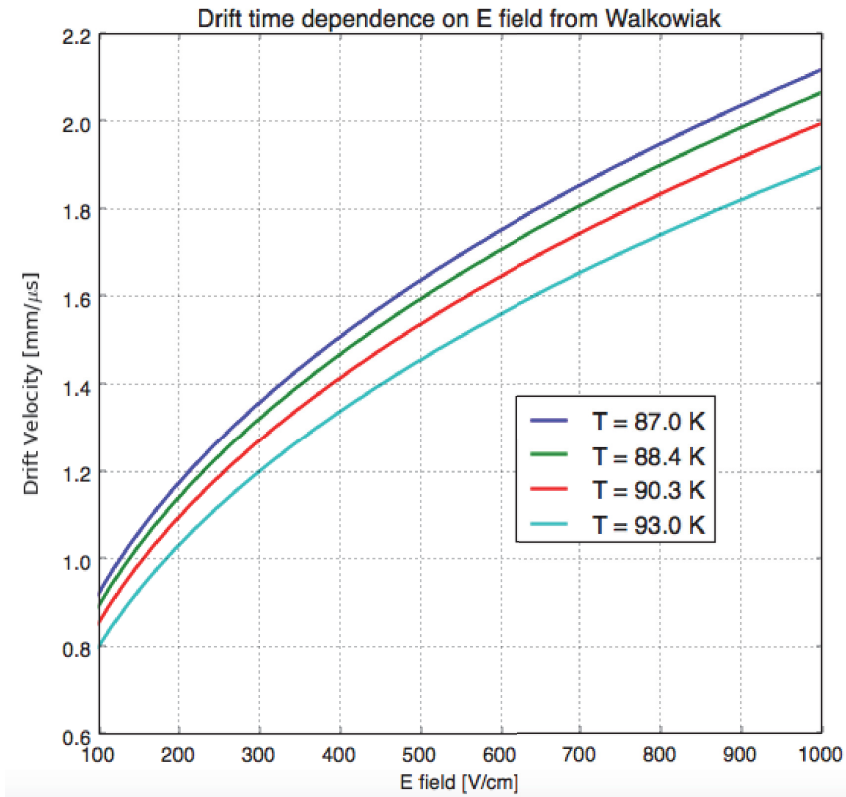
Figure 7.10: Electric Field vs Drift Velocity for several temperatures. (9)

sions of one module of DUNE far detector. With a 0.77 kton of liquid argon, a drift distance of 3.6 m, and an electric field of 500 V/cm, this LArTPC is sitting in a charged particle beam collecting data since 2018 (**?**).

Table **??** summarizes all the relevant information about these experiments to compare with results obtained for LArIAT. Figure 7.10 shows the electron's drift velocity for different liquid argon's temperature and for various electric fields applied to the TPC. Combining all this information is possible to make some predictions for the neutrino experiments.

As shown on table 7.2, for a great shower separation in LArIAT, the detector required a minimum electron lifetime of $\approx 400~\mu$s for Run2 (4 mm), $\approx 250~\mu$s for Run IIIA (5 mm), and $\approx 300~\mu$s for Run IIIB (3 mm). With its electric field of 500 V/cm, these lifetime values allowed the free electrons to have a mean free path of 128% of the drift distance of LArIAT's TPC for Run II configuration. For Run IIIA configuration, the minimum electron lifetime allows a mean free path of 79% of LArIAT's TPC. And for the third configuration with 5 mm wire pitch, the minimum τ allows a mean free path of 100% of the drift distance. Extrapolating this for the three experiments above and taking into account the difference in electron mobility due to different electric fields with the graphic from figure 7.10, the results shown for the

Table 7.3: Results for other LArTPCs using the extrapolated results found for LAr-IAT.

Experiment	Electric Field (V/cm)	Drift Distance (m)	Wire Pitch (mm)	Minimum Electron Lifetime (μs)
MicroBooNE	273	2.5	3	2083
SBND	500	2	3	1333
ProtoDUNE-SP	500	3.6	$\approx$4.7	1896

minimum electron lifetime needed for a good electromagnetic shower separation are found in 7.3.

With these results from table 7.3, it is possible to estimate what should be the minimum electron lifetime to allow good separation of electron-photon showers with at least 80% of electron purity at the one ionizing particle peak. MicroBooNE is already taking data, and the electron lifetime measured is being kept around 10000 μs, way higher than the minimum limit. ProtoDUNE-SP had, during most of its run, much more than the value from the table above, and reached a 6000 μs (**?**). SBND is not running yet, but it is aiming for an electron lifetime greater than 2000 μs.

CHAPTER 8

CONCLUSION

Understand completely how a LArTPC will respond to particles expected to come out of neutrino interactions is essential for the particle physics' future. For this reason, the LArIAT experiment was created.

LArIAT's goals are, among others, to characterize the response of charged particles expected to appear in neutrino interactions, and to distinguish electron from photon initiated showers.

Previous neutrino experiments, LSND and MiniBooNE, found an excess of electron neutrinos with low energy that could indicate the existence of a fourth type of neutrino. Since these two experiments were Cherenkov detectors, they could not distinguish photons from electrons. The next generation of neutrino experiments is being planed on the LArTPC technology, which has excellent spatial resolution and calorimetric capacity. However, to be able to extract good results from the detector is necessary to characterize it and understand what it is expected to be seeing in fully-fledged experiments.

LArIAT is a small detector sitting in a charged particle beam. It is exposed to a high number of electrons, making this experiment the perfect place to understand the response of LAr to signals from electrons and photons. All the information learned with LArIAT will be used for the next generation of neutrino experiments, helping them to understand the reason behind the low energy excess.

To have a good signal from the detector, it is also essential to have argon clean and free from impurities. With the electron's lifetime calculation, it is possible to know how much contaminants are in the detector, and it is also possible to correct the charge read by the readout planes to minimize the negative effect of the impurities.

Table 8.1: Values of minimum electron lifetime for a good electron-photon shower separation on LArIAT's detector.

4 mm wire pitch	5 mm wire pitch	3 mm wire pitch
$\approx 400~\mu$s	$\approx 250~\mu$s	$\approx 300~\mu$s

Table 8.2: Results for other LArTPCs using the extrapolated results found for LAr-IAT.

Experiment	Electric Field (V/cm)	Drift Distance (m)	Wire Pitch (mm)	Minimum Electron Lifetime (μs)
MicroBooNE	273	2.5	3	2083
SBND	500	2	3	1333
ProtoDUNE-SP	500	3.6	≈ 4.7	1896

Preliminary analysis in LArIAT showed in this thesis shows that LArTPCs can separate well signals from electrons and photons, and it also shows how the detector behaves with different electron lifetimes. Chapter 7 gives the relation between τ and a Figure of Merit used to distinguish between electron and photon showers. The main result for LArIAT is shown in table 8.1

Extrapolating this result to some neutrino experiments, it is possible to infer about a minimum electron lifetime for them to be able to separate electromagnetic showers satisfactorily. These results are summarized in table 8.2

The study performed for this thesis shows that these new experiments will be able to distinguish electron and photon initiated showers with more than 80% of electron purity, an important step to understand the low energy excess found in neutrino experiments.

The next step is to apply these results to LArIAT's data using a CNN (Convolution Neural Network) to separate shower from track information on LArIAT's data. The CNN is already being trained, hence shortly, new and exciting results about this are being expected.

BIBLIOGRAPHY

[1] J. A. Formaggio and G. P. Zeller, "From ev to eev: Neutrino cross sections across energy scales," *Rev. Mod. Phys.*, vol. 84, pp. 1307–1341, Sep 2012. [Online]. Available: https://link.aps.org/doi/10.1103/RevModPhys.84.1307 ix, 25, 26

[2] A. A. Aguilar-Arevalo and et al, "Improved search for $\bar{\nu}_\mu \to \bar{\nu}_e$ oscillations in the miniboone experiment," *Phys. Rev. Lett.*, vol. 110, p. 161801, Apr 2013. [Online]. Available: https://link.aps.org/doi/10.1103/PhysRevLett.110.161801 ix, 29, 32

[3] E. Morikawa, R. Reininger, P. Gürtler, V. Saile, and P. Laporte, "Argon, krypton, and xenon excimer luminescence: From the dilute gas to the condensed phase," *The Journal of Chemical Physics*, vol. 91, no. 3, pp. 1469–1477, 1989. [Online]. Available: https://doi.org/10.1063/1.457108 ix, 39, 41

[4] E. Gramellini, "Measurement of the Negative Pion and Positive Kaon Total Hadronic Cross Sections on Argon at the LArIAT Experiment," Ph.D. dissertation, Yale U., 2018. [Online]. Available: http://lss.fnal.gov/archive/thesis/2000/fermilab-thesis-2018-24.pdf x, 46

[5] R. Acciarri and et al, "Effects of nitrogen contamination in liquid argon," *Journal of Instrumentation*, vol. 5, no. 06, p. P06003–P06003, Jun 2010. [Online]. Available: http://dx.doi.org/10.1088/1748-0221/5/06/P06003 x, 68

[6] M. Berger, J. Coursey, M. Zucker, and J. Chang, "Estar, pstar and astar: computer programs for calculating stopping-power and range tables for electrons, protons and helium ions (version 1.2.3)." [Online]. Available: http://physics.nist.gov/Star xi, 79

[7] M. Berger and et al, "Xcom: Photon cross section database (version 1.5)," 2010. [Online]. Available: http://physics.nist.gov/xcom xi, 82

[8] Particle Data Group (PDG), "Passage of particles through matter." [Online]. Available: http://pdg.lbl.gov/2013/reviews/rpp2012-rev-passage-particles-matter.pdf xi, 36, 71, 80, 83, 84

[9] W. Walkowiak, "Drift velocity of free electrons in liquid argon," *Nuclear Instruments and Methods in Physics Research Section A: Accelerators, Spectrometers, Detectors and Associated Equipment*, vol. 449, no. 1, pp. 288 – 294, 2000. [Online]. Available: http://www.sciencedirect.com/science/article/pii/S0168900299013017 xi, 93

[10] Royal Swedish Acad. Sci., "Scientific Background on the Nobel Prize in Physics 2015: Neutrino oscillations," *The Universe*, vol. 3, no. 4, pp. 38–50, 2015. 16

[11] P. W. Higgs, "Broken symmetries and the masses of gauge bosons," *Phys. Rev. Lett.*, vol. 13, pp. 508–509, Oct 1964. [Online]. Available: https://link.aps.org/doi/10.1103/PhysRevLett.13.508 18

[12] F. Englert and R. Brout, "Broken symmetry and the mass of gauge vector mesons," *Phys. Rev. Lett.*, vol. 13, pp. 321–323, Aug 1964. [Online]. Available: https://link.aps.org/doi/10.1103/PhysRevLett.13.321 18

[13] F. Reines and C. Cowan, "The Reines-Cowan experiments: Detecting the Poltergeist," *Los Alamos Sci.*, vol. 25, pp. 4–27, 1997. 20

[14] S. Bilenky, "Neutrino. history of a unique particle," *The European Physical Journal H*, vol. 38, no. 3, p. 345–404, Dec 2012. [Online]. Available: http://dx.doi.org/10.1140/epjh/e2012-20068-9 20

[15] M. L. Perl, "The Discovery of the tau lepton," in *The Rise of the standard model: Particle physics in the 1960s and 1970s. Proceedings, Conference, Stanford, USA, June 24-27, 1992*, 1992, pp. 79–100. [Online]. Available: http://www-public.slac.stanford.edu/sciDoc/docMeta.aspx?slacPubNumber=SLAC-PUB-5937 20

[16] K. Kodama, N. Ushida, C. Andreopoulos, N. Saoulidou, G. Tzanakos, P. Yager, B. Baller, D. Boehnlein, W. Freeman, B. Lundberg, and et al., "Observation of tau neutrino interactions," *Physics Letters B*, vol. 504, no. 3, p. 218–224, Apr 2001. [Online]. Available: http://dx.doi.org/10.1016/S0370-2693(01)00307-0 20

[17] J. N. Bahcall, "Solving the mystery of the missing neutrinos." [Online]. Available: https://www.nobelprize.org/prizes/themes/solving-the-mystery-of-the-missing-neutrinos 21

[18] T. Kajita, "Nobel lecture: Discovery of atmospheric neutrino oscillations," *Rev. Mod. Phys.*, vol. 88, p. 030501, Jul 2016. [Online]. Available: https://link.aps.org/doi/10.1103/RevModPhys.88.030501 21

[19] S. L. Glashow, J. Iliopoulos, and L. Maiani, "Weak interactions with lepton-hadron symmetry," *Phys. Rev. D*, vol. 2, pp. 1285–1292, Oct 1970. [Online]. Available: https://link.aps.org/doi/10.1103/PhysRevD.2.1285 23

[20] N. Cabibbo, "Unitary symmetry and leptonic decays," *Phys. Rev. Lett.*, vol. 10, pp. 531–533, Jun 1963. [Online]. Available: https://link.aps.org/doi/10.1103/PhysRevLett.10.531 23

[21] M. Kobayashi and T. Maskawa, "CP Violation in the Renormalizable Theory of Weak Interaction," *Prog. Theor. Phys.*, vol. 49, pp. 652–657, 1973. 23

[22] B. Pontecorvo, "Inverse beta processes and nonconservation of lepton charge," *Sov. Phys. JETP*, vol. 7, pp. 172–173, 1958, [Zh. Eksp. Teor. Fiz.34,247(1957)]. 23

[23] Z. Maki, M. Nakagawa, and S. Sakata, "Remarks on the Unified Model of Elementary Particles," *Progress of Theoretical Physics*, vol. 28, no. 5, pp. 870–880, 11 1962. [Online]. Available: https://doi.org/10.1143/PTP.28.870 23

[24] R. Acciarri and et al, "Long-Baseline Neutrino Facility (LBNF) and Deep Underground Neutrino Experiment (DUNE)," 2015. 23

[25] M. Gonzalez-Garcia, M. Maltoni, and T. Schwetz, "Global analyses of neutrino oscillation experiments," *Nuclear Physics B*, vol. 908, p. 199–217, Jul 2016. [Online]. Available: http://dx.doi.org/10.1016/j.nuclphysb.2016.02.033 24

[26] The Double Chooz collaboration, "Improved measurements of the neutrino mixing angle $\theta 13$ with the double chooz detector," *Journal of High Energy Physics*, vol. 2014, no. 10, p. 86, Oct 2014. [Online]. Available: https://doi.org/10.1007/JHEP10(2014)086 24

[27] J. K. Ahn, S. Chebotaryov, J. H. Choi, S. Choi, W. Choi, Y. Choi, H. I. Jang, J. S. Jang, E. J. Jeon, I. S. Jeong, K. K. Joo, B. R. Kim, B. C. Kim, H. S. Kim, J. Y. Kim,

S. B. Kim, S. H. Kim, S. Y. Kim, W. Kim, Y. D. Kim, J. Lee, J. K. Lee, I. T. Lim, K. J. Ma, M. Y. Pac, I. G. Park, J. S. Park, K. S. Park, J. W. Shin, K. Siyeon, B. S. Yang, I. S. Yeo, S. H. Yi, and I. Yu, "Observation of reactor electron antineutrinos disappearance in the reno experiment," *Phys. Rev. Lett.*, vol. 108, p. 191802, May 2012. [Online]. Available: https://link.aps.org/doi/10.1103/PhysRevLett.108.191802 24

[28] F. P. An and et al, "New measurement of antineutrino oscillation with the full detector configuration at daya bay," *Phys. Rev. Lett.*, vol. 115, p. 111802, Sep 2015. [Online]. Available: https://link.aps.org/doi/10.1103/PhysRevLett.115.111802 24

[29] K. Abe and et al, "Precise measurement of the neutrino mixing parameter θ_{23} from muon neutrino disappearance in an off-axis beam," *Phys. Rev. Lett.*, vol. 112, p. 181801, May 2014. [Online]. Available: https://link.aps.org/doi/10.1103/PhysRevLett.112.181801 24

[30] A. Gando and et al, "Reactor on-off antineutrino measurement with kamland," *Phys. Rev. D*, vol. 88, p. 033001, Aug 2013. [Online]. Available: https://link.aps.org/doi/10.1103/PhysRevD.88.033001 24

[31] D. Casper, "The nuance neutrino physics simulation, and the future," *Nuclear Physics B - Proceedings Supplements*, vol. 112, no. 1, pp. 161 – 170, 2002. [Online]. Available: http://www.sciencedirect.com/science/article/pii/S0920563202017565 25

[32] A. Aguilar-Arevalo and et al, "Evidence for neutrino oscillations from the observation of $\overline{\nu}_e$ appearance in a $\overline{\nu}_\mu$ beam," *Phys. Rev. D*, vol. 64, p. 112007, Nov 2001. [Online]. Available: https://link.aps.org/doi/10.1103/PhysRevD.64.112007 28

[33] A. A. Aguilar-Arevalo and et al, "The miniboone detector," *Nuclear Instruments and Methods in Physics Research Section A: Accelerators, Spectrometers, Detectors and Associated Equipment*, vol. 599, no. 1, p. 28–46, Feb 2009. [Online]. Available: http://dx.doi.org/10.1016/j.nima.2008.10.028 29

[34] ——, "Measurement of muon neutrino quasielastic scattering on carbon," *Phys. Rev. Lett.*, vol. 100, p. 032301, Jan 2008. [Online]. Available: https://link.aps.org/doi/10.1103/PhysRevLett.100.032301 29

[35] ——, "First measurement of the muon neutrino charged current quasielastic double differential cross section," *Phys. Rev. D*, vol. 81, p. 092005, May 2010. [Online]. Available: https://link.aps.org/doi/10.1103/PhysRevD.81.092005 29

[36] ——, "First observation of coherent π_0 production in neutrino nucleus interactions with $e_\nu < 2gev$," *Physics Letters B*, vol. 664, no. 1-2, p. 41–46, Jun 2008. [Online]. Available: http://dx.doi.org/10.1016/j.physletb.2008.05.006 29

[37] Short-Baseline Neutrino Program. [Online]. Available: https://sbn.fnal.gov/ 30

[38] D. R. Nygren, "The time projection chamber: A new 4 π detector for charged particles." *Technical report*, 1974. [Online]. Available: http://lss.fnal.gov/conf/C740805/p58.pdf. 33

[39] C. Rubbia, "The Liquid Argon Time Projection Chamber: A New Concept for Neutrino Detectors," 1977. 34

[40] J. Nikkel, T. Gozani, C. Brown, J. Kwong, D. Mckinsey, Y. Shin, S. Kane, C. Gary, and M. Firestone, "Liquefied noble gas detectors for detection of nuclear materials," *Journal of Instrumentation - J INSTRUM*, vol. 7, 03 2012. 35

[41] J. Thomas and D. A. Imel, "Recombination of electron-ion pairs in liquid argon and liquid xenon," *Phys. Rev. A*, vol. 36, pp. 614–616, Jul 1987. [Online]. Available: https://link.aps.org/doi/10.1103/PhysRevA.36.614 38

[42] R. Acciarri and et al., "A study of electron recombination using highly ionizing particles in the argoneut liquid argon tpc," *Journal of Instrumentation*, vol. 8, no. 08, p. P08005–P08005, Aug 2013. [Online]. Available: http://dx.doi.org/10.1088/1748-0221/8/08/P08005 39

[43] M. Mooney, "The MicroBooNE Experiment and the Impact of Space Charge Effects," in *Proceedings, Meeting of the APS Division of Particles and Fields (DPF 2015): Ann Arbor, Michigan, USA, 4-8 Aug 2015*, 2015. 39

[44] B. J. P. Jones, "Sterile neutrinos in cold climates," *Ph.D. thesis, MIT*, 2015. [Online]. Available: http://lss.fnal.2363gov/archive/thesis/2000/fermilab-thesis-2015-17.pdf 39

[45] B. J. P. Jones, C. S. Chiu, J. M. Conrad, C. M. Ignarra, T. Katori, and M. Toups, "A measurement of the absorption of liquid argon scintillation light by dissolved nitrogen at the part-per-million level," *Journal of Instrumentation*, vol. 8, no. 07, p. P07011–P07011, Jul 2013. [Online]. Available: http://dx.doi.org/10.1088/1748-0221/8/07/P07011 42

[46] V. Gehman, S. Seibert, K. Rielage, A. Hime, Y. Sun, D.-M. Mei, J. Maassen, and D. Moore, "Fluorescence efficiency and visible re-emission spectrum of tetraphenyl butadiene films at extreme ultraviolet wavelengths," *Nuclear Instruments and Methods in Physics Research Section A: Accelerators, Spectrometers, Detectors and Associated Equipment*, vol. 654, no. 1, p. 116–121, Oct 2011. [Online]. Available: http://dx.doi.org/10.1016/j.nima.2011.06.088 42

[47] "The fermilab hierarchical configuration language." [Online]. Available: https://cdcvs.fnal.gov/redmine/projects/fhicl/wiki. 44

[48] M. Antonello and et al, "Precise 3D track reconstruction algorithm for the ICARUS T600 liquid argon time projection chamber detector," *Adv. High Energy Phys.*, vol. 2013, p. 260820, 2013. 47

[49] C. Anderson and et al, "The ArgoNeuT Detector in the NuMI Low-Energy beam line at Fermilab," *JINST*, vol. 7, p. P10019, 2012. 55

[50] M. Adamowski and et al., "The liquid argon purity demonstrator," *Journal of Instrumentation*, vol. 9, no. 07, p. P07005–P07005, Jul 2014. [Online]. Available: http://dx.doi.org/10.1088/1748-0221/9/07/P07005 57

[51] Technical report, "Glassman high voltage, inc." Precision Regulated High Voltage DC Power Supply. 57

[52] CAEN, "Caen v1495 data sheet," Technical report, 2018. [Online]. Available: http://www.caen.it/csite/CaenProd.jsp?idmod=484&parent=11. 66

[53] B. Baibussinov and et al, "Free electron lifetime achievements in liquid argon imaging tpc," *Journal of Instrumentation*, vol. 5, no. 03, p. P03005–P03005, Mar 2010. [Online]. Available: http://dx.doi.org/10.1088/1748-0221/5/03/P03005 67

[54] R. Acciarri and et al, "Demonstration of mev-scale physics in liquid argon time projection chambers using argoneut," *Physical Review D*, vol. 99, no. 1, Jan 2019. [Online]. Available: http://dx.doi.org/10.1103/PhysRevD.99.012002 68

[55] E. Buckley and et al, "A study of ionization electrons drifting over large distances in liquid argon," *Nuclear Instruments and Methods in Physics Research Section A: Accelerators, Spectrometers, Detectors and Associated Equipment*, vol. 275, no. 2, pp. 364 – 372, 1989. [Online]. Available: http://www.sciencedirect.com/science/article/pii/0168900289907109 69, 70

[56] H. Bichsel, "Straggling in thin silicon detectors," *Rev. Mod. Phys.*, vol. 60, pp. 663–699, Jul 1988. [Online]. Available: https://link.aps.org/doi/10.1103/RevModPhys.60.663 71

[57] E. Segr´e. New York, Benjamin, 1964. 79

[58] B. Rossi. Prentice-Hall, Inc., Englewood Cliffs, NJ, 1952. 80

[59] R. M. Barnett and et al., "Review of particle physics," *Phys. Rev. D*, vol. 54, pp. 1–708, Jul 1996. [Online]. Available: https://link.aps.org/doi/10.1103/PhysRevD.54.1 80

[60] Y.-S. Tsai, "Pair production and bremsstrahlung of charged leptons," *Rev. Mod. Phys.*, vol. 46, pp. 815–851, Oct 1974. [Online]. Available: https://link.aps.org/doi/10.1103/RevModPhys.46.815 80

[61] W. R. Nelson, T. M. Jenkins, R. C. McCall, and J. K. Cobb, "Electron-induced cascade showers in copper and lead at 1 gev," *Phys. Rev.*, vol. 149, pp. 201–208, Sep 1966. [Online]. Available: https://link.aps.org/doi/10.1103/PhysRev.149.201 84

[62] G. Bathow, E. Freytag, M. Koebberling, K. Tesch, and R. Kajikawa, "Measurements of the longitudinal and lateral development of electromagnetic cascades in lead, copper and aluminum at 6 gev," *Nucl. Phys.*, vol. B20, pp. 592–602, 1970. 84

[63] A. B. Christophe, "Valley to peak ratio as a measure for the separation of two chromatographic peaks," *Chromatographia*, vol. 4, no. 10, pp. 455–458, Oct 1971. [Online]. Available: https://doi.org/10.1007/BF02268814 87

[64] MicroBooNE Collaboration. [Online]. Available: https://microboone.fnal.gov/ 92